Alma Mater Studiorum - Università di Bologna

DOTTORATO DI RICERCA IN FISICA
Ciclo XXII

Settore scientifico-disciplinare di afferenza: FIS/04

Measurement of low p_T D^0 meson production cross section at CDF II

Dott. Manuel Mussini

Coordinatore Dottorato:
Prof. Fabio Ortolani

Relatore:
Prof. Franco Rimondi

Correlatore:
Prof. Jeffrey A. Appel

Esame finale anno 2011

Contents

List of Figures

List of Tables

Introduction

In this thesis we present a study of the production of D^0 meson in the low transverse momentum region. In particular the inclusive differential production cross section of the D^0 meson (in the two-body decay channel $D^0 \to K^-\pi^+$) is obtained extending the published CDF II measurement to p_T as low as 1.5 GeV/c. This study is performed at the Tevatron Collider at Fermilab with the CDF II detector.

The behavior of the strong interaction in the low Q^2 (four-momentum transferred in an interaction) region is neither describable nor predictable by theory because in these kinematic conditions the strong coupling constant α_s is of the order of the unity. It's not, therefore, possible for low momentum transferred interactions to obtain QCD features through theories based on perturbative expansions. In that situation a global investigation of the physical quantities involved in the interactions becomes necessary in order to develop new models that bypass this mathematical limitation. At present, current phenomenological models are usually able to describe only few aspects of the observed physical quantities and not their whole interplay. New measurements on real data are then crucial to understand and theoretically model QCD where α_s becomes too big for perturbative expansions and the colour confinement behaviour is not yet understood.

To perform this kind of study we have to select samples which best represent the natural distribution of data, removing any possible bias due to the data taking selection because they could modify the natural shapes of the physical quantities we are interested in. The upgraded Collider Detector at the Fermilab Tevatron (CDF II) is a good environment for studing this region. Dedicated works were published by CDF both in Run I and Run II to explore this "soft" region but only the s-quark contribution was studied in Run I via the production cross section measurement of mesons and barions contanining one quark s like K^0_s and Λ^0. The huge amount of data that CDF II is now collecting in Run II gives us the great opportunity to extend our knowledge to a new flavor contribution: the quark c. Because of its relatively big mass, the quark c production cross section is several order of magnitude smaller than lighter quarks ones (u, d and s) and low p_T can be probed only collecting hundreds of millions of collisions between protons and antiprotons. The measurement of the differential cross section plays an important role in this context; evaluating it to low p_T can give important informations to refine the actual knowledge.

This thesis is organized as follows.

Chapter 1 describes the theoretical framework of the D^0 meson and its place within the Standard Model (SM); the importance of the study presented here is also explained.

Chapter 2 contains a general description of the Tevatron collider and of the CDF II experiment.

Chapter 3 describes the online and offline data selections with a description of the optimization tecnique used to extract the D^0 signal.

Chapter 4 lists the Monte Carlo samples used for this work, their features and their use through the analysis.

Chapter 5 is devoted to the fitting procedure used to estimate the yields of the signal as a function of the D^0 transverse momentum.

Chapter 6 describes the evaluation of the trigger and the reconstruction efficiencies.

Chapter 7 describes the main sources of systematic uncertainties.

Chapter 8 presents the final result of the measurement and its interpretation.

Results will be under internal CDF review for pubblication by the end of next summer.

Chapter 1

Theory and motivation

This chapter is devoted to the description of the importance and uniqueness of the measurement obtained with this analysis. A general description of the Standard Model and the Strong Interaction are followed by a brief history of the measurements related to the D^0 mesons. The motivations of this analysis are then discussed.

1.1 The Standard Model

The Standard Model (SM) is a quantum field theory that describes all elementary particles and three of the four fundamental forces known today (gravitation is not included): the strong, the electromagnetic and the weak interactions (the latter two unified into the electroweak interaction). Behind the formulation of the SM there's a principle of symmetry for the Lagrangian which is invariant under appropriate transformations, called local gauge transformations. The gauge transformations that describe the forces observed in nature are those of the unitary group:

$$G_{SM} = SU(3)_C \otimes SU(2)_T \otimes U(1)_Y \tag{1.1}$$

where the subscripts indicate the conserved charges: the strong charge or color C, the weak isospin T (or rather its third component T_3) and the hypercharge Y. These quantities are linked to the electric charge Q (which is also conserved) through the Gell-Mann–Nishijima relation:

$$Q = \frac{Y}{2} + T_3 \tag{1.2}$$

In this model, the elementary particles appear as representations of the G_{SM} symmetry group. They are divided into two groups: fermions (with spin 1/2 and described by the Fermi-Dirac statistics) and bosons (with integer spin and described by the Bose-Einstein statistics). There are 12 fundamental fermions and the corresponding anti-particles; 6 of them, called *leptons*, interact only through the electroweak force while the other 6, called *quarks* are also coupled to the strong force.

Generation:	**I**	**II**	**III**	$\mathbf{T_3}$	**Y**	**Q**
Leptons	$\begin{pmatrix}\nu_e\\ e\end{pmatrix}_L$	$\begin{pmatrix}\nu_\mu\\ \mu\end{pmatrix}_L$	$\begin{pmatrix}\nu_\tau\\ \tau\end{pmatrix}_L$	+1/2 −1/2	−1 −1	0 −1
	e_R	μ_R	τ_R	0	−2	−1
Quarks	$\begin{pmatrix}u\\ d'\end{pmatrix}_L$	$\begin{pmatrix}c\\ s'\end{pmatrix}_L$	$\begin{pmatrix}t\\ b'\end{pmatrix}_L$	+1/2 −1/2	1/3 1/3	+2/3 −1/3
	u_R d'_R	c_R s'_R	t_R b'_R	0 0	4/3 −2/3	+2/3 −1/3

Table 1.1: *SM elementary particles.*

Leptons (see Table 1.1), which in the SM are massless particles, are divided into three iso-doublets with negative helicity (left-handed) and 3 iso-singlets with positive helicity (right-handed); in the doublets the particle with T_3 = -1/2 has a negative unitary charge, while the particle with $T_3 = +1/2$ has neutral charge and it's called the neutrino. The charged leptons are called electron (e), muon (μ) and tau (τ); neutrinos interact only via the weak force and are only left-handed [1].

The quarks (see Table 1.1) are also divided into iso-doublets and iso-singlets and they are all electrically charged. Particles with $T_3 = +1/2$ in the doublets have a fractional charge of +2/3 while the other particles have charge -1/3. The six types of quarks are called "flavors" and are: up (u), down (d), charm (c), strange (s), top (t) and bottom (b). The strong charge is called "color" and the quarks are triplets of $SU_C(3)$ (i.e. they can exist in three different colors: C = R, G, B). If one chooses a base where u, c and t quarks are simultaneously eigenstates both of the strong and the weak interaction, the remaining eigenstates are usually written as d, s and b for the strong and d', s' and b' (they result rotated w.r.t. the previous) for the weak interaction.

The elementary particles with spin 1 are the gauge bosons (see Table 1.2); they are the mediators of the fundamental interactions, namely the generators of the G_{SM} symmetry group: the photon (γ) and the three vector bosons ($W^\pm$ and Z) are generators of the $SU_T(2) \otimes U_Y(1)$, while the gluons (g) are the generators of the group $SU_C(3)$.

Gauge theories are not able to describe massive particles but this contradicts what is observed experimentally (e.g. the vector bosons, see [2, 3]). On the other hand, massive fields would make the theory non-renormalizable, which is incoherent from the mathematical point of view. To correctly describe the massive particles in the SM, a scalar iso-doublet H is introduced (see Table 1.3). The *Higgs field* spontaneously breaks the electroweak symmetry through the Higgs mechanism and

Interaction	**Gauge boson**	**Q**
Electroweak	γ	0
	Z^0	0
	$W^{\pm}$	± 1
Strong	$g_\alpha(\alpha = 0, \ldots, 8)$	0

Table 1.2: *SM four fundamental interactions and gauge bosons.*

Higgs boson:	$\mathbf{T_3}$	**Y**	**Q**
$H = \begin{pmatrix} H^+ \\ H^0 \end{pmatrix}$	$+1/2$	1	1
	$-1/2$	1	0

Table 1.3: *The Higgs boson.*

gives the mass to the gauge bosons and the fermions [4, 5]:

$$SU_T(2) \xrightarrow{<H>} U_{em}(1) \tag{1.3}$$

The Higgs boson H has not been observed experimentally yet and its mass is one of the free parameters in the SM.

1.2 Quantum Chromodynamics

The modern theory of the strong interaction is Quantum Chromodynamics (QCD), the quantum field theory of quarks and gluons based on the non-abelian SU(3) gauge group. QCD is well tested at high energies, where the strong coupling constant becomes small and perturbation theory applies. In the low-energy regime, however, QCD becomes a strongly-coupled theory, many aspects of which are not understood. Conceptually, QCD is simple: it is a relativistic quantum field theory of quarks and gluons interacting according to the laws of non-abelian forces between colour charges. The starting point of all considerations is the QCD Lagrangian density:

$$\mathcal{L}_{QCD} = -\frac{1}{4} G_a^{\mu\nu} G^a_{\mu\nu} + \sum_f \bar{q}_f [i\gamma^\mu D_\mu - m_f] q_f \tag{1.4}$$

where

$$G_a^{\mu\nu} = \partial^\mu A_a^\nu - \partial^\nu A_a^\mu + g f_a^{bc} A_b^\mu A_c^\nu \tag{1.5}$$

is the gluon field strength tensor and

$$D^\mu = \partial^\mu - i\frac{g}{2} A_a^\mu \lambda^a \tag{1.6}$$

the gauge covariant derivative involving: the gluon field A_a^μ, the strong coupling constant g ($\alpha_s = g^2/4\pi$) and the quark flavours f relevant in the interaction[1].

[1] We consider $\hbar = 1 = c$.

This deceptively simple looking QCD Lagrangian is at the basis of the rich and complex phenomena of nuclear and hadronic physics. How this complexity arises in a theory with quarks and gluons as fundamental degrees of freedom is only qualitatively understood. The QCD field equations are non-linear since the gluons that mediate the interaction carry colour charge and hence interact among themselves. This makes every strongly-interacting system intrinsically a many-body problem wherein, apart from the valence quarks, many quark-antiquark pairs and many gluons are always involved. This non-abelian feature of QCD is believed to lead to the phenomenon that the basic degrees of freedom, quarks and gluons, cannot be observed in the QCD spectrum. The confinement of colour charge is the reason behind the complex world of nuclear and hadronic physics.

The process of renormalization in quantum field theory generates an intrinsic QCD scale Λ_{QCD} through the mechanism of dimensional transmutation; loosely speaking, Λ_{QCD} is the scale below which the coupling constant becomes so large that standard perturbation theory no longer applies. All hadron masses are in principle calculable within QCD in terms of Λ_{QCD}. This dynamical generation of the mass scale of the strong interaction is the famous QCD gap phenomenon; the proton mass is non-zero because of the energy of the confined quarks and gluons. Although a mathematical proof of colour confinement is lacking, qualitatively this is thought to be linked to the fact that the quark and gluon bilinears $\bar{q}_a q^a$ and $G^a_{\mu\nu} G^{\mu\nu}_a$ acquire non-zero vacuum expectation values.

Now, some 35 years after the development of QCD, it is fair to say that strong interactions are understood in principle, but a long list of unresolved questions about low-energy QCD remains. Our present understanding of QCD thereby serves as the basis to set priorities for theoretical and experimental research. Experiments that test QCD in the non-perturbative regime to improve our limited understanding of several aspects are crucial.

1.2.1 The QCD Coupling Constant

The qualitative understanding of QCD, as outlined above, is to a large extent based on a classical calculation of the renormalization scale dependence of the QCD coupling constant α_s as given by the β-function at an energy scale μ:

$$\beta(\alpha_s) \equiv \frac{\mu}{2}\frac{\partial \alpha_s}{\partial \mu} = -\frac{\beta_0}{4\pi}\alpha_s^2 - \frac{\beta_1}{8\pi^2}\alpha_s^3 - \dots \tag{1.7}$$

where

$$\beta_0 = 11 - \frac{2}{3}n_f \tag{1.8}$$

$$\beta_1 = 51 - \frac{19}{3}n_f \tag{1.9}$$

and n_f is the number of quarks with mass less than μ. In solving this differential equation for α_s, one introduces the scale Λ to provide the μ dependence of α_s. A first order approximate solution can be written as follows:

$$\alpha_s(\mu^2) = \frac{\alpha_s(\Lambda^2)}{1 + \frac{\alpha_s(\Lambda^2)}{12\pi}\beta_0 ln\frac{\mu^2}{\Lambda^2}} \tag{1.10}$$

The solution demonstrates the famous properties of asymptotic freedom

$$\alpha_s \xrightarrow{\mu \to +\infty} 0 \tag{1.11}$$

and of strong coupling at scales below $\mu \sim \Lambda$ as shown in Figure 1.1. Based on

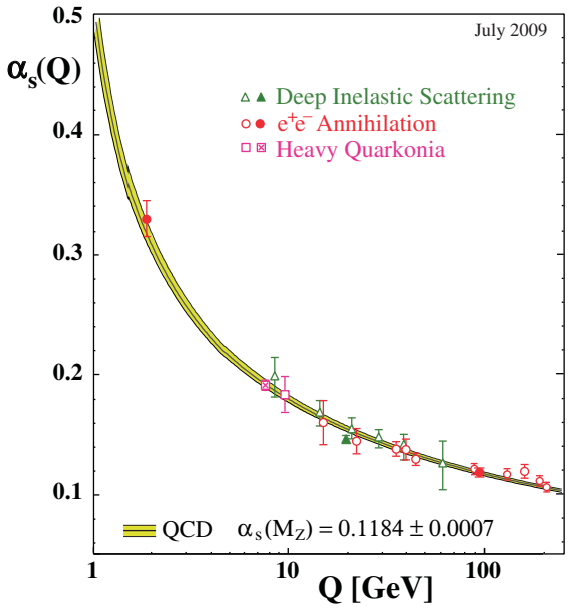

Figure 1.1: *The running of the strong coupling constant as a function of the scale* μ.

this result for the scale dependence of the QCD coupling constant, one may roughly divide the field of strong interaction physics into the areas of perturbative QCD (pQCD) and of non-perturbative QCD. This theory has been very successful in quantitatively describing phenomena where perturbation theory with its standard machinery of Feynman rules applies. An important example is the e^+e^- annihilation in the area of the Z^0 boson, where the multi-particle hadronic final-state system reveals the pQCD physics in the form of the quark and gluon jets. In this perturbative regime, predictions can be made on the basis of the magnitude of the QCD coupling constant. Its value as a function of the energy determines a host of phenomena, such as scaling violations in deep inelastic scattering, the τ lifetime, high-energy hadron collisions, heavy-quarkonium (in particular bottomonium) decay, e^+e^- collisions and

jet rates in ep collisions. The coupling constant derived from these processes are consistent and lead to an average value [6] (see Figure 1.2):

$$\alpha_s(m_Z^2) = 0.1184 \pm 0.0007. \tag{1.12}$$

The non-perturbative regime is the area of strong nuclear forces and hadronic

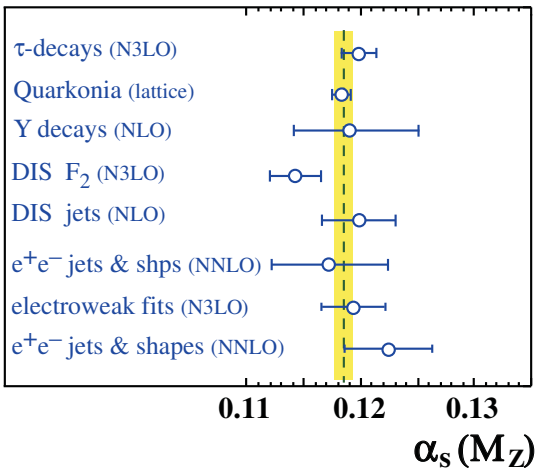

Figure 1.2: *Summary of $\alpha_s(m_Z^2)$ measurements and world average value.*

resonances which are quantitatively much less well understood and where important questions still have to be addressed.

1.2.2 The symmetries of QCD

It has been said that QCD is a most elegant theory in physics since its structure is solely determined by symmetry principles: QCD is the most general renormalisable quantum field theory based on the SU(3) gauge group. In addition to exact Lorentz invariance and SU(3) colour gauge invariance, it has several other important symmetry properties. The QCD Lagrangian, as given above, has a number of "accidental" symmetries (i.e. symmetries that are an automatic consequence of the assumed gauge invariance). The discrete symmetries parity and charge conjugation are such accidental symmetries; flavour conservation is another one: the number of quarks (minus antiquarks) of each flavour is conserved, corresponding to an automatic invariance of the Lagrangian under phase rotations of the quark fields of each flavour separately.

Additional symmetries result from the consideration that the masses of the up, down and strange quarks can be considered small compared to the typical hadronic scale Λ_{QCD}. To the extent that these masses can be ignored, the QCD Lagrangian is invariant under unitary transformations of the quark fields of the form $q_i' = U_{ij}q_j$.

This accounts for the rather accurate SU(2)-isospin and the approximate SU(3)-flavour symmetries of nuclear and hadronic physics. Moreover, when the u, d and s masses can be ignored, QCD is invariant under separate unitary transformations among the left and right-handed quarks ($q_i^{L'} = U_{ij}^L q_j^L$ and $q_i^{R'} = U_{ij}^R q_j^R$) resulting in the chiral symmetry group $\mathrm{U}(3)_L \times \mathrm{U}(3)_R$. The diagonal subgroup ($\mathrm{U}(3)_L = \mathrm{U}(3)_R$) corresponds to the SU(3)-flavour (and barion number) symmetry mentioned. The remaining chiral SU(3) summetry ($\mathrm{U}(3)_L^{-1} = \mathrm{U}(3)_R$) is believed to be spontaneously broken by the vacuum state of QCD, resulting in the existence of an octet of Goldstone bosons identified with the pseudoscalar mesons π, K and η.

These approximate flavour and chiral symmetries due to the smallness of the u, d and s quark masses are important since they can be exploited to formulate effective field theories that are equivalent to QCD in a certain energy range. A classical example is heavy-quark effective theory (HQET) for hadrons contaning a quark c, b or t because their mass is $m_Q \gg \Lambda_{QCD}$. In the limit $m_Q \to +\infty$ the heavy quark becomes on-shell and the dynamics becomes independent of its mass. The hadronic matrix elements can be expanded as a power series in $1/m_Q$ resulting in symmetry relations between various matrix elements [7].

Generalizing QCD to an SU(N_c) gauge theory, the inverse of the number of colours, $1/N_c$, is a hidden expansion parameter [8]; this theory wherein the coupling is decreased, such that $g^2 N_c$ is constant, is called "large-N_c QCD". Diagrammatic considerations suggest that large-N_c QCD is a weakly-coupled theory of mesons and baryons wherein baryons are heavy semiclassical objects.

1.2.3 Theoretical approaches to non-perturbative QCD

Lattice QCD (LQCD) is an *ab initio* approach to deal with QCD in the non-perturbative low-energy regime. The equations of motion of QCD are discretised on a 4-dimensional space-time lattice and solved by large-scale numerical simulations on big computers. For numerical reasons the QCD action is Wick rotated into Euclidean space-time. The lattice spacing, a, acts as the ultraviolet regulator of the theory; by letting $a \to 0$ the regulator is removed and continuum results are obtained. LQCD, originally proposed by Wilson in 1974, has made enormous progress over the last decades. In the past the accuracy of LQCD results were limited by the use of the "quenched approximation" (i.e. the neglect of sea quarks) by unrealistic heavy up and down quarks and by the use of only two (instead of three) light quark flavours. These deviations from "real QCD" were partly mandated by the limited availability of CPU-time; in recent years all these limiting aspects (finite volume effects, lattice artefacts, unrealistic quark masses, exclusion of sea quarks, ...) are being improved upon gradually.

Calculations from QCD, be it pQCD or LQCD, are and will remain very difficult, especially in situations where several dynamical scales are involved. Effective field

theory (EFT) techniques in many such cases can provide a solution. For instance, LQCD is paticularly powerful when it is combined with EFT. A variety of EFTs with quark and gluon degrees of freedom have been developed in recent years. Exploiting a scale separation a simpler theory is obtained that is equivalent to full QCD in the energy region considered. The degrees of freedom above a chosen energy scale are integrated out (in a path-integral sense) and the resulting field theory is organized as a power series of operators containing the low-energy degrees of freedom over the heavy scales. The high-energy physics is encoded in the coupling constants multiplying these operators, which are calculated by "matching" selected observables in the EFT and in full QCD. In the process, the symmetries of QCD need to be obeyed.

1.3 Quark c and the D mesons

Unlike for strangeness, the existence of hadrons with the charm quantum number had been predicted in 1963 for taking into account normalization issues of the weak interactions due to the invocation of non-abelian gauge theories [9, 10]. The salient features of charm quarks (c) needed to keep the theory consistent and manage consequent possible anomalies were the following.

- They possess the same coupling as u quarks;
- yet their mass is much heavier, namely about 2 GeV/c^2.
- They form charged and neutral hadrons, of which (in the C = 1 sector) three mesons and four baryons are stable; i.e., decay only weakly with lifetimes of very roughly $10^{-13}s$.
- Charm decay produces direct leptons and preferentially strange hadrons.

It's amazing to see, ~ 50 years later, how these assumptions were reliable.
c quarks occupy a unique place among *up*-type quarks. t quarks decay before they can hadronize and, on the other end of the mass spectrum, there are only two weakly decaying light flavour hadrons, the neutron and the pion: in the former the d quark decays and in the latter the quarks of the first family annihilate each other. In this picture the c quark is the only *up*-type quark whose hadronization and subsequent weak decay can be studied. Since the charm is an *up-type* quark, loop diagrams do not involve the heavy top quark and the SM prediction for these processes is smaller by many orders of magnitude. Intermediate meson-states are expected to contribute at the 10^{-3} level and thus overshadow the short-distance contributions. While it will be more difficult to observe loop-mediated processes, new physics may enhance them and actually leave more distinct signatures in the charm system than in the bottom system. Experimentally, charm has some distinct advantages compared to the B-system: branching fractions into fully reconstructed modes are up to

the 10 % level, while the product of branching ratios to fully reconstruct a b decay is typically at the 10^{-4} level. About one third of the D^0 comes from a $D^{*+} \to D^0\pi^+$ decay, where the slow pion tags the D^0 flavor at production with an efficiency of almost 100 %.

Just like the kaon and B systems, mixing of neutral mesons can occur in the charm system through box-diagrams. Since the c quark is of the up-type, box-diagrams involve the relatively light d, s and b quarks and lack the large contributions from the heavy t quark. The box-diagram prediction for $x = \Delta M/\Gamma$ and $y = \Delta\Gamma/2\Gamma$ are at the 10^{-5} level [11] (hadronic intermediate states can bring it to the 10^{-5} level). New physics has a little effect on $\Delta\Gamma$, but may have significant contributions to ΔM up to values of x at the 1 % level. Contributions from non-perturbative QCD tend to increase $\Delta\Gamma$ but the effect on ΔM is small. An observation of the x at the percent level together with a strong limit on y at the 10^{-3} level would be a strong indication for new physics. No evidence for D^0 mixing has been found yet; the CDF collaboration is extremely active in this sense and recently published a measurement of the time integrated CP violation in $D^0 \to \pi\pi$ decays evaluating it to be $A_{CP}(\pi^+\pi^-) = (0.22 \pm 0.24(stat.) \pm 0.11(syst.))\%$ (with a sensitivity never reached even at the B factories) where:

$$A_{CP}(\pi^+\pi^-) = \frac{\Gamma(D^0 \to \pi^+\pi^-) - \Gamma(\bar{D}^0 \to \pi^+\pi^-)}{\Gamma(D^0 \to \pi^+\pi^-) + \Gamma(\bar{D}^0 \to \pi^+\pi^-)} \tag{1.13}$$

A similar result for $A_{CP}(K^+K^-)$ is going to be published soon.

1.4 D^0 mesons production cross section measurements

Recently, the inclusive production of charmed hadrons (X_c) at hadron colliders has been the subject of extensive experimental and theoretical studies. In 2003, the CDF Collaboration published the measurements of the differential cross sections for the inclusive production of D^0, D^+, D^{*+} and D_s^+ mesons (and their antiparticles) as a function of the transverse momentum for $p_T \geq 5.5$ GeV/c [12]. The PHENIX Collaboration measured non-photonic electron production through charm and bottom decays in pp, dAu and AuAu collisions at the BNL Relativistic Heavy Ion Collider (RHIC) with $\sqrt{s} = 200$ GeV as a function of p_T [13]. The STAR Collaboration at RHIC presented mid-rapidity open charm spectra from direct reconstruction of $D^0 \to K\pi$ decays in dAu collisions and indirect e^+e^- measurements via charm semileptonic decays in pp and dAu collisions at $\sqrt{s} = 200$ GeV [14]; they also reported results on non-photonic electron production in pp, dAu and AuAu collisions at $\sqrt{s} = 200$ GeV [15]. Unfortunately, these RHIC data only cover a very limited

low-p_T range, where theoretical predictions based on pQCD are difficult.

On the theoretical side, the cross sections for the inclusive production of X_c mesons can be obtained as convolutions of universal parton distribution functions (PDFs) and universal fragmentation functions (FFs) with perturbatively calculable hard-scattering cross sections. The non-perturbative input in the form of PDFs and FFs must be known from fits to other processes. The universality of the PDFs and FFs guarantees unique predictions for the cross section of the inclusive production of heavy-flavored hadrons. The results of such calculations for X_c production at the energy available at the Tevatron have recently been compared to CDF results [16, 17]. For all four meson species, theory is in good agreement with the data in the sense that the experimental and theoretical errors overlap but the central data points tend to overshoot the central theoretical prediction even by a factor of about 1.5 at the lower end of the considered p_T range. The experimental results are gathered on the upper side of the theoretical error band, corresponding to a small value of the renormalization scale (μ_R) and large values of the factorization scales (μ_F and μ'_F, related to the initial and final states respectively).

It is clear how new measurements on real data are crucial to understand and theoretically model QCD where α_s becomes too big for perturbative expansions and the colour confinement behaviour is not yet understood. The measurement of the $D^0 \to K\pi$ differential cross section plays an important role in this context; the extension of the previous CDF published one to low p_T can give important information to refine the current knowledge. The uniqueness of this measurement has to be highlighted because even if new-generation accelerators will be able to probe the same p_T range, their experimental conditions won't reproduce (at least for several decades from now) Tevatron ones both in terms of initial state ($p\bar{p}$) and center of mass energy ($\sqrt{s}$ = 1.96 TeV). Different energies means different conditions and processes interlacing into the unknown region that we have to probe. A comprehension of the energy scale dependence in non-pQCD conditions plays a fundamental role in this picture too.

In this work we measure the D^0 meson inclusive differential production cross section as a function of the transverse momentum defined as follows:

$$\frac{d\sigma_{D^0\to K\pi}}{dp_T}(p_T; |y| \le 1) = \left.\frac{\frac{N_{D^0}+N_{\bar{D}^0}}{2}(p_T)}{L \cdot \varepsilon_{trig} \cdot \varepsilon_{rec}(p_T) \cdot Br(D^0 \to K\pi)}\right|_{|y|\le 1} \tag{1.14}$$

where:

- N_{D^0} and $N_{\bar{D}^0}$ are the yields of the D^0 and $\bar{D}^0$ signals. The factor of 1/2 is included because we count both D^0 and $\bar{D}^0$ mesons while we report the cross section for D^0 mesons only and not for the sum of D^0 and $\bar{D}^0$. Actually what

is measured is the average cross section for D^0 and $\bar{D}^0$ mesons and we assume charge invariance in the production process through strong interaction.

- L is the integrated luminosity of the data sample.
- ε_{trig} is the trigger efficiency.
- ε_{rec} is the global reconstruction's efficiency of our candidates. It takes into account geometrical and kinematical acceptances and also the detector's reconstruction efficiency of the signal.
- $Br(D^0 \to K\pi)$ is the decay branching ratio of the channel used in this analysis.

Chapter 2

The Tevatron Collider and the CDF II experiment

This chapter briefly describes the Tevatron collider accelerator and the CDF II detector, focusing on the subsystems most important for this analysis such as the trigger and the tracking systems. For an exhaustive description of the experimental apparatus, refer to [18].

2.1 The Tevatron collider

The Fermilab Tevatron collider is the last and highest energy accelerating stage located at Fermi National Accelerator Laboratory (a.k.a. FNAL or Fermilab), about 50 km West from Chicago (Illinois) in the US. The Tevatron is a circular superconducting magnets synchrotron, with a 1 km radius, able to produce collisions between bunches of protons (p) and antiprotons ($\bar{p}$) with an energy of 980 GeV; the energy available in the center of mass is thus $\sqrt{s}$ = 1.96 TeV. The Tevatron produced its first $p\bar{p}$ collision in 1985 and since then has undergone extensive upgrades and improvements. In order to reach $p\bar{p}$ interactions at this energy, several preparation and acceleration steps are needed; Figure 2.1 shows the arrangement in the laboratory area of all the machines involved.

2.1.1 Luminosity and $\sqrt{s}$

The performance of a collider is evaluated in terms of two key parameters: the available center of mass energy, $\sqrt{s}$ and the instantaneous luminosity, $\mathcal{L}$.

The latter is the coefficient of proportionality between the rate of a given process and its cross section σ:

$$\text{rate [events s}^{-1}\text{]} = \mathcal{L}\ [\text{cm}^{-2}\text{s}^{-1}] \times \sigma\ [\text{cm}^{2}] \tag{2.1}$$

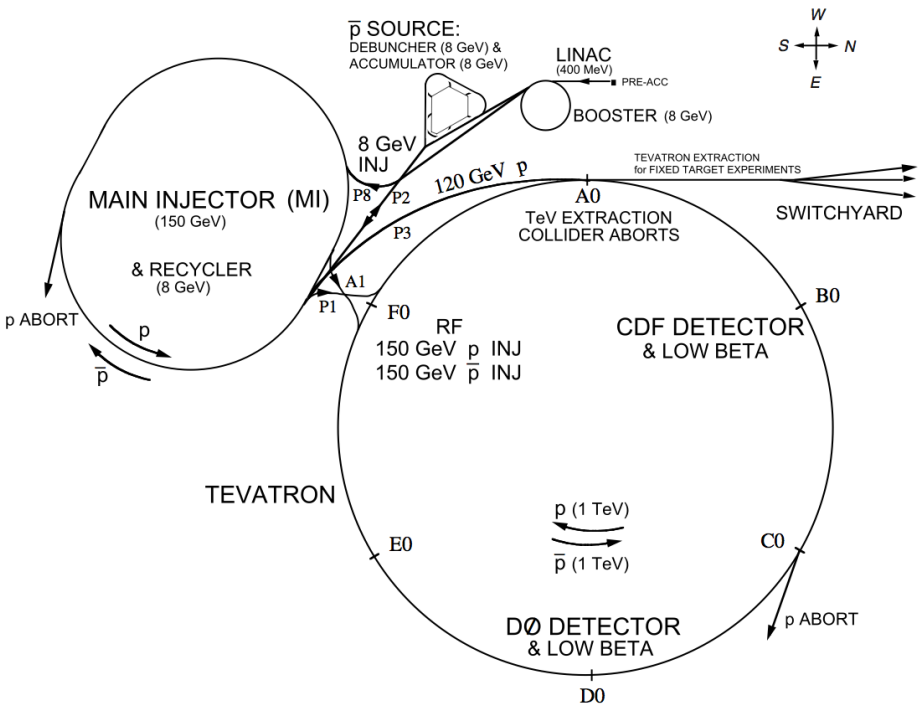

Figure 2.1: *Illustration of the Fermilab Tevatron collider.*

The time integral of the luminosity (integrated luminosity) is therefore a measurement of the expected number of events, n, produced in a finite time ΔT:

$$n(\Delta T) = \sigma \int_{\Delta T} \mathcal{L}(t)\, dt \tag{2.2}$$

Assuming an ideal head-on $p\bar{p}$ collision with no crossing angle between the beams, the instantaneous luminosity is defined as:

$$\mathcal{L} = 10^{-5} \frac{N_p N_{\bar{p}} B f \beta\gamma}{2\pi\beta^* \sqrt{(\epsilon_p + \epsilon_{\bar{p}})_x (\epsilon_p + \epsilon_{\bar{p}})_y}} \mathcal{H}(\sigma_z/\beta^*) \ [10^{30}\mathrm{cm}^{-2}\mathrm{s}^{-1}] \tag{2.3}$$

$\mathcal{L}$ depends on the following Tevatron parameters: the number of circulating bunches in the ring ($B = 36$), the revolution frequency ($f = 47.713$ kHz), the Lorentz relativistic factor (boost, $\beta\gamma = 1045.8$ at 980 GeV), the average numbers of protons ($N_p \approx 2.78 \times 10^{12}$) and antiprotons ($N_{\bar{p}} \approx 8.33 \times 10^{11}$) in a bunch, an empiric "hourglass" factor ($\mathcal{H} = 0.6$-0.7), which is a function of the ratio between the longitudinal r.m.s. width of the bunch ($\sigma_z \approx 60$ cm) and the "beta function" calculated at the interaction point ($\beta^* \approx 31$ cm) and the 95% normalized emittances of the beams ($\epsilon_p \approx 18\ \pi$ mm mrad and $\epsilon_{\bar{p}} \approx 13\ \pi$ mm mrad after injection)[1]. The luminosity limiting factor

[1]The hourglass factor is a parameterization of the longitudinal profile of the beams in the

at the Tevatron is the availability of $\bar{p}$ because its production has a low efficiency, it's difficult to compact them into bunches and it's hard to trasfer them through the subsequent accelerator stages.

$\sqrt{s}$, instead, defines the accessible phase space for the production of resonances in the final states; this Tevatron parameter was increased after the upgrade from Run I to Run II moving from 1.8 to 1.96 TeV thanks to an improvement of the performances of the superconducting-magnet cooling system. The particles lost from the bunches in theirs circular orbits increase the temperature of the magnets; when the minimum value for the superconduction is overtaken, the magnets are no more able to curve the particles trajectories and the beam is lost. The $\sqrt{s}$ value is extremely important because it fixes the upper limit for the masses of the particles produced in the $p\bar{p}$ interaction.

The Tevatron provides beams for experiments in different modes (collider, fixed-target, fixed-target for neutrinos beams, ...); for the purpose of the present analysis, we will focus on the procedure for obtaining a continuous period of collider operation using the same collection of protons and antiprotons, called a *store*. Further details can be found in [19].

2.1.2 Protons beam

H^- ions are produced by ionization of gaseous hydrogen and boosted to 750 keV by a commercial *Cockroft-Walton* accelerator. They are then injected in a 150 m long linear accelerator called *Linac* which increases their energy to 400 MeV. A carbon foil is then used to strip the two electrons from the H^- before the resulting protons are injected to the *Booster*. The Booster (see Figure 2.1) is a rapid cycling synchrotron (with a radius of 75.5 m) that accelerates the protons up to 8 GeV and compacts them into bunches. The protons bunches are then transferred to the following synchrotron, called the *Main Injector*, which brings their energy to 150 GeV: this is the beginning of the process of final injection into the Tevatron called "shot". Inside the Main Injector several bunches are coalesced into one for Tevatron injection. The last stage of the process is the transfer to the Tevatron, a synchrotron which employs superconducting Nb-Ti alloy filaments embedded in copper as magnet

collision region, which assumes the shape of an horizontal hourglass centered in the interaction region. The beta function is a parameter convenient for solving the equation of motion of a particle through an arbitrary beam transport system. The emittance ϵ measures the phase-space occupied by the particles of the beam. Three independent two-dimensional emittances are defined. The quantity $\sqrt{\beta\epsilon}$ is proportional to the r.m.s. width of the beam in the corresponding phase plane. On-line measurements of the transverse emittances are performed at the Tevatron with various methods, including flying through the beam a 7 μm wire and by measuring the cascade of losses, which is proportional to the beam intensity, or detecting the synchrotron light radiated by the particles at the edge of a dipole magnet.

coils. The magnetic field of 5.7 T keeps the protons on an approximately circular orbit while they reach the final energy of 980 GeV.

2.1.3 Antiprotons beam

While the energy of the protons bunches circulating in the Main Injector reaches 120 GeV, they are slammed to a rotating 7 cm thick nickel or copper target. Spatially wide-spread antiprotons are produced and then focused into a beam via a cylindrical lithium lens which separates $\bar{p}$ from other charged interaction products. The emerging antiprotons have a bunch structure similar to that of the incident protons and are stored in a *Debuncher*. It is a storage ring where the momentum spread of the $\bar{p}$ is reduced while maintaining a constant energy of 8 GeV, via stochastic cooling stations. Many cycles of Debuncher cause the destruction of the bunch structure which results in a continuous beam of antiprotons. At the end of the process the monochromatic antiprotons are stored in the *Accumulator* (see Figure 2.1), which is a triangle-shaped storage ring, where they are further cooled and stored until the cycles of the Debuncher are completed. When a current sufficient to create 36 bunches with the required density is available, the $\bar{p}$ are injected into the Main Injector. Here their energy is raised to 150 GeV and they are transferred to the Tevatron where 36 bunches of protons are already circulating in the opposite direction.

2.1.4 The collision

When 36 bunches of both protons and antiprotons are circulating in the Tevatron, the energy of the machine is increased in about 10 seconds from 150 to 980 GeV and the collisions begin at the two interaction points: DØ (where the homonym detector is located) and BØ (home for CDF II). Special quadrupole magnets (*low-β squeezers*) located at both extremities of the detectors along the beam pipe "squeeze" the beam to maximize the luminosity inside the detectors. A roughly Gaussian distribution of the interaction region along the beam axis is achieved ($\sigma_z \approx 28$ cm) and its center is shifted on the nominal interaction point by the fine tuning of the squeezers.
The transverse shape of the interaction region has an almost circular spatial distribution with a diameter of $\sigma_{\mathrm{T}} \approx 30$ μm. The luminosity lifetime is increased by using electrostatic separators which separate transversely the proton and antiproton bunches except at the collision regions. Then the "scraping" takes place, a procedure which shapes the beam transverse profile to its optimized configuration, in order to avoid detector damages due to the tails of the $p\bar{p}$ distributions entering the active volumes. The scraping is done by moving iron plates which act as collimators in the transverse plane toward the beam and sweep away the transverse beam halo. When the beam profile is narrow enough and the conditions are safely stable the detectors are powered and the data taking starts. This is the end of the injection procedure

called "shot".

The inter-bunch crossing is 396 ns and this defines an overall time constant which influences the whole detector design: on this parameter depends the choice of the active parts, the design of the readout electronics, the structure of the trigger, etc. The number of overlapping interactions N for each bunch crossing is governed by a Poisson distribution function of the instantaneous luminosity (see Figure 2.2). At

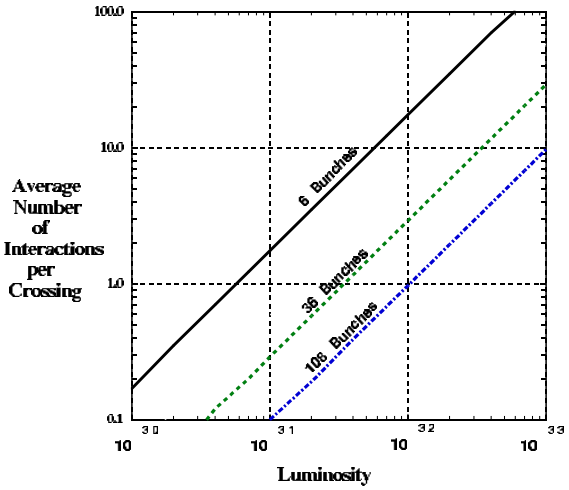

Figure 2.2: *Average number of interactions per crossing as a function of the luminosity (cm^{-2} s^{-1}) and the number of bunches circulating in the Tevatron.*

Tevatron's peak luminosities of $\mathcal{L} \approx 3 \times 10^{32}[\mathrm{cm}^{-2}\mathrm{s}^{-1}]$, $< N >$ is approximately 10. Each time that at least one of the CDF II triggers fires, an *event* is labeled with an increasing number. Events are grouped into *runs*; a run is a period of continuous[2] operation of the CDF II Data Acquisition (DAQ). Most parameter of the CDF II operations (e.g. the position of the beam) are stored in a database on a run-averaged format. While collisions are taking place the luminosity decreases exponentially[3] because of the beam-gas and beam-halo interactions. In the meantime, antiproton production and storage continues. When the antiproton stack is sufficiently large ($\simeq 4 \times 10^{12}$ antiprotons) and the circulating beams are degraded the detector high-voltages are switched off and the store is dumped. The beam is extracted via a switch-yard and sent to an absorption zone. Beam abortion can occur also accidentally when the temperature of a superconducting magnet shift above the critical value and a magnet quenches destroying the orbit of the beams. The time between the end of a store and the beginning of collisions of the next one is typically ~ 2 hr; during this time CDF II crew usually performs calibrations of the sub-detectors and

[2]Many different situations can require the Data Acquisition (DAQ) to be stopped and restarted including the need to enable or disable a subdetector, a change in the Trigger Table, a problem in the trigger/DAQ chain, etc.

[3]The decrease is about a factor of 3 (5) for a store of ~ 10 (20) hrs.

test runs with cosmics.

2.1.5 Tevatron status

The stated goal of Tevatron Run II was (1996) the accumulation of 2 fb^{-1} at $\sqrt{s}$ = 2 TeV with instantaneous luminosity peaks up to $2 \times 10^{32}[cm^{-2}s^{-1}]$. The current performance is well beyond these expectations. The center of mass energy is 1.96 TeV, the peak luminosity, as shown in Figure 2.3, is almost regularly $\sim 3.8 \times 10^{32}[cm^{-2}s^{-1}]$ (with usual peaks at $4 \times 10^{32}[cm^{-2}s^{-1}]$) and the crossing time is equal to 396 ns. From February 2002 to February 2010, ~ 6.7/fb were recorded on tape; these are the data used for this analysis. Figure 2.4 shows the trend of Tevatron's integrated and initial luminosity as function of time and store number; the Tevatron delivered until today ~ 10.3/fb (on tape ~ 8.5/fb).

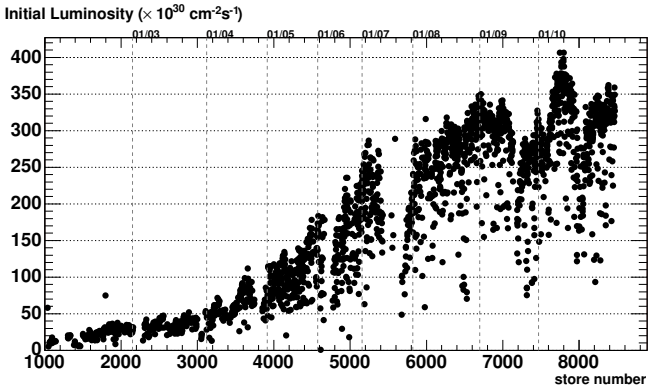

Figure 2.3: *Initial luminosity as a function of the time (or store number).*

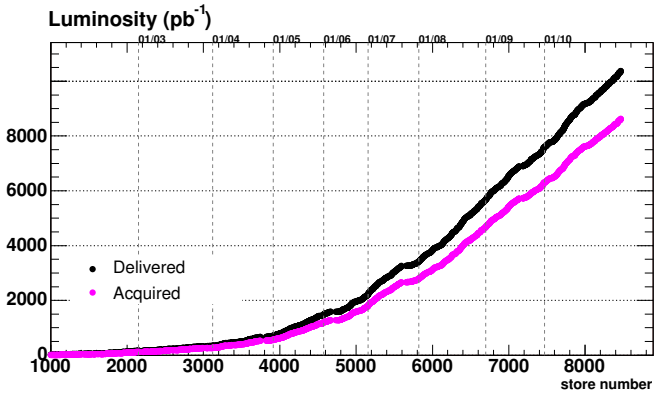

Figure 2.4: *Integrated luminosity as a function of the time (or store number).*

2.2 The CDF II experiment

The CDF II detector is a large multi purpose solenoidal magnetic spectrometer surrounded by 4π, fast, projective calorimeters and fine-grained muon detectors. It is installed at the BØ interaction point of the Tevatron (see Figure 2.1) to determine energy, momentum and, whenever possible, the identity of a broad range of particles produced in 1.96 TeV $p\bar{p}$ collisions. Several upgrades modified the design of the original facility commissioned in 1985; the most extensive upgrade started in 1995 and led to the current detector whose operation is generally referred to as Run II (see Figures 2.5 and 2.6).

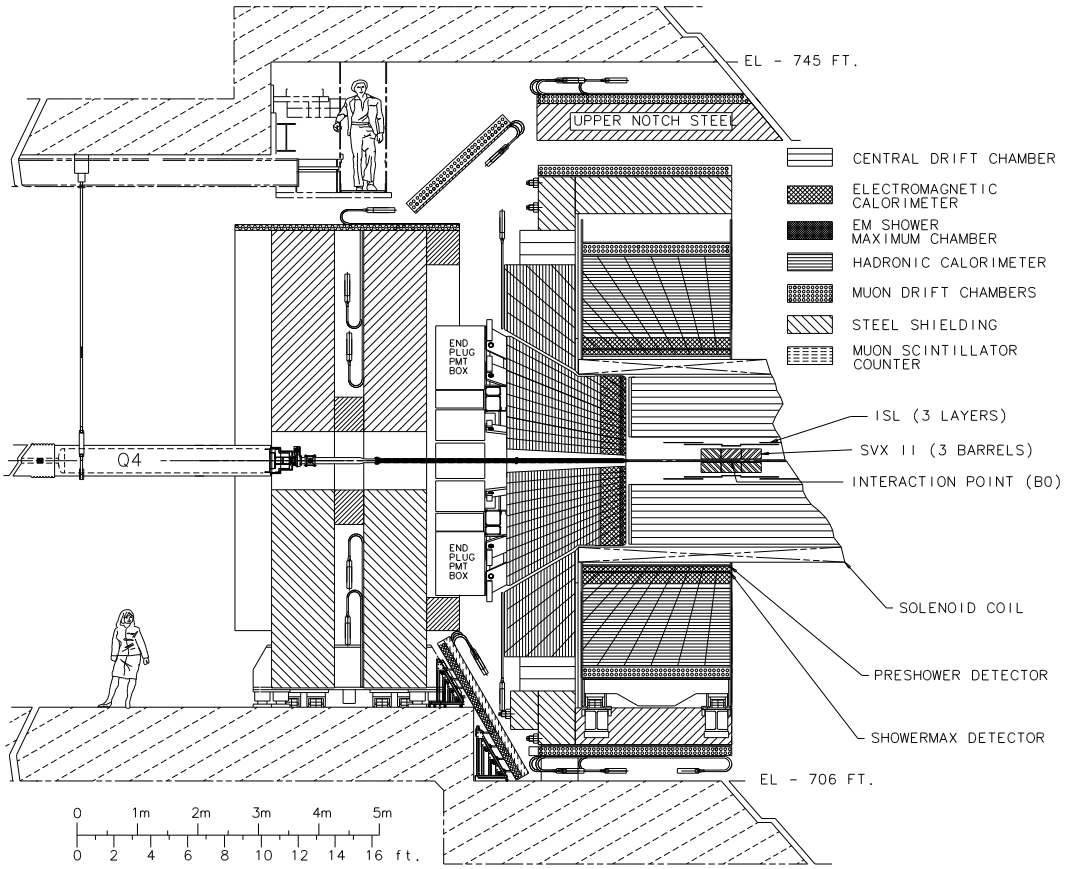

Figure 2.5: *Elevation view of one half of the CDF II detector.*

2.2.1 Coordinates system and notations

As shown in Figure 2.7, CDF II employs a right-handed Cartesian coordinates system with the origin in the BØ interaction point, assumed coincident with the center of the drift chamber. The positive z-axis lies along the nominal beam-line pointing

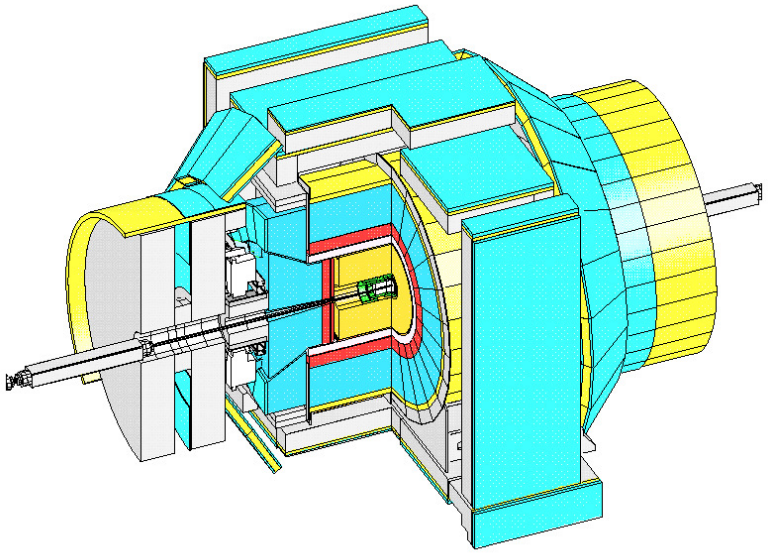

Figure 2.6: *3D view of the CDF II detector.*

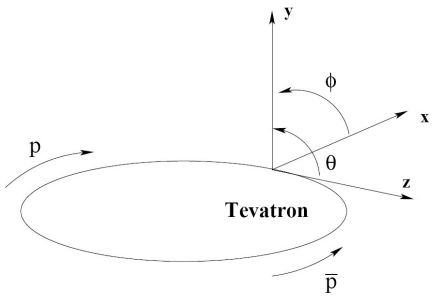

Figure 2.7: *CDF II Cartesian coordinates system.*

toward the proton direction (east). The (x, y) plane is therefore perpendicular to either beams, with positive y-axis pointing vertically upward and positive x-axis in the horizontal plane of the Tevatron, pointing radially outward with respect to the center of the ring.

Since the colliding beams of the Tevatron are unpolarized, the resulting physical observations are invariant under rotations around the beam line axis. Thus, a cylindrical (r, ϕ, z) coordinates system is particularly convenient to describe the detector geometry. Throughout this thesis, *longitudinal* means parallel to the proton beam direction (i.e., to the z-axis) and *transverse* means perpendicular to the proton direction, i.e., in the $(x, y) \equiv (r, \phi)$ plane.

Since the protons and antiprotons are composite particles, the actual interaction occurs between individuals partons (valence or sea quarks and gluons) contained within them. Each parton carries a varying fraction of the (anti)proton momentum,

not known on a event-by-event basis. As a consequence of the possible imbalance in the longitudinal components of the momenta of interacting partons, possible large velocities along $\hat{z}$ for the center-of-mass of the parton-level interaction may occur. In the hadron collisions environment, it is customary to use a variable invariant under $\hat{z}$ boosts as an unit of relativistic phase-space, instead of the polar angle θ. This variable is the *rapidity* defined as

$$y = \frac{1}{2} \ln\left[\frac{E + p \cdot \cos(\theta)}{E - p \cdot \cos(\theta)}\right] \tag{2.4}$$

where $(E, \vec{p})$ is the energy-momentum four-vector of the particle. Under a $\hat{z}$ boost to an inertial frame with velocity β, the rapidity of a particle transforms linearly, according to $y \to y' \equiv y + \tanh^{-1}(\beta)$, therefore y is invariant since $dy \equiv dy'$. However, a measurement of rapidity still requires a detector with accurate identification capabilities because of the mass term entering E. Thus, for practical reasons, it is often preferred to substitute y with its approximate expression η in the ultra-relativistic limit ($p \gg m$), usually valid for products of high-energy collisions:

$$y \xrightarrow{p \gg m} \eta + \mathcal{O}(m^2/p^2) \tag{2.5}$$

where the *pseudo-rapidity* is only function of θ:

$$\eta = -\ln \tan\left(\frac{\theta}{2}\right) \tag{2.6}$$

As the event-by-event longitudinal position of the actual interaction is distributed around the nominal interaction point with ~ 30 cm r.m.s width, it is useful to distinguish the *detector pseudo-rapidity*, η_{det}, measured with respect to the (0,0,0) nominal interaction point, from the *particle pseudo-rapidity*, η, measured with respect to the z_0 position of the real vertex where the particle originated[4].

Other convenient variables are the transverse component of the momentum with respect to the beam axis (p_T), the "transverse energy" (E_T) and the approximately Lorentz-invariant angular distance ΔR, defined as:

$$\vec{p}_T \equiv (p_x, p_y) \to p_T \equiv p \cdot \sin(\theta), \quad E_T \equiv E \cdot \sin(\theta) \quad \text{and} \quad \Delta R \equiv \sqrt{\eta^2 + \phi^2}. \tag{2.7}$$

2.2.2 Overview

CDF II is designed for measurements of a broad range of final states in $p\bar{p}$ collisions at high energy. A comprehensive description of the CDF II detector and its subsystems is given in [18].

[4] An idea of the difference is given by considering that $\eta_{\text{det}} \approx \eta \pm 0.2$ if the particle is produced at $z = 60$ cm from the nominal interaction point

CDF II (see Figure 2.5) is a three-story, 5000-ton approximately cylindric assembly of sub-detectors, ~ 15 m in length, ~ 15 m in diameter. The flow of final state particles in energetic hadronic collisions is well described by quantities of (pseudo)rapidity, transverse component of the momentum with respect to the beam axis and azimuthal angle around this axis. Consequently the CDF II detector was designed and constructed with an approximately cylindrically symmetric layout both in the azimuthal plane and in the *forward* ($z > 0$) – *backward* ($z < 0$) directions with spatial segmentation of its subcomponents roughly uniform in pseudorapidity and azimuth.
CDF II is composed of several specialized sub-systems each one designed to perform a different task. Its capabilities include high resolution charged particle tracking, electron and muon identification, low momentum π/K separation, precise secondary vertices proper time measurements, finely segmented sampling of energy flow coming from final state hadrons, electrons or photons, identification of neutrinoss via transverse energy imbalance.
A 1.4 T solenoidal magnetic field is maintained in the region with $r \leq 150$ cm and $|z| \leq 250$ cm by circulating a 4650 A current through 1164 turns of a Nb-Ti/Cu superconducting coil. The field is oriented along the positive $\hat{z}$ direction and is uniform at the 0.1% level in the $|z| \leq 150$ cm volume, where tracking measurements are made[5]. The field is continuously monitored via NMR probes during data taking and any deviation from the mapped values is applied as a correction to measured track momenta. The threshold to escape radially the magnetic field for a particle is $p_T > 280$ MeV/c while the trajectory of a $p_T = 30$ GeV/c particle deviates only 1.6 cm from a straight path of 150 cm. The solenoid is 4.8 m in length, 1.5 m in radius, 0.85 X_0 in radial thickness[6] and is cooled by forced flow of two-phase helium. Outside the coil the field flux is returned through a steel yoke to avoid having the fields interfere with the proper operations of the calorimeter's PMTs.
The detector is divided conventionally into two main polar regions. In the following, if not otherwise stated, we shall refer to the detector volume contained in the $|\eta_{\text{det}}| < 1$ as the *central region*, while the *forward region* indicates the detector volume comprised in $1 < |\eta_{\text{det}}| < 3.6$.

2.2.3 Tracking system

Three-dimensional charged particle tracking is achieved through an integrated system consisting of three silicon inner subdetectors and a large outer drift chamber, all contained in a superconducting solenoid. The 1.4116 T magnetic field and the 138 cm total lever arm provide an excellent tracking performance (see Figure 2.8).

[5]The tiny non-uniformities, mapped out during the detector construction, are treated as a small perturbation within the track fitting software.

[6]The symbol X_0 indicates the radiation length. This value has to be intended for normally incident particles.

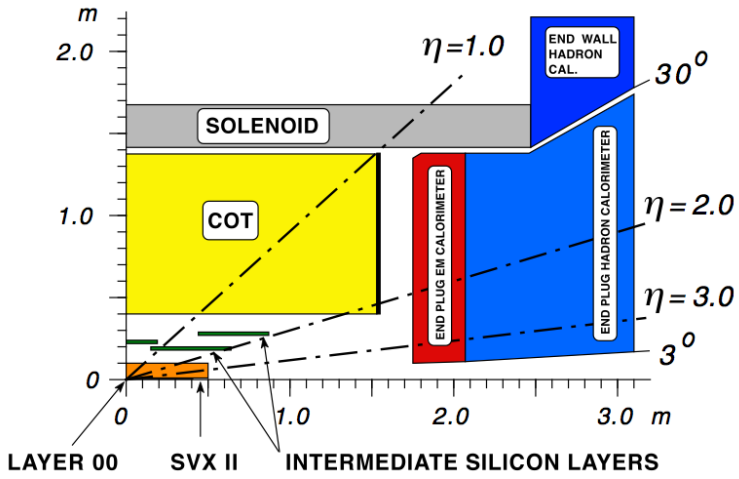

Figure 2.8: *Elevation view of one quadrant of the inner portion of the CDF II detector showing the tracking volume surrounded by the solenoid and the forward calorimeters.*

2.2.3.1 Layer ØØ (L ØØ)

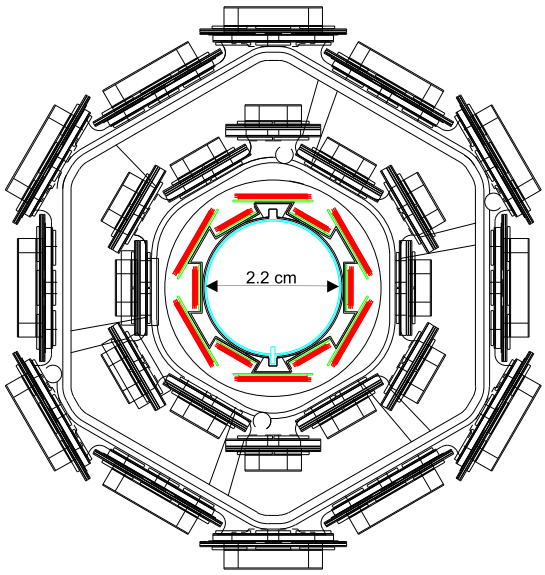

Figure 2.9: *Section that shows LØØ arrangement.*

Layer ØØ (LØØ) is the innermost layer of the microvertex silicon detector (see Figure 2.9). It consists of one layer of single sided AC-coupled silicon sensors which covers longitudinally the beryllium beam pipe along 80 cm. The state-of-the-art 7.85 cm long silicon sensors of LØØ can be biased to very high voltages ($\mathcal{O}$(500 V))

allowing to maintain a good signal-to-noise ratio even after high integrated radiation dose ($\mathcal{O}$(5 MRad)). The radiation hardness of such sensors allowed their installation at radii of 1.35 and 1.62 cm supported by a mechanical structure in direct contact with the beam pipe. The LØØ strips are parallel to the beam axis allowing the first sampling of the track within the $r-\phi$ plane; the inter-strip pitch is 25 μm but the read-out strip are alternated with floating ones resulting in 50 μm of readout pitch and a resolution of the $r-\phi$ charged particle's impact point of about 10 μm.
The signals of the 13,824 channels are fed via special optical fiber cables to the front-end electronic which is placed in a region separated from the sensors and less exposed to the radiation. The operation temperature of this device is around 0° C maintained by a forced flux of under-pressurized[7] gas through tiny aluminum pipes installed in between the sensor and the beam-pipe. The cooling circuit increases the total mass of the LØØ which is about $0.01 \cdot X_0$ where it passes the cooling pipes and reduces to $0.006 \cdot X_0$ where only sensors contribute.

2.2.3.2 Silicon VerteX detector II (SVX II)

The Silicon VerteX detector II (SVX II) is a fine resolution silicon microstrip vertex detector which provides five 3D samplings of a track between 2.4 and 10.7 cm of radial distance from the beam (see Figure 2.8). Its cylindrical geometry coaxial with the beam is segmented along z into three *mechanical barrels* for a total length of 96 cm which provides complete geometrical coverage within $|\eta_{\text{det}}| < 2$ (see Figure 2.10a). Each barrel consists of twelve azimuthal wedges each of which subtends approximately[8] 30°. One wedge of a given barrel comprises 5 concentric and equally spaced layers of silicon sensors installed at radii 2.45 (3.0), 4.1 (4.6), 6.5 (7.0), 8.2 (8.7) and 10.1 (10.6) cm from the beam as shown in Figure 2.10b.

Sensors in a layer are arranged into independent readout units, called *ladders* (or electrical barrels). The ladder components are two double sided rectangular 7.5 cm long sensors and the *hybrid* which is a multilayer board where all the front end electronics, biasing circuits and fan-out are allocated. The two silicon sensors, accurately aligned along their major axis, are glued end-to-end on a carbon-fiber support with wirebonds connections joining the strips on one sensor to the strips of the next. It results in strips with an effective length of 15 cm in turn wirebonded to the front-end electronics of the hybrid which is mounted at one end of the carbon fiber support. Two ladders are longitudinally juxtaposed head-to-head within a barrel's layer, in order to leave the two hybrids at the two outside extremities of the barrel.
The active surface consists of double-sided, AC-coupled silicon sensors having mi-

[7] The pressure of the cooling fluid is maintained under the atmospheric pressure to avoid dangerous leaks of fluid in case of damaged cooling pipe.

[8] There is a small overlap between the edges of two adjacent wedges, which helps in wedge-to-wedge alignment.

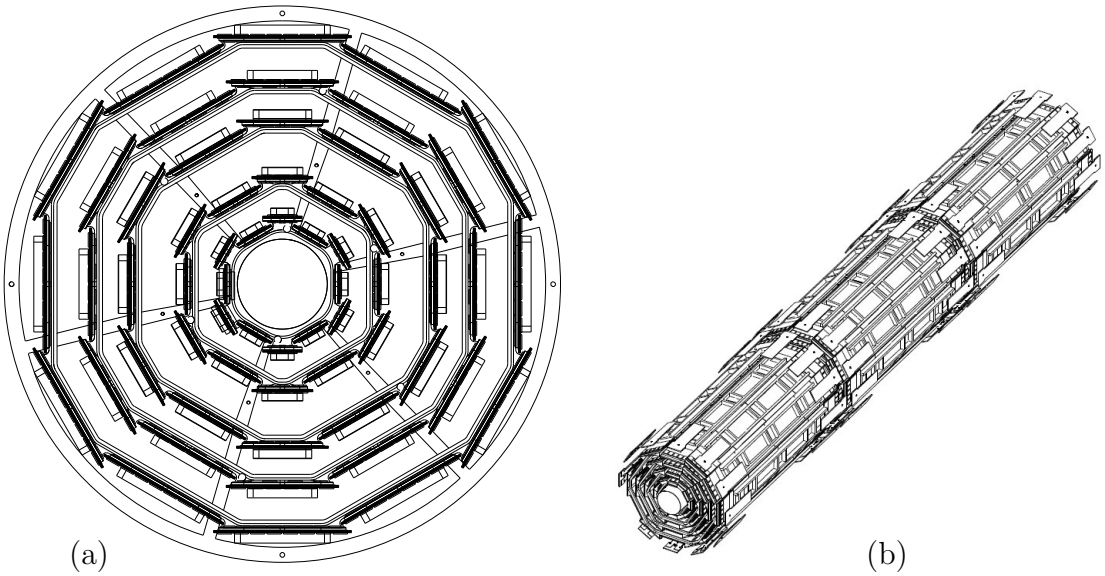

(a) (b)

Figure 2.10: *Schematic illustration of the three instrumented mechanical barrels of SVX II (a) and of the section view of a SVX II barrel in the* (r, ϕ) *plane (b).*

crostrips implanted on a 300 μm thick, high resistivity bulk. Bias is applied through integrated polysilicon resistors. There are three different possible sort of strip orientations in each sensor's side: $r - \phi$ (axial) strips oriented parallel to the beam axis, small angle stereo (SAS) strips whose orientation is tilted by 1.2° with respect to the beam axis and the 90° stereo strips which lie in the transverse plane. All the five layers have axial strips on one side, three of the other sides have 90° stereo and two have SAS strips.
The charge pulse from each strip flows to a channel of *SVX3D*, the radiation-hard front-end chip. SVX3D operates readout in "sparse-mode" which means that only signals above a threshold are processed. SVX3D samples the pedestal event-by-event and subtracts it from the signal. The discriminated differential pulse from each one of the 405,504 channels is preamplified, ADC-converted to a digital string and fed through neighbor-logic[9] to the DAQ chain. The measured average signal-to-noise ratio is S/N $\geq$ 10 with a single hit efficiency greater than 99%.
Impact parameter resolution for central high momentum tracks are $\sigma_\phi < 35$ μm and $\sigma_z < 60$ μm. To prevent thermal expansion, relative detector motion, increased leakage current and chip failure due to thermal heating the SVX II is held at roughly constant temperature of 10-15° C through the operation of a water-glycol cooling system whose pipes run all below the detector. The average material of SVX II corresponds to $0.05 \cdot X_0$.

[9]In presence of a channel over threshold also the signal of the neighbor channels is accepted allowing clustering of the hits.

2.2.3.3 Intermediate Silicon Layer (ISL)

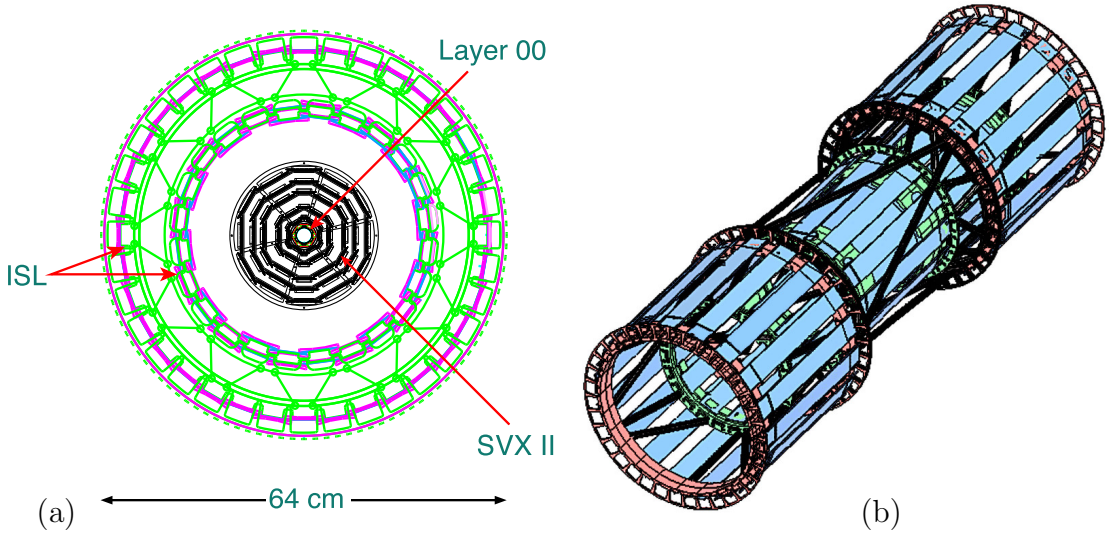

Figure 2.11: *Schematic illustration of the three instrumented mechanical barrels of ISL (a) and of the section view of a ISL barrel in the* (r, ϕ) *plane (b).*

The Intermediate Silicon Layer detector, shown in Figure 2.11, is a silicon tracker placed at intermediate radial distance between the SVX II and the drift chamber (see Figure 2.8). The polar coverage extends to $|\eta_{\text{det}}| < 2$. In the central region ISL consist of a single layer of silicon installed over a cylindrical barrel at radius of 22 cm. In the forward region, two layers of silicon are placed on concentric barrels at radii of 20 and 28 cm. Each silicon layer is azimuthally divided into a 30° wedge structure matching SVX II's one. The basic readout unit is the ISL *ladder* which is similar to the SVX II ladder but consists of three, instead of two, sensors wirebonded in series resulting in a total active length of 25 cm.
ISL employs 5.7×7.5 cm^2 double sided AC-coupled 300 μm thick sensors. Each sensor has axial strips on one side and SAS strips on the other. As in SVX II, signals from the 303,104 channels are read by SVX3D chips. The average mass of the detector is $0.02 \cdot X_0$ for normally incident particles.

2.2.3.4 Central Outer Tracker (COT)

The outermost tracking volume of CDF II is a large open cell drift chamber called the Central Outer Tracker (COT), see Figure 2.12.
The COT has a coaxial bi-cylindrical geometry and extends, within the central region, from 40 to 138 cm radially from the beam axis. The chamber contains 96 radial layers of 0.40 μm diameter gold-plated tungsten sense (anode) wires arranged into 8 *superlayers* (SL), see Figure 2.12a. Each SL samples the path of a charged particle

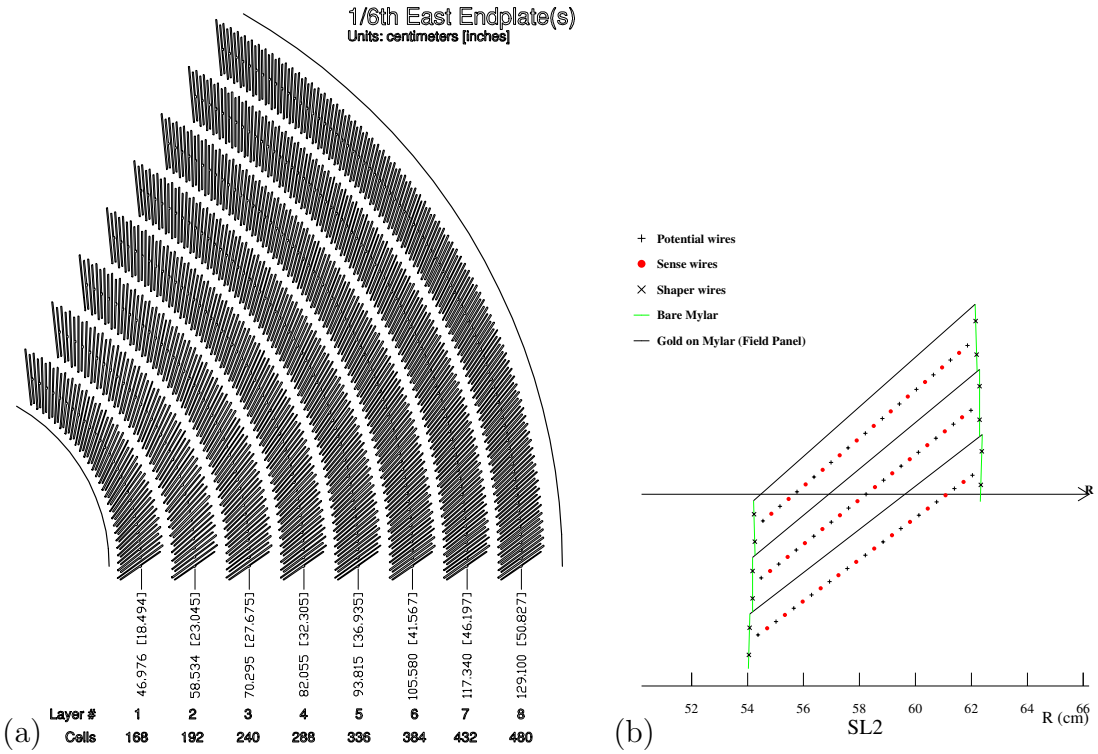

Figure 2.12: *A 1/6 section of the COT end-plate (a). For each super-layer is given the total number of cells, the wire orientation (axial or stereo) and the average radius [cm]. The enlargement shows in details the slot were wire planes (sense) and field sheet (field) are installed. A sketch of an axial section of three cells in super-layer 2 (b). The arrow shows the radial direction.*

at 12 radii (spaced 0.762 cm apart) where sense wires are strung. Four SL have their constituent sense wires oriented parallelly to the beam axis in order to measure the hit coordinates in the $r-\phi$ plane. These are radially interleaved with four *stereo* superlayers having wires canted at angles of either $+3°$ or -3° with respect to the beamline. Combined readout of stereo and axial SLs allows the measurement of the $r-z$ hit coordinates.

Each superlayer is azimuthally segmented into open drift cells. A drift cell, as shown in Figure 2.12b, contains a row of 12 sense wires alternating with thirteen 0.40 μm diameter gold-plated tungsten potential wires which control the gain on the sense wires, optimizing the electric field intensity. The cathode of the detection circuit is the *field panel* which closes the cell along the azimuthal direction. It is made of gold on a 0.25 mm thick Mylar sheet and defines the fiducial volume of a cell. The electric field strength is 2.5 kV/cm. Innermost and outermost radial extremities of a cell are both closed mechanically and electrostatically by the *shaper panels*, which are Mylar strips carrying field-shaping wires attached. The architecture of the cell allows the containment of a possible broken wire inside only one cell and its dimen-

sions bound to 0.88 cm the maximum drift distance.
Wire planes are not aligned with $\hat{r}$. A 35° azimuthal tilt is provided in order to offset the Lorentz angle of the drift paths which results from the combined effect of crossed electrical and magnetic field and the characteristics of the gas mixture. Moreover the tilted-cell geometry helps in the drift-velocity calibration as every high-p_T (radial) track samples the full range of drift distances within each superlayer. Further benefit of the tilt is that the left-right ambiguity[10] is cleared-up for track coming from the origin since the ghost track in each superlayer appears rotated of a large azimuthal angle becoming unfittable by pattern recognition.
The volume of the COT is filled with an $\mathsf{Ar(50\%)/Ethane(35\%)/CF_4(15\%)}$ gas mixture. Drift electrons follow approximately azimuthal trajectories at speed $v \sim 100$ μm/ns. The resulting maximum drift time is about 100 ns, well smaller than the inter-bunch spacing 396 ns, providing the read-out and processing of the COT data available for the Level 1 trigger.
The analog pulses from the 30,240 sense wires flow to preamplifiers where are amplified and shaped. The discriminated differential output encodes charge information in its width to be used for dE/dx measures and is fed to a TDC which records leading and trailing edge of the signals in 1 ns bins.
The COT has a 99% efficiency on tracks with measured single hit resolution $\sigma_{\rm hit} \simeq 175$ μm and p_t resolution is $\sigma_{p_T}/p_T^2 \simeq 0.13\%$ c/GeV. The material of the COT is about $0.016 \cdot X_0$ for tracks at normal incidence.

2.2.3.5 Tracking performance.

The only physical objects used in this analysis are the *tracks*. Within a uniform axial magnetic field in vacuum, the trajectory of a charged particle produced with non-zero initial velocity in the bending plane of the magnet is described by an helix. The arc of an helix described by a charged particle in the magnetic volume of CDF II is parameterized using three transverse and two longitudinal parameters:

C – signed helix (half-)curvature, defined as $C \equiv \frac{q}{2R}$, where R is the radius of the helix. This is directly related to the transverse momentum: $p_T = \frac{cB}{2|C|}$ (where B is the intensity of the magnetic field).

φ_0 – ϕ direction of the particle at the point of closest approach to the beam.

d_0 – signed impact parameter, i.e. the distance of closest approach to the z-axis, defined as $d_0 \equiv q \cdot (\sqrt{x_c^2 + y_c^2} - R)$, where (x_c, y_c) are the coordinates of the beam in the transverse plane.

[10] Each pulse on a given wire has a two fold ambiguity corresponding to the two incoming azimuthal drift trajectories. The signals from a group of nearby radially wires will satisfy the configuration for two tracks, one from the actual particle trajectory and another "ghost track" originated by the two fold ambiguity.

λ – the helix pitch, i.e. $\cot(\theta)$, where θ is the polar direction of the particle at the point of its closest approach to the beam. This is directly related to the longitudinal component of the momentum: $p_z = p_T \cdot \cot(\theta)$.

z_0 – the z coordinate of the point of closest approach to the beam.

The trajectory of a charged particle satisfies the following equations:

$$x = r \cdot \sin(\varphi) - (r + d_0) \cdot \sin(\varphi_0) \tag{2.8}$$

$$y = -r \cdot \cos(\varphi) + (r + d_0) \cdot \cos(\varphi_0) \tag{2.9}$$

$$z = z_0 + s \cdot \lambda \tag{2.10}$$

where s is the projected length along the track, $r = 1/2C$ and $\varphi = 2Cs + \varphi_0$. The reconstruction of a charged-particle trajectory (a track) consists of determining the above parameters through an helical fit of a set of spatial measurements ("hits") reconstructed in the tracking detectors by clustering and pattern-recognition algorithms. The helical fit takes into account field non-uniformities and scattering in the detector material.

For this analysis only tracks reconstructed with both silicon and COT hits were used (*SVX+COT* tracks) because of three main reasons:

- silicon stand-alone tracking (*SVX-Only* tracks) becomes important in the region $1 \leq |\eta| \leq 2$ where the COT coverage is incomplete (this region of acceptance is excluded in our analysis[11], since the reconstruction efficiency out of this region is too low);

- in the central region only track with a $p_T < 0.28$ GeV/c have SVX-Only informations and this value is well below our minimum request;

- COT stand-alone tracking (*COT-Only* tracks) has an insufficient impact parameter resolution for our needs;

All SVX+COT tracks are first fit in the COT and then extrapolated inward to the silicon. This approach guarantees fast and efficient tracking with high track purities. The greater radial distance of the COT with respect to the silicon tracker results in a lower track density and consequent fewer accidental combination of hits in the track reconstruction.

[11] Except if otherwise stated.

COT performance. All the channels of the COT are still properly working and its efficiency for tracks is typically 99%. The single-hit resolution is about 140 μm, including a 75 μm contribution from the ≈ 0.5 ns uncertainty on the measurement of the $p\bar{p}$ interaction time. Internal alignments of the COT cells are maintained within 10 μm using cosmic rays and curvatures effects from gravitational and electrostatic sagging are under control within 0.5% by equalizing the difference of E/p between electrons and positrons as a function of $\cot(\theta)$. The typical resolutions on track parameters are : $\sigma_{p_T}/p_T^2 \approx 0.0015$ c/GeV, $\sigma_{\varphi_0} \approx 0.035°$, $\sigma_{d_0} \approx 250$ μm, $\sigma_\theta \approx 0.17°$ and $\sigma_{z_0} \approx 0.3$ cm for tracks fit with no silicon information or beam constraint.

Performance with the silicon detectors. The silicon information improves the impact parameter resolution of tracks which, depending on the number (and radial distance) of the silicon hits, may reach $\sigma_{d_0} \approx 20$ μm (not including the transverse beam size). This value, combined with the $\sigma_{\mathrm{T}} \approx 30$ μm transverse beam size, is sufficiently small with respect to the typical transverse decay-lengths of heavy flavors (a few hundred microns) to allow separation of their decay vertices from production vertices. The silicon tracker improves also the stereo resolutions up to $\sigma_\theta \approx 0.06°$, and $\sigma_{z_0} \approx 70$ μm, while the transverse momentum and the azimuthal resolutions remain approximately the same of COT-Only tracks.

2.2.4 Other CDF II subdetectors

In this section the subdetectors not used in this analysis are briefly discussed and described.

2.2.4.1 Time OF Flight (TOF)

The Time of Flight detector (TOF) is a cylindrical array made of 216 scintillating bars and it is located between the external surface of the COT and the cryostat containing the superconducting solenoid (see Figure 2.13). Bars are 280 cm long and oriented along the beam axis all around the inner cryostat surface at an average radial distance of 140 cm. Both longitudinal sides of the bars collect the light pulse into PhotoMulTipliers (PMT) and measure accurately the timing of the two pulses. The time between the bunch crossing and the scintillation signal in these bars defines the β of the charged particle while the momentum is provided by the tracking. PID information is available through the combination of TOF information and tracking measurements:

$$m = \frac{p}{c}\sqrt{\frac{c^2t^2}{l^2} - 1} \tag{2.11}$$

where t is the time measured by the TOF, l is the particle's path lenght and p is the momentum measured by the tracking system. The measured mean time resolution is now 110 ps. This guarantees a separation between charged pions and kaons with

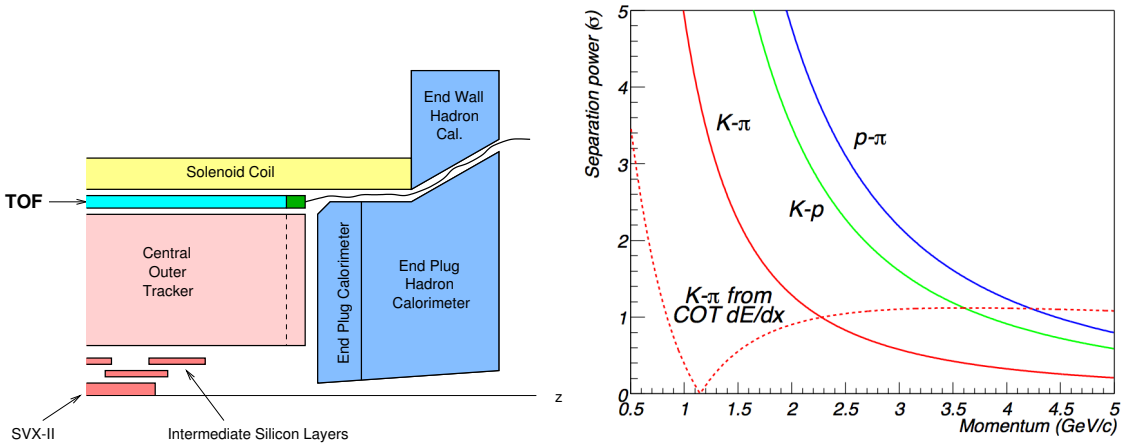

Figure 2.13: *Elevation view of one quadrant of the inner portion of the CDF II detector showing the TOF location (left); K and π time of flight difference expressed in sepatation power as a function of the momentum. The dashed line represents the COT K-π separation power obtained through the dE/dx measurement (right).*

$p_T \lesssim 1.6$ GeV/c equivalent to 2σ, assuming Gaussian distributions, as shown in Figure 2.13.

2.2.4.2 Calorimeters

Outside the solenoid, scintillator-based calorimetry covers the region $|\eta_{\text{det}}| \leq 3.6$; it is devoted to the measurement of the net energy deposition of photons, electrons and hadrons using the *shower sampling* technique.
The basic structure consists of alternating layers of passive absorber and plastic scintillator. Neutral particles and charged particles with a transverse momentum greater than about 350 MeV/c are likely to escape the solenoid's magnetic field and penetrate into the CDF II calorimeters. Here particles undergo energy loss (striking the absorber material) and produce daughter particles, which also interact in a cascade process, giving rise to a *shower* of particles. Showers propagate through many layers of the absorber before they exhaust their energy generating a detectable signal, roughly proportional to the number of particles in the shower, within the active scintillator layers. The sum of the signals collected by all the sampling active layers is proportional to the energy of the incident particle.
The CDF II calorimeters are finely segmented in solid angle around the nominal collision point and coarsely segmented radially outward from the collision point (in-depth segmentation). Angular segmentation is organized in projective *towers*. Each tower has a truncated-pyramidal architecture having the imaginary vertex pointing to the nominal interaction point and the base is a rectangular cell in the $(\eta_{\text{det}}, \varphi)$ space. Radial segmentation of each tower instead consists of two compartments, the

inner (closer to the beam) devoted to the measure of the electromagnetic component of the shower and the outer devoted to the measure of the hadronic fraction of energy. These two compartments are read independently through separated electronics channels.
A different fraction of energy release in the two compartments distinguishes photons and electrons from hadronic particles. CDF II calorimetry is divided in several independent subsystems presented in the following subsections.

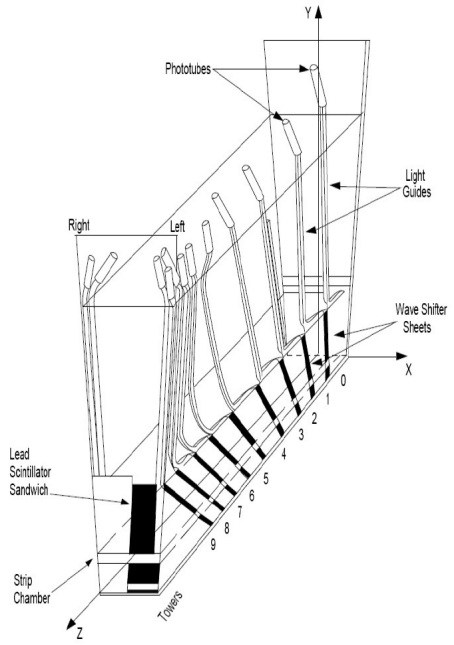

Figure 2.14: *Schematic illustration of an azimuthal sector of the central electromagnetic calorimeter.*

Central region (CEM, CHA, WHA) The radial extension of the calorimeters in the central region is 1.73 m < r < 3.5 m. The Central ElectroMagnetic calorimeter (CEM) is constructed as four azimuthal arches (NE, NW, SE, SW) each of which subtends 180° and is divided into twelve 15° wedges (see Figure 2.14). A wedge consists of 31 layers of 5 mm thick polystyrene scintillator interleaved with 30 aluminum-clad lead 3.2 mm thick sheets, divided along η_{det} into ten towers ($\Delta\eta_{\text{det}} \approx 0.11$ per tower). To maintain a constant thickness in X_0, compensating the $\sin(\theta)$ variation between towers, some lead layers are replaced with increasing amounts of acrylic as a function of η_{det}[12]. Light from each tower is collected by sheets of acrylic wavelength shifter at both azimuthal tower boundaries and guided to two

[12]The number of lead layers varies from 30 in the innermost ($|\eta_{\text{det}}| \approx 0.06$) tower to 20 in the outermost ($|\eta_{\text{det}}| \approx 1.0$).

phototubes per tower. The spatial resolution of the CEM is about 2 mm. The outer two towers in one wedge (known as *chimney towers*) are missing to allow solenoid access, for a resulting total number of 478 instrumented towers.
At a radial depth of $5.9 \cdot X_0$, which is approximately the depth corresponding to the peak of shower development, the CEntral Strip multi-wire proportional chambers (CES) measure the transverse shower shape with ~ 1.5 cm segmentation. A further set of multi-wire proportional chambers, the Central Pre-Radiator (CPR) is located in the gap between outer surface of the solenoid and the CEM. It monitors eventual photon conversions started before the first CEM layer. Phototube gains are calibrated once per store using an automated system of Xenon or LED light flashers.
The hadronic compartment is the combination of two sub-systems: the Central HAdronic (CHA) and Wall HAdronic (WHA) calorimeters. Analogously as in the CEM, in both systems four "C"-shaped arches contain 48 wedges. Each CHA wedge is segmented into 9 $\eta_{\rm det}$ towers matching in size and position the CEM towers. The WHA wedge instead consists of 6 towers of which three are matching CHA towers. Radially a CHA tower is constructed of 32 layers of 2.5 cm thick steel absorber alternating with 1.0 cm thick acrylic scintillator. WHA towers structure is similar but there are only 15 layers of absorber which is 5.1 cm thick.

The total thickness of the electromagnetic section corresponds to approximately $19 \cdot X_0$ ($1 \cdot \lambda_{\rm int}$, where $\lambda_{\rm int}$ is the pion nuclear absorption length in units of g cm^{-2}), for a relative energy resolution $\sigma_E/E = 13.5\%/\sqrt{E \cdot \sin(\theta)} \oplus 2\%$[13]. The total thickness of the hadronic section corresponds to approximately $4.5 \cdot \lambda_{\rm int}$, for an energy resolution of $\sigma_E/E = 50\%/\sqrt{E \cdot \sin(\theta)} \oplus 3\%$ for the central and $\sigma_E/E = 75\%/\sqrt{E \cdot \sin(\theta)} \oplus 4\%$ for the end-wall.

Forward region (PEM, PHA) The coverage of the $1.1 \leq |\eta_{\rm det}| \leq 3.6$ region relies on the scintillating tile *Plug* calorimeter which is composed of two identical devices, one installed in $\eta_{\rm det} > 0$ region and the other in the $\eta_{\rm det} < 0$. Each of these two halves has electromagnetic and hadronic compartments (see Figure 2.15).
Each half of the absorber of the Plug ElectroMagnetic calorimeter (PEM) consists in 23 *doughnuts*-shaped lead plates, 2.77 m in outer diameter, which have a central hole where the beam pipe is allocated. Each plate is made out of 4.5 mm thick calcium-tin-lead sandwiched between two 0.5 mm thick stainless-steel sheets. Between the absorber plates are inserted the 4 mm thick scintillator *tiles* organized azimuthally in 15° triangularly-shaped wedges. The signal of each tile is collected independently by embedded wavelength-shifter fibers which guide it to the photomultipliers. A preshower detector consist of a thicker (10 mm) amount of scintillator installed in the first layer of PEM, while shower maximum sampling is performed

[13]The first term is called the "stochastic" term and derives from the intrinsic fluctuations of the shower sampling process and of the PMT photo-electron yield. The second term, added in quadrature, depends on the calorimeter non-uniformities and on the uncertainty on the calibrations. All energies are in GeV.

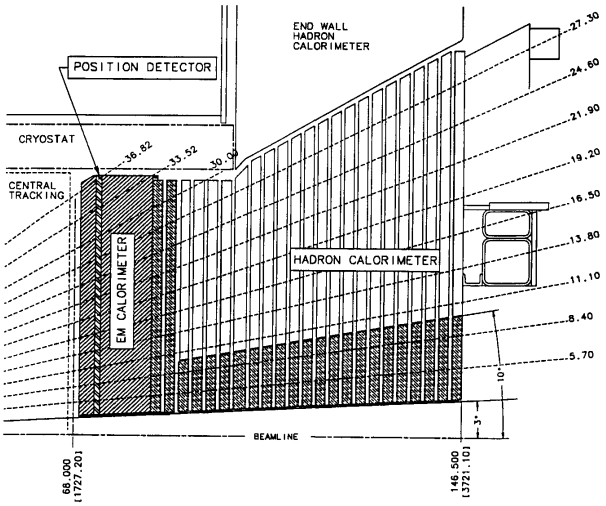

Figure 2.15: *Elevation view of one quarter of the plug calorimeter.*

at radial depth of $\sim 6 \cdot X_0$ by two tilted layers of scintillator strips (pitch 5 mm). Each half of the hadronic compartment, Plug HAdronic calorimeter (PHA), is azimuthally subdivided in 12 wedge-shaped modules each subtending 30°. In depth each module consists of 23 layers of 5 cm thick iron absorber alternated with 6 mm scintillator layers. Within each sampling layer the scintillator is arranged in tiles similar to those used in the PEM.

The total thickness of the electromagnetic section corresponds to approximately 21 $\cdot X_0$ (1 $\cdot \lambda_{\text{int}}$), for an energy resolution of $\sigma_E/E = 16\%/\sqrt{E \cdot \sin(\theta)} \oplus 1\%$. The total thickness of the hadronic section corresponds to approximately 7 $\cdot \lambda_{\text{int}}$, for an energy resolution of $\sigma_E/E = 74\%/\sqrt{E \cdot \sin(\theta)} \oplus 4\%$.

2.2.4.3 Muon system (CMU, CMP, CMX, IMU)

CDF II is equipped with scintillating counters and drift tubes installed at various radial distances from the beam to detect muons and shielded by the iron structure of the inner detector (see Figure 2.16). Scintillators serve as trigger and vetoes while the drift chambers measure the φ coordinate using the absolute difference of drift electrons arrival time between two cells and the z coordinate by charge division. These systems cover the whole range of pseudorapidity $|\eta_{\text{det}}| < 2$ and are used only to identify the penetrating muon reconstructing a small segment of their path (*stub*) sampled by the chambers. The momentum measurement is performed by pointing back the stub to the corresponding track in the COT. The shield is constituted by the iron of the calorimeter, the return yoke and further steel walls intended to filter out the punch-through of hadrons. Different muon sub-systems cover different geometrical regions. In the $|\eta_{\text{det}}| < 0.6$ region moving outward from the beam

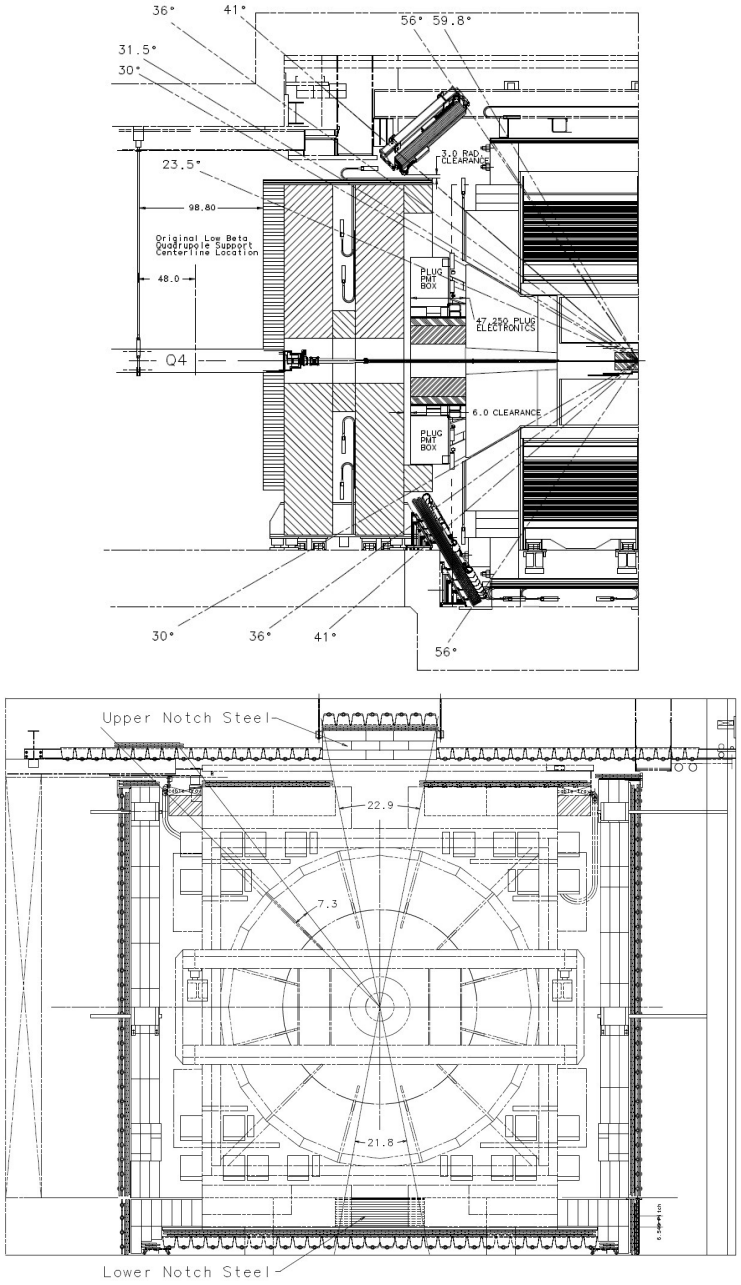

Figure 2.16: *Elevation (top) and section views (bottom) of the muon system.*

we encounter the inner CMU (Central MUon detector) chambers at radial distance of 3.5 m. Approximately $5.4 \cdot \lambda_{\text{int}}$ of material[14] separate the luminous region from the CMU resulting in about 1/220 high energy hadrons traversing the calorimeter

[14]This defines also a p_T threshold for muons reaching the CMU which is approximately 1.4 GeV/c.

unchecked. In order to recognize and discard them, the CMP (Central Muon uPgrade) chambers lie in the same η_{det} region separated radially from the CMU by a 60 cm thick wall of steel achieving a rejection of 95% of the fake muons.
The muon coverage in the $0.6 < |\eta_{\text{det}}| < 1$ volume is ensured by the CMX (Central Muon eXtension) chambers, embedded in scintillator counters and placed at radius of 3.5 m. The Intermediate MUon (IMU) detectors are instead drift tubes covering the pseudorapidity range of $1 < |\eta_{\text{det}}| < 2$.
CDF II triggers on muons only emerging at $|\eta_{\text{det}}| < 1.5$ where the muon coverage is segmented with sufficient granularity to survive high occupancies. The granularity of muon devices in the forward regions is less fine and not adequate for triggering but sufficient for offline muon assignation to high p_T tracks going through that region.

2.2.5 Cherenkov Luminosity Counters (CLC)

The luminosity ($\mathcal{L}$) is inferred from the average number of inelastic interactions per bunch crossing ($< N >$) according to:

$$< N > \cdot f_{\text{b.c.}} = \sigma_{\text{p}\bar{\text{p}}\text{-in.}} \cdot \varepsilon \cdot \mathcal{L} \tag{2.12}$$

where the bunch-crossing frequency ($f_{\text{b.c.}}$) is precisely known from the Tevatron RF, $\sigma_{\text{p}\bar{\text{p}}\text{-in.}} = 59.3 \pm 2.3$ mb is the inelastic $p\bar{p}$ cross-section resulting from the averaged CDF and E811 luminosity-independent measurements at $\sqrt{s} = 1.8$ TeV [20, 21] and extrapolated to $\sqrt{s} = 1.96$ TeV and ε is the efficiency to detect an inelastic scattering.

The Cherenkov Luminosity Counters (CLC) are two separate modules, covering the $3.7 \leq |\eta_{\text{det}}| \lesssim 4.7$ range symmetrically in the forward and backward regions (see Figure 2.17). Each module consists of 48 thin, 110–180 cm long, conical, isobutane-filled Cherenkov counters. They are arranged around the beam-pipe in three concentric layers and point to the nominal interaction region. The base of each cone, 6–8 cm in diameter and located at the furthest extremity from the interaction region, contains a conical mirror that collects the light into a PMT, partially shielded from the solenoidal magnetic field. Isobutane guarantees high refraction index and good transparency for ultraviolet photons. With a Cherenkov angle $\theta_C = 3.4°$, the momentum thresholds for light emission are 9.3 MeV/c for electrons and 2.6 GeV/c for charged pions. Prompt charged particles from the $p\bar{p}$ interaction are likely to traverse the full counter length, thus generating large signals and allowing discrimination from the smaller signals of particles emitted at the same angle due to the beam halo or to secondary interactions. In addition, the signal amplitude distribution shows distinct peaks for different particle multiplicities entering the counters. This allows a measurement of $< N >$ with 4.4% relative uncertainty in the luminosity range $10^{31} \leq \mathcal{L} \leq 10^{32}$ [$\text{cm}^{-2}\text{s}^{-1}$]. This accuracy, combined with the relative uncertainty on the inelastic $p\bar{p}$ cross-section, results in an instantaneous luminosity measured with 5.8% relative uncertainty.

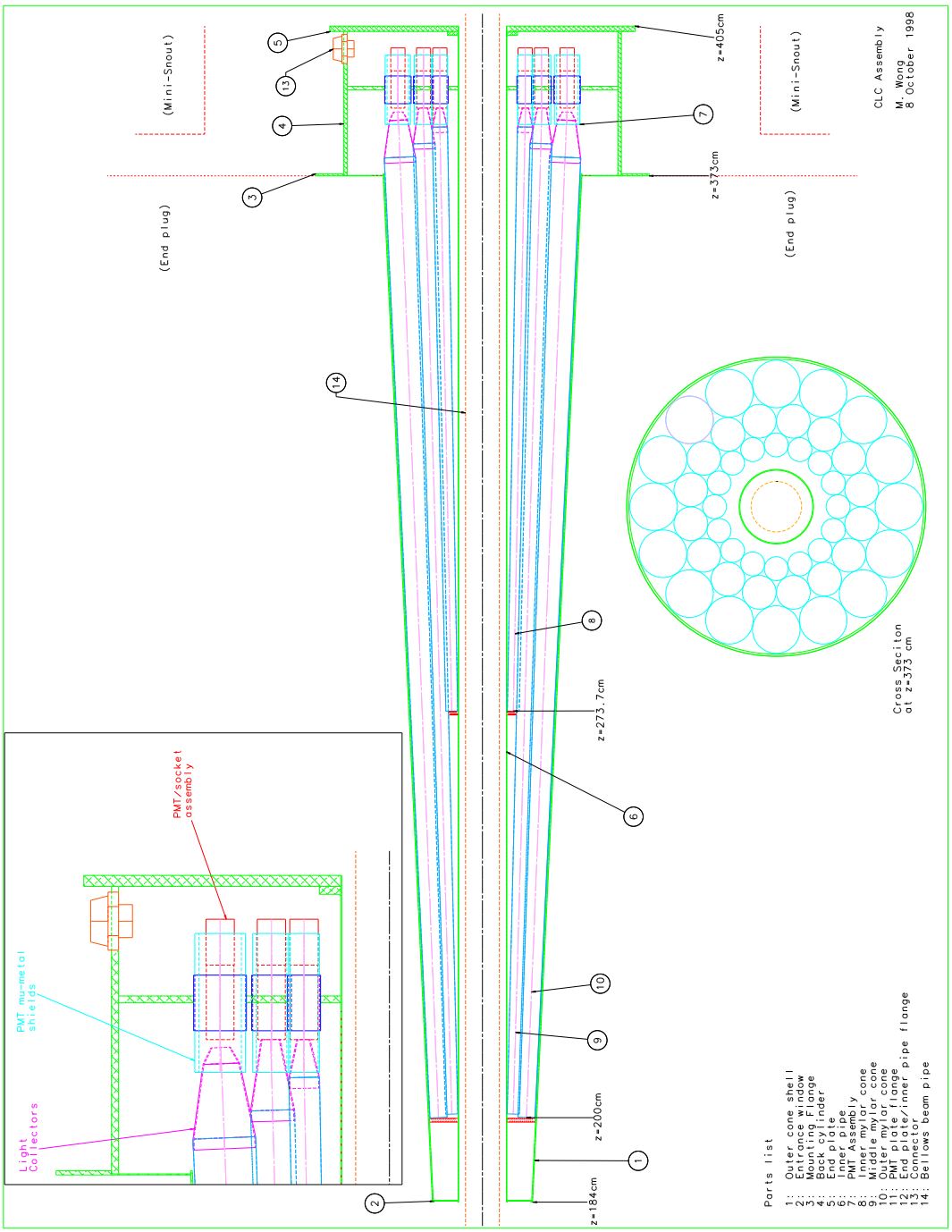

Figure 2.17: *Longitudinal section of the CLC system.*

2.2.6 Trigger and Data AcQuisition (DAQ) system

Since the interaction rate at the Tevatron collider is well beyond the current maximum storage rate, the task of separating the great majority of background events

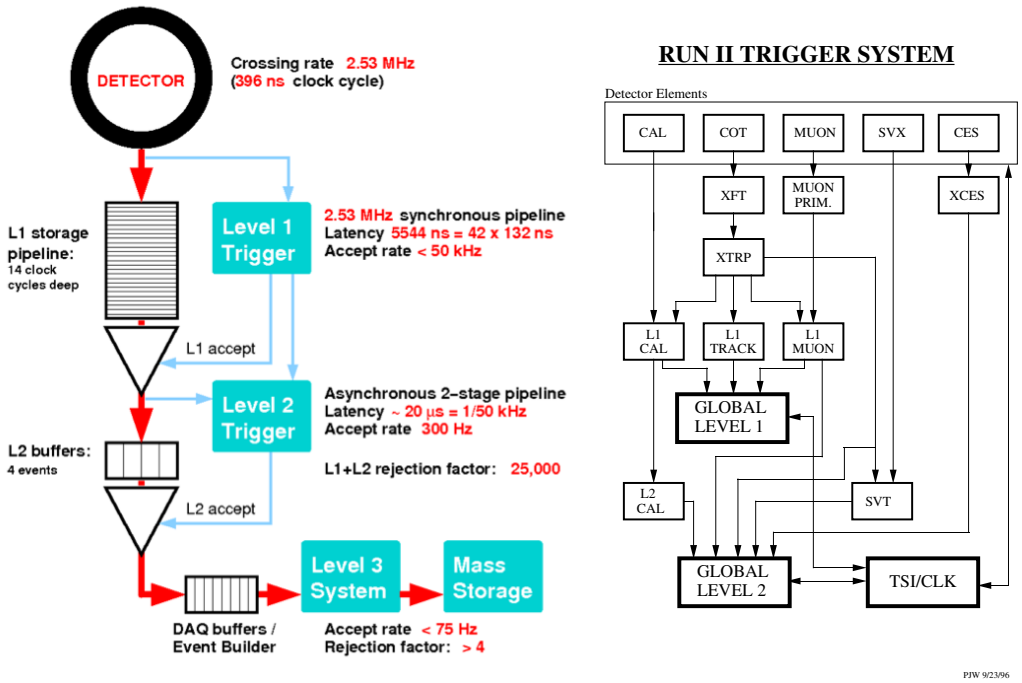

Figure 2.18: *Functional block diagram of the CDF II trigger and data acquisition system.*

from the fraction of interesting events is of crucial importance[15]. This goal is achieved by the trigger system which evaluates the partial information provided by the detector in real time and discards the uninteresting events.

The Tevatron runnnig at 396 ns of interbunch spacing has an average collision rate of about 1.7 MHz; the writing of events on permanent memories is designed for a maximum rate of ~ 100 Hz. For practical reasons the CDF II trigger has been designed as a multi-stage system in order to reduce the acquisition rate allowing to record only the events with a physical interest. Its architecture is modular and divided into three levels, represented in Figure 2.18. Each level receives the data event from the previous one and, provided with more accurate detector information and more time for processing, chooses to discard it or to send it to the following level. Level-1 receives data directly from the detector front end electronics; events passing the Level-3 are stored to permanent memory.

Since the read-out of the entire detector needs about 2 ms on average, after the acquisition of one event, other ~ 5,000 interactions would occur and remain unrecorded. The percentage of events rejected solely because the trigger is busy

[15]E.g., the b production cross section is ~ 1,000 times smaller than the total $p\bar{p}$ inelastic one. High p_T physics as vector bosons or *top* physics suffers even smaller signal-to-background ratios at production.

processing previous events is referred to as trigger *deadtime* and at the current luminosity its tipical value is around the 5%.

2.2.6.1 Level 1 (L1)

A trigger divided into three stages does not remove the problem to deal with the Tevatron crossing rate of ~ 1.7 MHz; the problem is now re-routed to the Level-1 (L1) stage. In order to avoid deadtime caused by the trigger processing time, L1 has to sustain the clock of the Tevatron. In a complex detector as CDF II, it is unconceivable an effective trigger architecture able to process data and make a decision in less than 396 ns. The "impasse" is overcome with a fully pipelined front-end electronics for the whole detector. The signal of each channel is stored, every 396 ns, in a buffer of a 42-cell long pipeline. This means that L1 has 396×42 ns $\simeq$ 16 μs to make its decision before the content of the buffer is deleted. The actual latency of L1 is 5.5 μs, as was designed for a crossing time of 132 ns.

At L1, a synchronous system of custom-designed hardware processes a simplified subset of data in three parallel streams to reconstruct coarse information from the calorimeters (total energy and presence of single towers over threshold), the COT (two-dimensional tracks in the transverse plane) and the muon system (muon stubs in the CMU, CMX, and CMP chambers). A decision stage combines the information from these low-resolution physical objects, called "primitives", into more sophisticated objects (e.g., track primitives are matched with muon stubs or tower primitives) to form muon, electron or jet[16] objects, which are subjected to basic selections.

The eXtremely Fast Tracker (XFT) is a custom processor that identifies two-dimensional tracks in the (r, ϕ) view of the COT (transverse plane) in time with the L1 decision. It uses pattern matching to first identify short segments of tracks and then to link them into full-length tracks. If a coincidence between segments crossing four super-layers is found, two-dimensional XFT-tracks are reconstructed by linking the segments. Segments are compared with a set of about 2,400 predetermined patterns corresponding to all tracks with $p_T \gtrsim 1.5$ GeV/c originating from the beam line. The track-finding efficiency and the fake-rate with respect to the off-line tracks depend on the instantaneous luminosity and were measured to be $\varepsilon \approx 96\%$ and 3%, respectively, for tracks with $p_T \gtrsim 1.5$ GeV/c at $\mathcal{L} \approx 10^{32}$ [cm^{-2}s^{-1}]. The observed momentum resolution is $\sigma_{p_T}/p_T^2 \approx 0.017$ c/GeV and the azimuthal resolution is $\sigma_{\varphi_6} \approx 0.3°$ (where φ_6 is the azimuthal angle of the track measured at the sixth COT super-layer, located at 106 cm radius from the beam line).

Currently about 63 different L1 combinations of requirements are implemented and they have an output rate of ~ 18 KHz.

[16] A particle jet is a flow of observable secondary particles produced in a spatially collimated form, as a consequence of the hadronization of partons produced in the hard collision.

2.2.6.2 Level 2 (L2)

The Level-2 (L2) trigger performs two subsequent operations. The *Event building* produces in output the event as reconstructed with L2 detector information and the *Decision* combines outputs from L1 and L2 to evaluate whether to flag or not the event for Level-3 processing.

The Event building process is done in parallel; calorimetric information is used to perform clustering and identification of hadronic jets. Simultaneously, the Silicon Vertex Trigger (SVT), a dedicated processor, combines XFT track informations with SVX II hits. It measures 2D track parameters with almost offline level quality for tracks with $p_T > 2$ GeV/c. The key improvement of the SVT track with respect to the XFT track is the measurement of the track's impact parameter. The event building has 10 μs to complete its task.

The Decision stages some selection algorithms, customized for each different combinations of requirement, runs on four dedicated CPUs and processes the available information from L1 and L2 in less than 10 μs.

The maximum latency of L2 is 20 μs for each event. The current number of different combinations of requirements at L2 is about 126 and the output rate is ~ 300 Hz.

2.2.6.3 Level 3 (L3)

Level-3 (L3) is implemented exclusively by software. About 400 commercial processors running in parallel reconstruct the event provided by L2 at full detector resolution. L3 codes are very similar to the offline reconstruction codes. About 191 *trigger paths*[17] are actually implemented at L3; moreover L3 distributes the information to on-line monitoring consumers and data logger programs. The L3 decision to write on tape happens after the full reconstruction of the event is completed and the integrity of its data is checked in less than 10 ms. The typical size for an event is 150 kbytes and the maximum storage rate is about 20 Mbyte/s. The event output rate is finally ~ 75 Hz (the 40% tracking, 30% jet and photon and 30% lepton). The trigger deadtime never exceeds 5%.

2.2.7 Operations and data quality

The proper operation of the detector and the quality of the on-line data-taking is continuously ensured by "crews" of three members of the CDF Collaboration plus one technician who alternate on duty with eight-hours shifts, plus several subdetector experts available on request. The on-line crew, in communication with the Tevatron crew, ensures smooth data-acquisition, monitors the crucial parameters of

[17] A trigger path defines a particular sequence of L1, L2 and L3 selections; an event flagged with a particular trigger path satisfied all the 3 levels requests. Different trigger paths differ by at least one level request but the same level request can be used by different trigger paths.

all subdetectors and intervenes in case of malfunctions. The average data-taking efficiency is ~ 85%. The inefficiency is approximately equally shared in a 5% arising at the beginning of the store, when the detector is not powered while waiting for stable beam conditions, a 5% due to trigger deadtime and a 5% due to unexpected detector or DAQ problems.

When no beam is present, cosmic-rays runs are taken or calibrations of the subdetector are done. During the Tevatron shut-down periods, the crew coordinates and helps the work of experts that directly access the detector.

Each time that at least one of the trigger paths fires, an "event" is labeled with a progressive number. Events are grouped into runs, i.e. periods of continuous data-taking in constant configurations of trigger table, set of active subdetectors and so forth[18]. Several parameters of the operations (e.g. beam-line position and slope, set of calibrations, ...) are stored in the database on a run-averaged format.

The data flow from L3 is segmented into ten trigger streams according to their macroscopic trigger features (di-muon trigger, jet trigger, Two-Track Trigger, ...). All data manipulations occurring some time after the data are written to permanent memories are referred to as *off-line* processes, as opposed to the on-line operations which take place in real time, during the data-taking. The most important off-line operation is the processing with a centralized *production* analysis that generates collections of high-level physics objects suitable for analysis such as tracks, vertices, muons, electrons, jets, ... from low-level information such as hits in the tracking subdetectors, muon stubs, fired calorimeter towers, ... During the production, more precise information about the detector conditions (e.g. calibrations, beam-line positions, alignment constants, masks of malfunctioning detector-channels, ...) and more sophisticated algorithms are used than those available at the L3 of the trigger. The production may be repeated when improved detector information or reconstruction algorithms become available: this typically occurs once or twice every year. The reprocessing uses large farms of commercial processors that reconstruct approximately 10^7 events per day employing approximately 2-5 s per event with 1 GHz CPU[19]. The added information increases the event size by typically 20% after production.

To ensure homogeneous data-taking conditions, each run undergoes a quality inspection. On-line shift operators, off-line production operators and subdetector experts certify in what fraction of data the running conditions for all relevant sub-detectors are compliant to physics-quality standards. When detectable problems of the detector occur, the data-taking is quickly stopped, so very short runs are likely to contain corrupted data. Runs with fewer than 10^8 live Tevatron clock-cycles,

[18]The data acquisition might need to be interrupted and recovered for several motivations, including the need for enabling or disabling a subdetector, the need for a change in the trigger table, a problem in the DAQ chain and so forth.

[19]The event size and the processing-time increase roughly linearly with the instantaneous luminosity.

or fewer than 10^4 (10^3) L1 (L2) accepts, or containing data corresponding to an integrated luminosity $\int \mathcal{L}dt < 1/\text{nb}$ are excluded from physics analysis. On-line shift operators further exclude the runs in which temporary or test trigger tables were used[20]. Runs whose data underwent problems or software crashes during the production are excluded off-line.

Accurate integrated luminosity measurements are ensured in physics-quality data by requiring the CLC to be operative during the data-taking and by verifying that a set of luminosity and beam-monitor probe quantities are within the expected ranges. Shift operators ensure that L1, L2 and L3 triggers operate correctly. In addition, higher level quantities such as event yields of $J/\psi \to \mu^+\mu^-$, $D^0 \to K^-\pi^+$, and $D^{*+} \to D^0\pi^+$ decays are monitored on-line and are required to be within the expected ranges. For analyses that use COT information, the minimum run integrated luminosity required is 10/nb and the fraction of noisy COT channels is required to be below 1%.

2.2.8 Monte Carlo simulation of CDF II

An important need, common to many analyses, is the necessity to estimate the fraction of events escaping from the detector acceptance and the detailed study of the detector expected response to the passage of particles. Typically, however, the complex geometry of the detectors and the huge number of effects that one has to take into account to predict this behaiour, make the analytical derivation of the relevant distributions extremely hard or even impossible. To solve this kind of problem are useful (and often used) Monte Carlo (MC) simulation tecniques. In High Energy Physics (HEP) experiments, these tecniques can be used at two different levels: *generator* and *detector*[21]. For generator level, in our case, we incorporate the simulation of all the processes involved in the $p\bar{p}$ collision starting from the partons interactions up to the formation of the final state hadrons; the detector level instead deals with the simulation of the passage of the produced particles inside the detector materials, the signals generated and collected by the subdetectors, their read out, etc. CDF Monte Carlo samples rely on two different type of generators: BGenerator [22] and Pythia [23].

To generate a B-hadron decay sample in the CDF B Monte Carlo (BMC) there are three different steps: the first step is the B-hadron generation, then the hadron is forced to decay into a particular final state and finally the decay products are propagated within the CDF II detector. The hadron generation and the decay are generated using BGenerator algorithm. In this step the algorithm as input information needs the joint distribution of transverse momentum and pseudo-rapidity for the different b-hadrons.

[20] It is sometimes necessary to test new configurations of the trigger selections in a real data-taking condition to monitor trigger rates, performance and so on.

[21] An additional step can be required for some kind of analyses: the *trigger simulation*.

Pythia, instead, simulates the whole temporal evolution of the two hadrons that take part in the process in several steps. At the beginning of the simulation two particles in the beams (a p and a $\bar{p}$) move towards each other; both them are composed of dynamic quarks and gluons: the "partons". Partons are described by their structure functions, called *PDF*s (Parton Density Functions) that represent, e.g., the probability of having a particular quark with a certain momentum. A collision is treated as an impact between two partons and several physical processes are then simulated: production of bosons, initial and final state radiation, multiple parton interactions, etc. Because of the QCD confinement, the products of the collisions are neither independent nor observable: the departing partons are represented by the string model. While moving apart, the color field lines that bound them are confined into a "pipe" that suffers breaks due to the creation of $q\bar{q}$ pairs. Strings fragment producing hadrons (color singlets) that will decay into several final state stable particles. The cross sections of the different process depend of the PDFs; however, PDFs derive only partially from the perturbative theory. For their definition some initial conditions (that theories can't predict) are needed; once fixed it is then possible to describe the PDFs evolution in terms of the Q^2 of the process. The only way to define this condition is through direct measurements with HEP experiments. For this reason PDFs undergo continuous updates and all the improvements obtained give a higher precision in the simulation of this type of interactions.

Once the physics of the interaction and the generated particles are available, they are propagated within a simulation of the detector in order to reproduce their interactions with the materials and the different signals they produce in all the subdetectors. In the standard CDF II simulation the detector geometry and material are modeled using the version 3 of the GEANT package [24] tuned using data from the test-beams and collision data. GEANT receives in input the positions, the four-momenta and the identities of all the particles produced by the simulated collisions that have long enough lifetimes to exit the beam pipe. It simulates their passage through the detector, mimicking their interactions (bremmstrhalung, multiple scattering, nuclear interactions, photon conversions, ...) and the consequent generation of signals on a channel by channel basis. Specific packages replace GEANT for some sub-detectors: the calorimeter response is simulated with GFLASH, a faster parametric shower-simulator [25] tuned from single particle response and shower shape using test beam data (8-230 GeV/c electrons and charged pions) and collision data (0.5-40 GeV/c single isolated tracks); the drift time within the COT is simulated using GARFIELD standard package [26] further tuned on data. The charge deposition model in the silicon uses a parametric model, tuned on data, which accounts for restricted Landau distribution, production of δ rays, capacitive charge sharing between neighboring strips and noise[22], etc.

The output of the simulated data has the same format as the real data, allowing

[22] If needed, the actual trigger logic can be simulated for all digital parts of the trigger.

their analysis with the same reconstruction programs. The detector and trigger configuration underwent several changes during data taking. Minor variations may occur between runs, while larger variations occur, for instance, after major hardware improvements or Tevatron shut-down periods. For a more detailed simulation of the actual experimental conditions, the simulation has been interfaced with the off-line database that reports, on a run-by-run basis, all known changes in configuration (position and slope of the beam line, relative mis-alignments between subdetectors, trigger table used, set of SVT parameters, ...) and local or temporary inefficiencies of the silicon tracker (active coverage, noisy channels, ...). This allows simulating the detailed configuration of any set of real runs, to match the distribution of real data in any given sample.

2.2.9 Event reconstruction and analysis framework

Once selected by CDF trigger or simulated by the Monte Carlo, events are stored on tapes and analyzed with a reconstruction program called *Production*; this process identifies in each event several physical objects that can be used by physicists for their analyses (primary and secondary vertices, jets, muons, ...). Data are then directly accessible by all CDF analysis groups (QCD, B, Electroweak, Higgs, ...); what usually happens is that each group creates a set of ntupes of these data in order to have a secondary (reduced in size) set of data that physicists may use. These ntuples are created within the ROOT framework [27] (written in C++ and commonly used by several HEP experiments) and this same environment is also used for all the analyses preformed at CDF. Occasionally, the ntuples may be reprocessed when an important improvement in the reconstruction is available. In this work we used the so-called Standard Ntuples (Stntuples) that are the default set of data used by the QCD group and the one containing the events collected by the triggers needed for this analysis.

Chapter 3

Data selection

This chapter describes the process to extract the $D^0 \to K^-\pi^+$ (and $\bar{D}^0 \to K^+\pi^-$) decays, referred to as "signal(s)", from all the other events, referred to as "background". After a brief discussion on the physics of the decay, we describe the online trigger selection and the offline cuts optimized to reach the minimal statistical uncertainties on the quantities we want to measure.

3.1 $D^0 \to K\pi$ decays at CDF

The D^0 decay channels to a couple of charged particles represent the simplest topology that we can study at CDF II to detect these "charmed" (neutral) mesons; in particular the $D^0 \to K\pi$ one has a sizeable branching fraction (~ 3.9 %) that gives us a chance to identify this heavy meson lost in a background of light particles (mainly pions and kaons) several orders of magnitude larger. Its relatively large mean lifetime ($\tau \sim 410 \cdot 10^{-15}$ s) results in a travelled path, away from the $p\bar{p}$ collision that originates it, of the order of few hundreds μm ($c\tau \sim 123$ μm) which can be measured thanks to the resolution of the silicon tracker SVX II (see Section 2.2.3.2). Combining together all the possible couples of tracks (with opposite charges) in each event, we can fit their helices looking for an intersection point displaced by the primary vertex; if the fit returns a possible common origin for the two tracks we have a D^0 **candidate**. We can then evaluate the candidate's invariant mass and study its distribution for all the candidates found in the sample looking for the evidence of a signal at the expected D^0 mass (~ 1.864 GeV/c^2).

Figure 3.1 visually decribes the topology of a D^0 that decays into $K^-\pi^+$ and gives us the opportunity to define some relevant quantities discussed in this analysis:

- the **transverse plane** is the plane perpendicular to the proton beam direction (*0xy*);

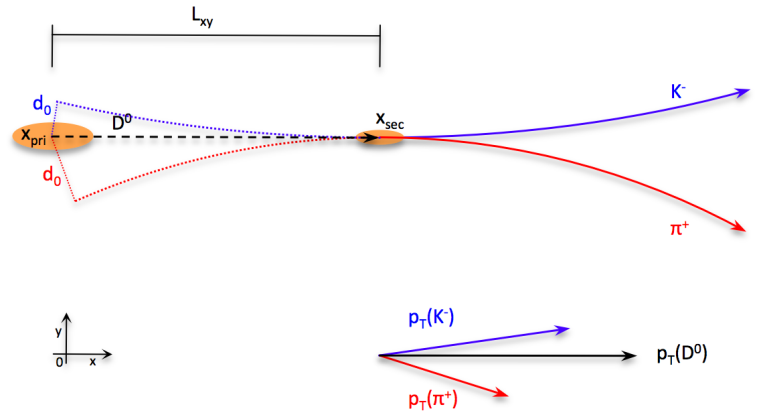

Figure 3.1: *Graphical representation of the topology of the* $D^0 \to K^-\pi^+$ *decay channel in the transverse plane.*

- the **primary vertex** $\vec{x}_{pri}$ is the point (within the beam pipe) where the $p\bar{p}$ collision occurs and it represents the D^0 **origin vertex**;
- the **transverse momentum** $\vec{p}_T$ is the projection of the momentum vector on the transverse plane (p_T represents its magnitude);
- the **secondary vertex** $\vec{x}_{sec}$ is the point where the D^0 decays into the two charged lighter mesons, $K^-\pi^+$;
- the **transverse decay lenght** L_{xy} is the signed distance between the primary and the secondary vertices projected onto the transverse plane of the path travelled by the D^0 before decaying:

$$L_{xy} = \frac{(\vec{x}_{sec} - \vec{x}_{pri}) \cdot \vec{p}_T}{p_T}; \tag{3.1}$$

- the **impact parameter** d_0 is the signed distance of the closest approach between the flight path of a particle (helix for a charged particle and a straight line for neutral ones) and the beam line (the sign is given by the opposite sign of the z component of the angular momentum evaluated w.r.t. the beam position at the maximum approach coordinate);
- the **longitudinal distance** Δz_0 between the two tracks is the difference of the z coordinate at their maximum approach to the beam;
- the **transverse opening angle** $\Delta\varphi_0$ between the two tracks is the difference of their angles in the transverse plane measured at the point of their maximum approach to the beam.

3.2 Online

We use the samples collected by the `ZEROBIAS` and the `MINBIAS` trigger paths; we choose them to avoid the risk of introducing a bias in the variables we have to measure. The previous CDF measurement of the D^0 production cross section [12] starts at a minimum $p_T(D^0)$ of 5.5 GeV/c because the data set is based on a trigger selection with hard requests in terms of transverse momentum of the meson decay products. Our goal, instead, is to reach $p_T(D^0)$ values down to 1.5 GeV/c; this choice requires removal of any possible bias at trigger level on this quantity. The two trigger paths used satisfy this requirement and their details are described in the following subsections. The sample has been collected over 8 years of data taking (from February 2002 to February 2010) and it corresponds to a total Tevatron delivered luminosity $L_{\text{dev}} = 6.7/\text{fb}$.

3.2.1 Zero Bias (ZB) trigger

The `ZEROBIAS` is the first trigger path used to collect events for this work. Its requirements to trigger an event are the followings:

Level 1: any bunch crossing fires L1. Prescale factor = 1,000,003.

Level 2: any event is automatically accepted by L2.

Level 3: no requests.

No CDF II subdetectors are used by this trigger path; its operation is totally related to the Tevatron bunch crossing frequency independently of whether the crossing produced a hard scattering or not. Because of the intrinsic maximum output rate of each CDF II trigger level, the event rate must be reduced by a prescale factor. At L1, then, the trigger is fired once every 1,000,003 bunch crossings resulting in about 1.7 events per second that pass L1. No further selection is applied at L2 and L3. The sample collected by this path contains ~ 177 millions of events.

3.2.2 Minimum Bias (MB) trigger

`MINBIAS` is the second path used; its requirements are the followings:

Level 1: CLC signals coincidence. Prescale factor = 100,003.

Level 2: any event is automatically accepted by L2. Rate limit = 3 Hz.

Level 3: any event is automatically accepted by L3. Rate limit = 1 Hz.

While the ZEROBIAS triggers any bunch crossing whether or not a collision occurs, the aim of this trigger path is to identify (and select) only crossings resulting in, at least, an inelastic $p\bar{p}$ collision. This check is performed at L1 using the Cherenkov luminosity counters (CLC): the trigger, indeed, requires a signal (at least 250 ADC counts) in at least one East CLC in coincidence with a signal in at least one West CLC. Every 100,003 times this coincidence occurs, one event is triggered by L1; again, this prescale factor is used to reduce the trigger rate because at the usual Tevatron initial luminosity almost all the bunch crossings result in a hard collision. L2 and L3 further reduce the trigger rate setting the output L3 rate to one event per second. The sample collected by this path contains ~ 123 millions of events.

3.2.3 Samples overlap

The two trigger selections operate at the same time during the data taking; this implies that events might be collected by both paths and appear twice in the sample. In particular the MINBIAS sample is a subset of the ZEROBIAS one: bunch crossings with no hard interaction won't be triggered by the CLC coincidence while all the crossings that trigger the CLC do also trigger the ZEROBIAS. From these simple considerations we can estimate the rate of overlapping events to be of the order of magnitude of 1 per million because the global effect of the prescale and the rate limit set in the MINBIAS trigger path represent a reduction factor of ~ 10^6. In fact we find that 194 events are present in both samples; in what follows these events are used only once and the effect of the overlap on key variables (e.g. sample's luminosity) is completely negligible w.r.t. their uncertainties.

3.3 Offline

3.3.1 Good Run List

The standard CDF data-quality requirements, described in 2.2.7, are used to define a list of "good" runs, called Good Run List (GRL), that CDF II physicists may use for their analyses; analysis groups make available several lists based on the proper functioning of some of the CDF II subdetectors (e.g. analyses based on the tracking system can use runs where the calorimeters did not work properly but not runs where the COT was excluded). For this work we use the official list that contains only runs where SVX II and the COT were working properly. After the GRL request the ZB sample is reduced to ~ 141 millions while the MB sample to ~ 85 millions.

3.3.2 Luminosity

CDF II instantaneous luminosity measurement is derived from the rate of the inelastic $p\bar{p}$ events estimated with the luminosity monitor (CLC). The CLC, in fact,

measures the average number of primary interactions μ which is related to the instantaneous luminosity $\mathcal{L}$ by the following equation [28]:

$$\mu \cdot f_{BC} = \sigma_{in} \cdot \mathcal{L} \tag{3.2}$$

where f_{BC} is the Tevatron average bunch crossing rate ($\sim$ 1.7 MHz) and σ_{in} the inelastic $p\bar{p}$ cross section at $\sqrt{s}$ = 1.96 TeV. A measurement of σ_{in} at the Tevatron has been performed only at the beginning on Run II when the center of mass energy was 1.8 TeV [29, 30]; after increasing the energy to the current value, the inelastic cross section has not been measured anymore and now the luminosity evaluation relies to an extrapolation of its value at 2 TeV. For historical reasons, even if the value of 2 TeV was never reached, the online and the offline calculation use that extrapolation underestimating $\mathcal{L}$ of about 1.9 %. Table 3.1 summarizes the correction of the measured integrated effective luminosities L_{eff} for our samples to get the right value of L ($L = L_{\text{eff}} \cdot 1.019$) that we have to use for this analysis.

	L_{eff}	$L_{\text{eff}} \cdot 1.019$
ZB	5.61	5.72
MB	4.40	4.48
Tot	10.0	10.2

Table 3.1: *Luminosities correction for ZB, MB and total samples in* $(nb)^{-1}$.

3.3.3 Base selection

The main ingredient to measure the D^0 production cross section is the number of candidates in our sample. Then, the very first step of the analysis is to apply a selection on the offline tracks in order to select only the *good quality* tracks in the events to be used to reconstruct the D^0 candidates. The requests for the single track are the followings:

- SVX II small angle stereo hits $\geq$ 1;
- SVX II stereo hits $\geq$ 2;
- SVX II axial hits $\geq$ 3;
- COT stereo hits $\geq$ 25;
- COT axial hits $\geq$ 25;
- $p_T \geq$ 0.9 GeV/c;
- $|\eta| \leq$ 1.2;

- $0.08 \leq |d_0| \leq 1$ mm;

where η is the track's pseudorapidity.
All possible pairs of good tracks are then required to meet the following criteria:

- $q_1 \cdot q_2 < 0$;
- $d_{0,1} \cdot d_{0,2} < 0$;
- $2^\circ \leq \Delta\varphi_0 = |\varphi_{0,1} - \varphi_{0,2}| \leq 120^\circ$;
- $\Delta z_0 = |z_{0,1} - z_{0,2}| \leq 5$ mm;

with q_1 and q_2 the charges of the tracks.
Then each pair of tracks is fit looking for a possible common origin point displaced by the primary vertex. The fit is based on these inputs:

- four-momentum of the negative track (1): our convention is to set the fourth component in the hypothesis that the negative track represents the kaon;
- four-momentum of the positive track (2): our convention is to set the fourth component in the hypothesis that the positive track represents the pion;
- position of the $p\bar{p}$ collision that generates the candidate (referred to as *primary* or *origin* vertex).

We decided to define the origin vertex as the nearest (along the z axis) reconstructed vertex to the mean of the tracks z_0; given the z coordinate of the primary vertex is then possible to evaluate the beam position in the transverse plane at that coordinate to set the other two components of the origin of the candidate. Given these informations, the fitter looks in the transverse plane for a possible intersection point between the two tracks (if necessary, even slightly modifying their momenta) and if, at that point, the longitudinal distance between the two helices is within a certain threshold. If the tracks are totally incompatible, the reconstruction fails; otherwise, if the fit converges, the fitter returns the candidate's decay vertex, the resulting χ^2 of the fit and the new "rearranged" tracks. If the fit succeeds, a D^0 candidate is selected if:

- $L_{\mathrm{xy}} \geq 180$ μm;
- $|y(D^0)| \leq 1$;
- $\chi^2 \geq 0$;

where $y(D^0)$ is the candidate's rapidity. Figure 3.2 shows the invariant $K^-\pi^+$ mass distribution for ZB, MB events and the summed samples, selected as described above, integrated over $p_T(D^0)$. In principle the two samples can not be summed because of their different trigger efficiencies; we assume here that the two triggers have the same efficiency and Section 6.1 will justify this assumption. Both the distributions show a clear peak at the expected D^0 mass ($m_{D^0} \simeq 1.864$ GeV/c^2). We expect that only a half of the $D^0 \to K\pi$ candidates are contained in the visible signal, while the other half (for which we misassign the masses for the outgoing particles) will have a smoother shape indistinguishable from the background.

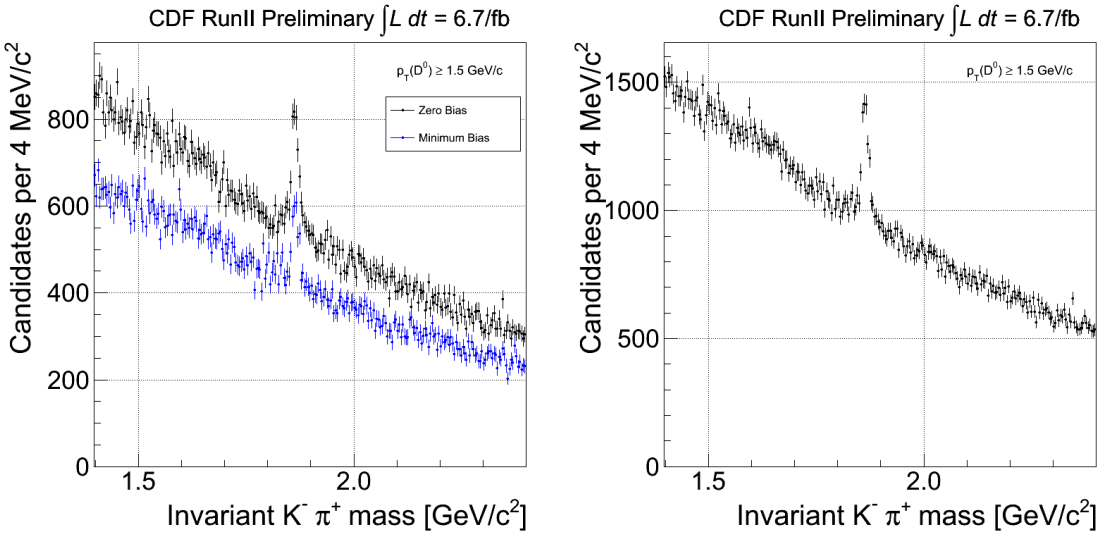

Figure 3.2: *Invariant $K^-\pi^+$ mass distribution of ZB (black), MB (blue) events (left) and summed samples (right) obtained through the selection discussed in the text.*

3.3.4 Selection optimization

The set of cuts described in the previous subsection was arbitrarily choosen referring to previous similar high-p_T analyses and readapting some requests to extend the selection to the low-p_T range; this does not ensure that it is the best one for our needs. We want to improve it with the aim of minimizing the statistical uncertainty associated with the measurement of the number of candidates in our sample. The MC does not help us in this issue because we can't assume that it is able to correctly reproduce all the distributions involved in the selection; we use directly our sample to obtained an unbiased selection of our candidates.

The method uses only data to estimate both signal and background yields for any probed configuration. It is implemented as follows:

- Consider the data sample $\mathcal{S}$ in which an optimization of the selection is required.
- $\mathcal{S}$ is subdivided into two mutually exclusive subsamples, A and B, using a random criterion.
- The same optimization procedure is applied independently on both subsamples:
  1. A criterion is defined to identify the signal events $\mathcal{S}_i^A$ and the background events $\mathcal{B}_i^A$ surviving the i-th configuration of the selection cuts in sample A (e.g., performing a fit of the candidates invariant mass distribution).
  2. The chosen figure of merit, $f(\mathcal{S}_i^A, \mathcal{B}_i^A)$, is maximized over the space of configurations for the selection requirements (e.g., all combinations of cuts).
  3. The configuration of cuts corresponding to the maximum of f defines the set of cuts optimized in sample A.
  4. Steps 3 and 4 are repeated in sample B to obtain the set of cuts optimized in sample B, different in general from the one obtained in sample A.
- The final sample used for the analysis is obtained by applying to the subsample B the cuts optimized in sample A and viceversa.

Figure 3.3 visually describes the procedure.

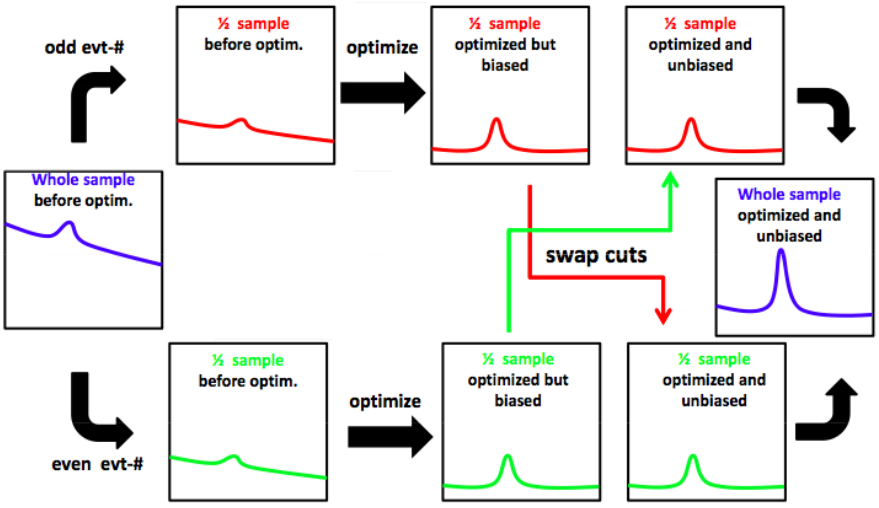

Figure 3.3: *Scheme of the data based selection optimization procedure.*

The procedure is statistically unbiased. A limitation is that this is scarcely effective for small signals (i.e., signals whose size is comparable with statistical

fluctuations of background). In pathologic cases, where the sought signal may sit on a highly constrained region of the phasespace, one should make sure that a fake signal cannot be built up from background clustering in that region of phase space. This is not our case because we decided to apply a global optimization integrating over the whole p_T range we are interested in: the integrated distribution shown in Figure 3.2 clearly shows that we are not in this pathologic case.
To apply this optimization method in our analysis we define the following criteria:

- The two statistically independent subsamples of approximately same size are obtained using the event number, splitting the sample between even and odd events.
- Signal and background are obtained through an extended unbinned likelihood fit of the invariant $K^-\pi^+$ mass plot (the details of this fit will be explained later in Section 5.2).
- The figure of merit is choosen as the one that maximizes the significance of the signal and it's defined as follows:

$$f(\mathcal{S},\mathcal{B}) = \frac{\mathcal{S}}{\sqrt{\mathcal{S}+\mathcal{B}}} \tag{3.3}$$

- Two sets of cuts are obtained based on the event number, an "even" optimal configuration and an "odd" optimal one. They are swapped, applying the *even* optimal configuration to the *odd* subsample and the *odd* optimal configuration to the *even* sample.

For each subsample the optimization algorithm evaluates the figure of merit for each configuration of cuts on the discriminating variables. The topology of our channel is rather simple, thus we have a limited number of simple observables effective in discriminating the signal; we chose to optimize the selection using the following ones: the longitudinal distance Δz_0 between the two tracks, the minimum track's d_0, the candidate's L_{xy} and the fit χ^2. Since the last three variables rely to a plane orthogonal to the z axis, we assume that they are not correlated to the first one; we then perform separately a one dimensional optimization for the Δz_0 and a 3D study for the other variables. For simplicity, in what follows we consider only sample A but the same procedure is used for sample B.

To optimize the Δz_0 we fixed the other 3 cuts this way (as in the base selection described before):

- $|d_0| \geq 80$ μm;
- $L_{\mathrm{xy}} \geq 180$ μm;

- $\chi^2 \geq 0$.

We then probed the function $f(\mathcal{S}, \mathcal{B})$ for 50 different Δz_0 cuts, from 100 μm to 5.1 mm in steps of 100 μm:

$$\Delta z_0 \leq 100 \cdot i \ \mu m, \quad i \in [1; 51]. \tag{3.4}$$

Figure 3.4 shows the value of $f(\mathcal{S}, \mathcal{B})$ as a function of the 50 different Δz_0 limits for sample A. Because the function has a horizontal asymptote we've set the maximum

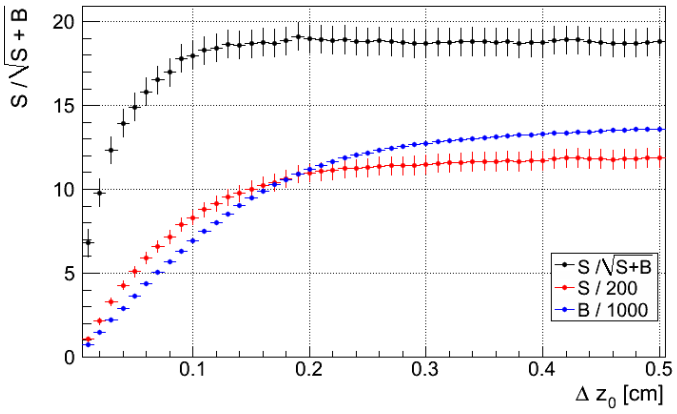

Figure 3.4: $f(\mathcal{S}, \mathcal{B})$ *as a function of the 50 different* Δz_0 *limits for sample A.*

acceptable Δz_0 between the two tracks at 2 mm (when also the signal almost reaches its maximum).

In the 3D optimization for d_0, L_{xy} and χ^2 we fixed the request on Δz_0 to the previous value found ($\Delta z_0 \leq 2$ mm) for all the possible combinations. We probed the function $f(\mathcal{S}, \mathcal{B})$ for 12 different d_0 cuts (from 60 μm to 170 μm in steps of 10 μm), 12 different L_{xy} cuts (from 160 μm to 380 μm in steps of 20 μm) and 12 different χ^2 cuts (from 1 to 12 in steps of 1):

$$\begin{cases} |d_0| \geq 60 + 10 \cdot i \ \mu m, & i \in [0; 11] \\ L_{xy} \geq 160 + 20 \cdot j \ \mu m, & j \in [0; 11] \\ \chi^2 \leq k, & k \in [1; 12] \end{cases} \tag{3.5}$$

Figure 3.5 shows the value of $f(\mathcal{S}, \mathcal{B})$ as a function of the d_0 and the L_{xy} limits for the χ^2 cut where $f(\mathcal{S}, \mathcal{B})$ reaches its absolute maximum for sample A. This maximum is reached when:

- $|d_0| \geq 80$ μm;
- $L_{\text{xy}} \geq 280$ μm;

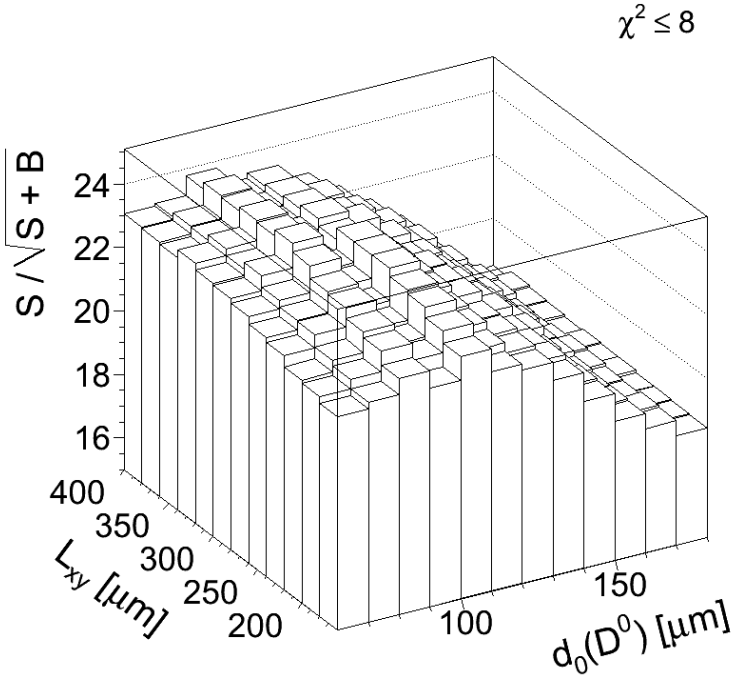

Figure 3.5: $f(\mathcal{S}, \mathcal{B})$ *as a function of the* d_0 *and the* L_{xy} *limits when* $\chi^2 \leq 8$ *for sample* A.

- $\chi^2 \leq 8$.

The same result is obtained when the optimization is performed on sample B; the new "global" selection is completely different from the one used as starting point; Figure 3.6 shows the invariant $K^-\pi^+$ mass distribution for ZB, MB events and the summed samples, selected with the optimized set of cuts, integrated over $p_T(D^0)$. Figures from 3.7 to 3.10 show the same distributions but for several 1 GeV/c invervals of the $p_T(D^0)$ starting from 1.5 GeV/c.

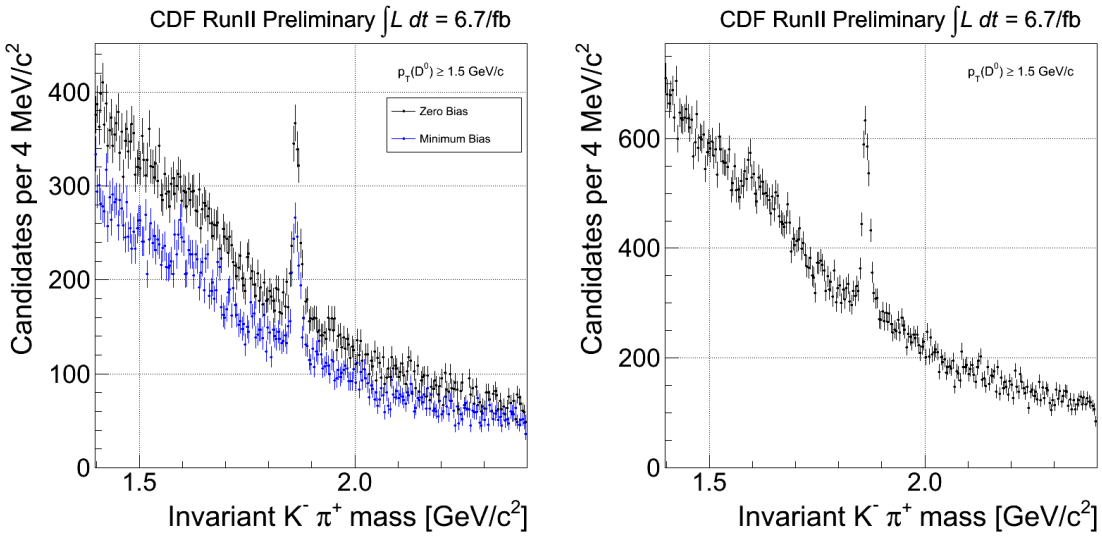

Figure 3.6: *Invariant $K^-\pi^+$ mass distribution of ZB (black), MB (blue) events (left) and summed samples (right) obtained through the optimization.*

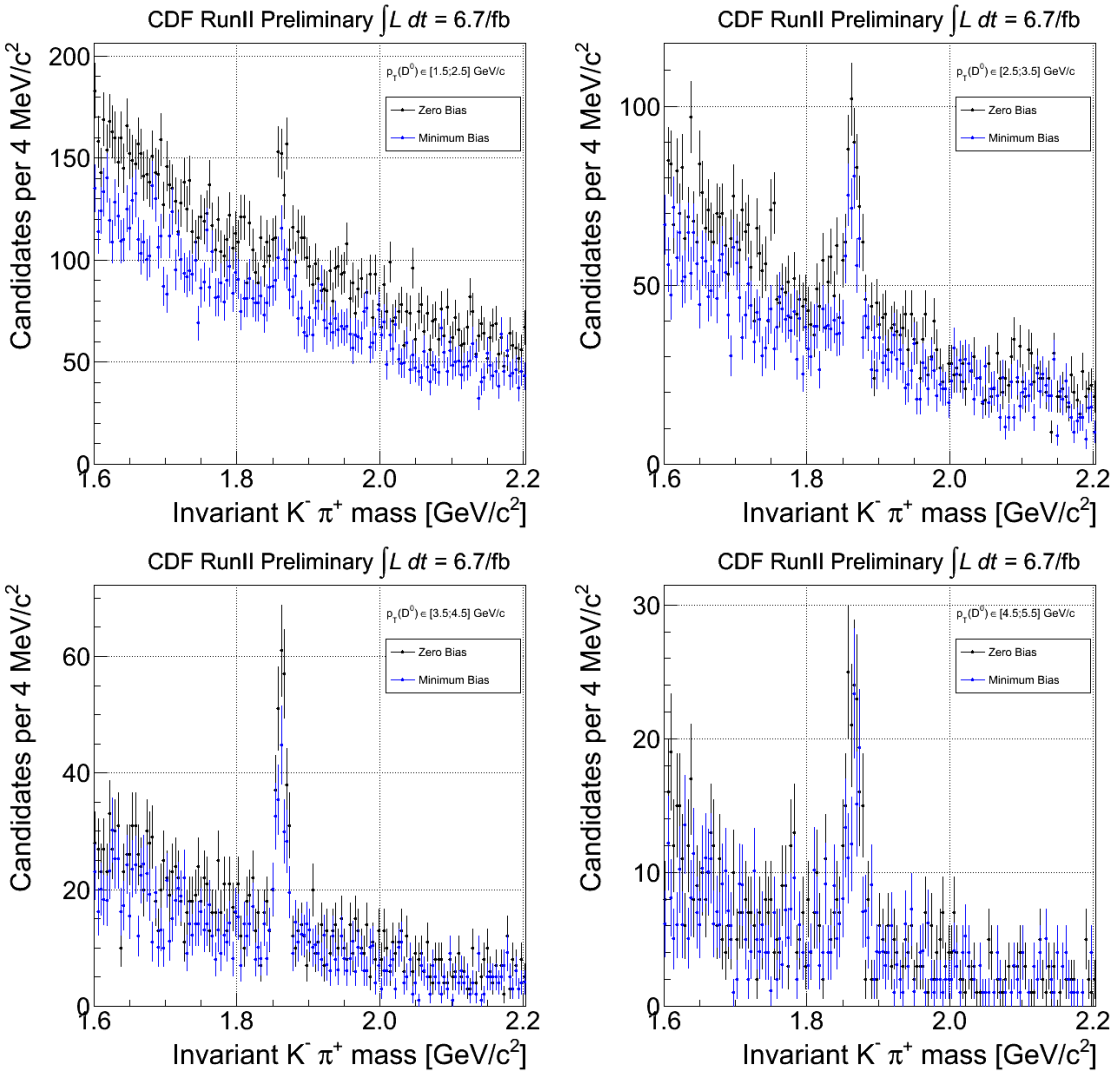

Figure 3.7: *Invariant $K^-\pi^+$ mass distribution of ZB (black) and MB (blue) events obtained through the optimization in 1 GeV/c intervals of $p_T(D^0)$.*

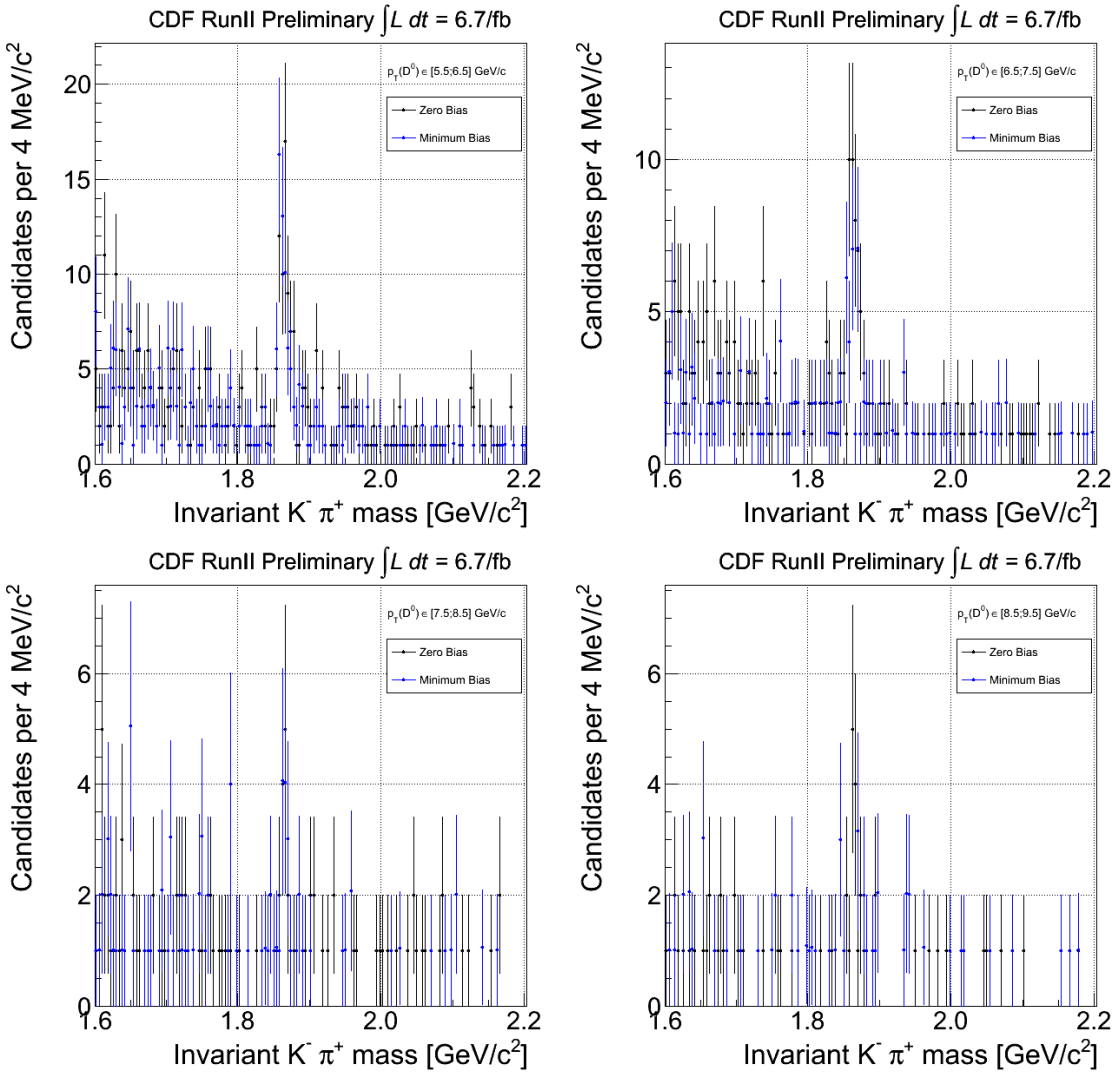

Figure 3.8: *Invariant $K^-\pi^+$ mass distribution of ZB (black) and MB (blue) events obtained through the optimization in 1 GeV/c intervals of $p_T(D^0)$.*

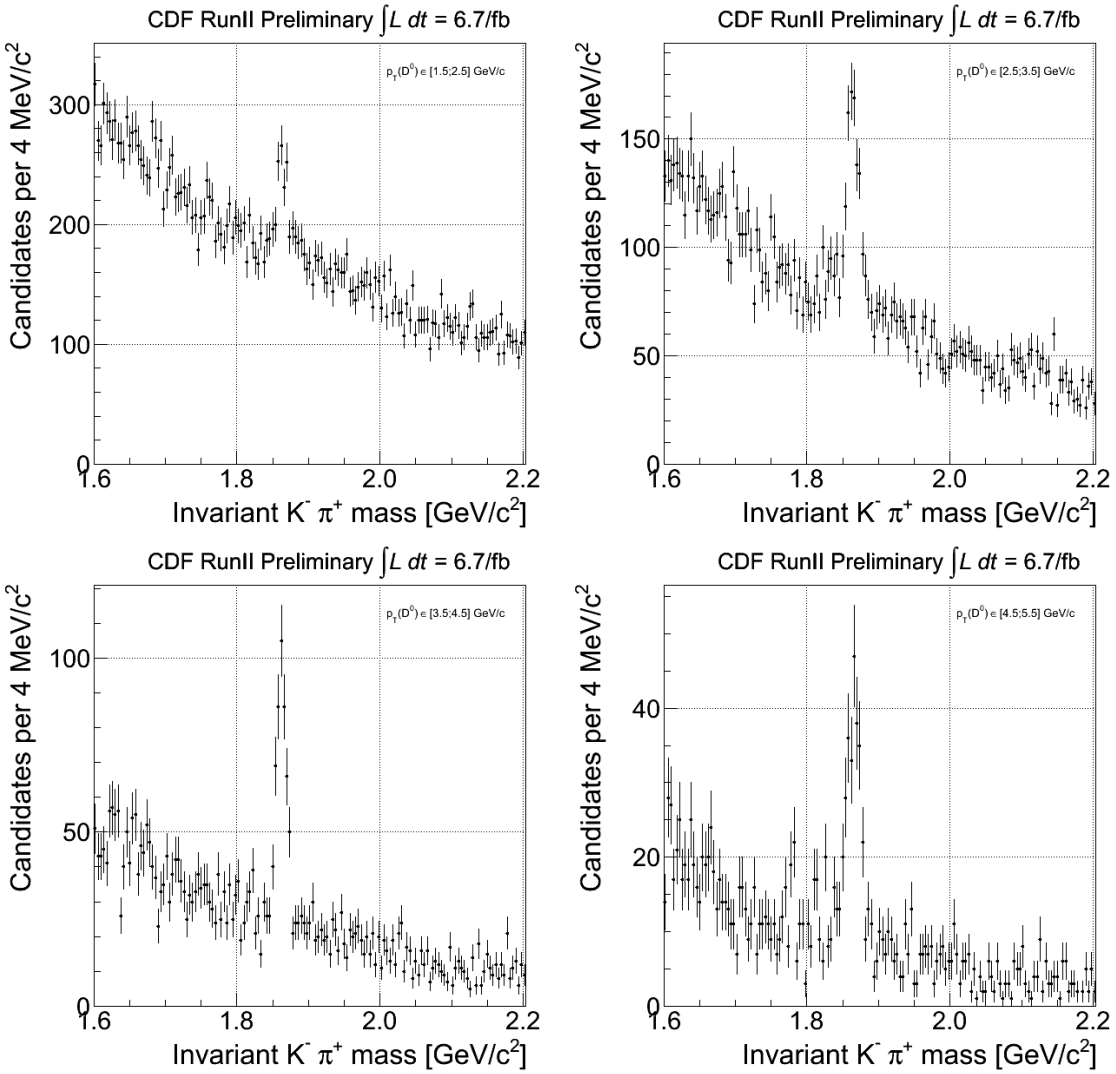

Figure 3.9: *Invariant $K^-\pi^+$ mass distribution for the summed samples obtained through the optimization in 1 GeV/c intervals of $p_T(D^0)$.*

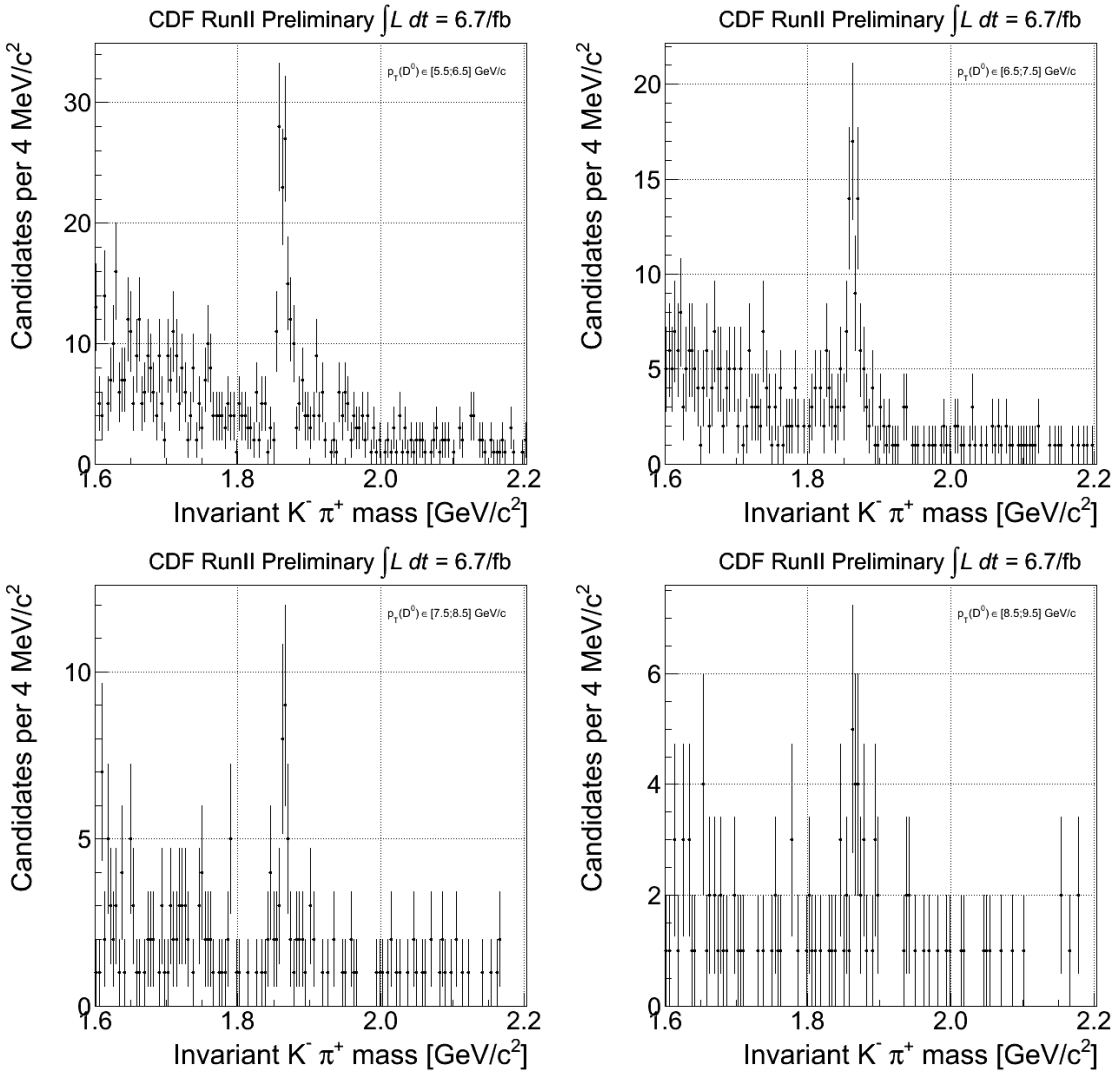

Figure 3.10: *Invariant $K^-\pi^+$ mass distribution for the summed samples obtained through the optimization in 1 GeV/c intervals of $p_T(D^0)$.*

Chapter 4

Monte Carlo samples

This chapter briefly describes the MC samples we generated; we used them to understand how to interpret the distridution obtained from data and to get a model for the shapes of several quantities that will be useful in the rest of our analysis.

4.1 BMC

Some MC samples have been generated in order to cover different needs in this analysis; this section describes their features and what they have been used for in this work. All the following samples were generated using `BGENERATOR` (see Section 2.2.8); they require an input y–p_T distribution for the generated mesons: we used input distributions that span the y–p_T plane in [-1.3; 1.3]×[0; 15] GeV/c. Because we want to reproduce the same online selection, no trigger simulation and selection is performed.

4.1.1 $D^0 \to K\pi$

We generated a sample of D^0 and $\bar{D}^0$ forcing them to decay into Kπ ($D^0 \to K^-\pi^+$ and $\bar{D}^0 \to K^+\pi^-$) to understand how our signal should appear in the invariant $K^-\pi^+$ plot. A realistic shape in the y–p_T range is used in generation. Figure 4.1 shows the resulting invariant $K^-\pi^+$ mass distribution performing the same candidate selection described in Section 3.3.4 on the reconstructed events after the detector simulation. The plot shows a narrow peak centered at the expected D^0 mass ($m_{D^0} \simeq 1.864$ GeV/c^2) with a width of about 8 MeV/c^2 and a wide peak centered at the same mass but with a width which is one order of magnitude larger. The first peak represents the $D^0 \to K^-\pi^+$ signal that we obtain when we have a Right Sign (RS) assignment of the masses to the tracks passed to the vertex fitter: if the negative track is related to the K^- we correctly assign the charged kaon mass ($m_{K^-} \simeq 494$ MeV/c^2) to it and the if positive track is related to the π^+ we assign the charged

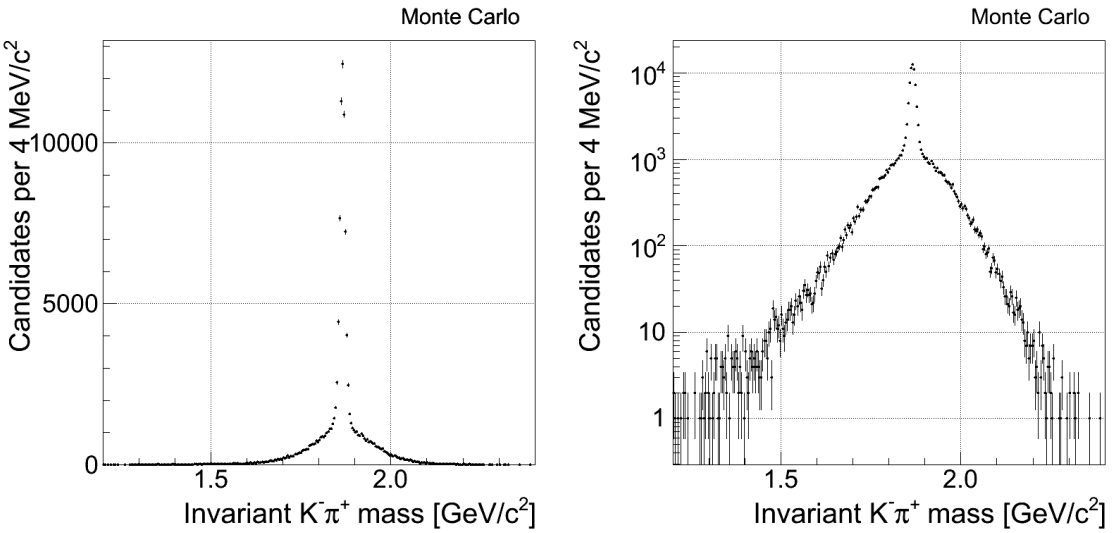

Figure 4.1: *Invariant $K^-\pi^+$ mass of candidates reconstructed in the $D^0 \to K\pi$ MC sample: linear (left) and logarithmic scale (right).*

pion mass ($m_{\pi^+} \simeq 139$ MeV/c^2) to it. If a $\bar{D}^0$ is generated it decays to $K^+\pi^-$; in this case, assigning the kaon mass to the negative track and the pion mass to the positive one, we have a Wrong Sign (WS) assignment. The result of this wrong assumption is the wider signal in the plot. Figure 4.2 shows the same candidates of Figure 4.1 but in a 2D invariant mass plot where on the y axis we assign the masses in the $K^+\pi^-$ hypothesis and on the x axis in the $K^-\pi^+$ hypothesis; here we can clearly separate the two signals: the horizontal bulk of candidates represents the reconstructed $\bar{D}^0$ while the vertical one comes from the generated D^0. Figure 4.1 is simply the projection of this 2D plot on the x axis.
This sample is used in this analysis for several aspects:

- understand how the signals (D^0 and $\bar{D}^0$) appear in the invariant $K^-\pi^+$ mass plots;
- study the signals shapes as a function of p_T and use them to perform the fit of the yield described in Chapter 5;
- study the reconstruction efficiency of our selection as described in Chapter 6;
- evaluate some systematic uncertainties as described in Chapter 7.

4.1.2 $D^0 \to X$

We also generated a sample of D^0 and $\bar{D}^0$ reproducing all the possible D^0 decay channels. A realistic shape in the y–p_T range is used in generation. Figure 4.3 shows

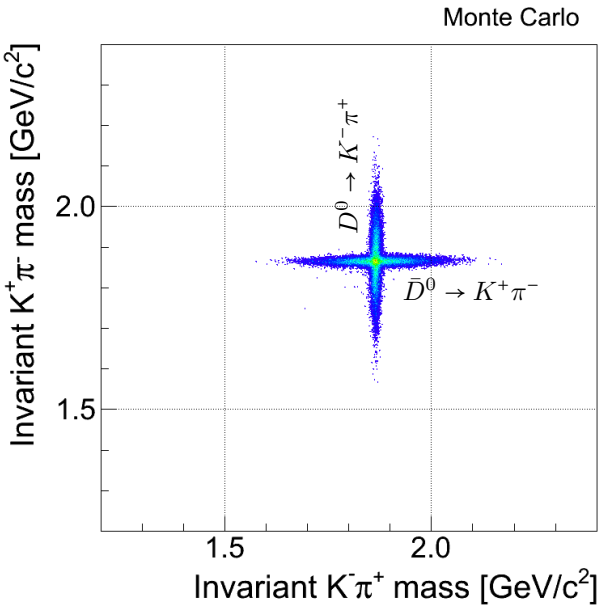

Figure 4.2: *2D invariant mass plot of candidates reconstructed in the $D^0 \to K\pi$ MC sample: $K^+\pi^-$ assignment in the y axis vs $K^-\pi^+$ assignment in the x axis.*

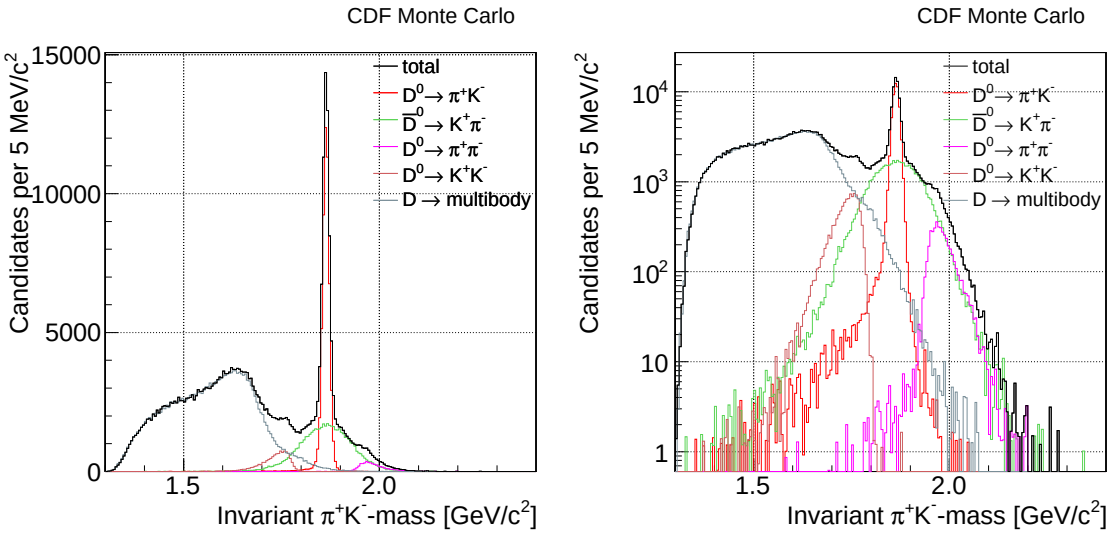

Figure 4.3: *Invariant $K^-\pi^+$ mass of candidates reconstructed in the $D^0 \to X$ MC sample.*

the resulting invariant $K^-\pi^+$ mass distribution performing the same candidates selection described in Section 3.3.4 on the reconstructed events after the detector simulation. The plot shows the same components described in the previous section but with several "new structures" at different invariant masses. Using again the 2D

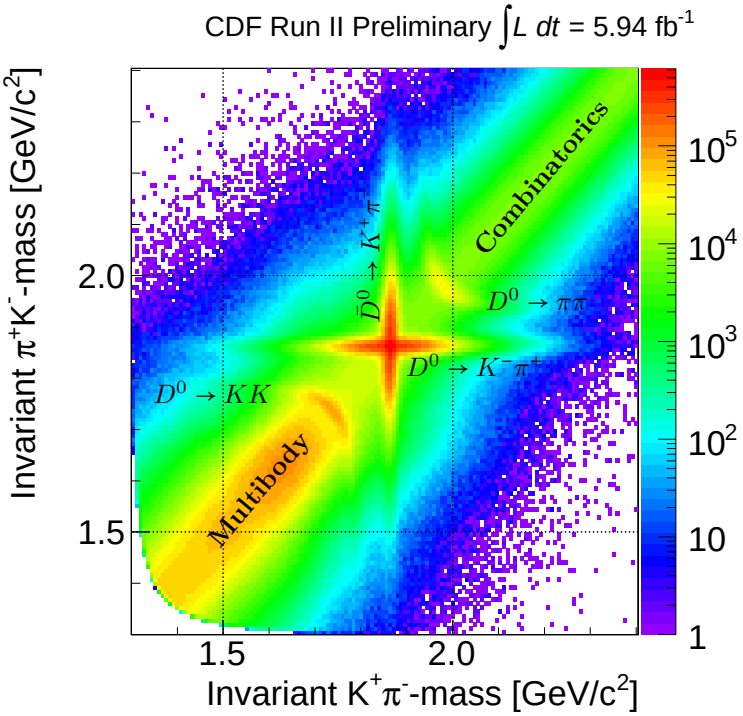

Figure 4.4: *2D invariant mass plot of candidates reconstructed in the $D^0 \to X$ MC sample: $K^+\pi^-$ assignment in the y axis vs $K^-\pi^+$ assignment in the x axis.*

invariant mass plot in Figure 4.4 we can understand the origin of these structures[1]:

- $D^0 \to K\pi$ candidates bulks are still present with the same consideration discussed before;
- $D^0 \to \pi\pi$ decays: in this case we make a mistake in the masses assignment when we fit the candidate assuming that one of the two tracks has the mass of a kaon (we overestimate the candidate's mass);
- $D^0 \to KK$ decays: in this case we make again a mistake in the masses assignment when we fit the candidate assuming that one of the two tracks has the mass of a pion (we underestimate the candidate's mass);

[1]Figure 4.4 shows real data collected by high-p_T triggers; we are showing these data instead of our MC sample because they give a better view of the distribution thanks to the huge statistics and the presence of the combinatorial component (the BMC simulates exclusively the D^0 decays and not the whole event).

- multibody D^0 decays: in this case we use to evaluate the candidate's mass only two tracks (e.g. we miss neutral particles and additional tracks that are decay products of the D^0) underestimating also in this case the real mass of the candidate;

- combinatorial: it includes all the random combinations of tracks in the events that accidentally satisfy our selection.

This sample is useful for several reasons:

- understand how the different D^0 decay channels enter in the invariant mass plot;

- understand the mass intervals where these channels appear in the plot: thanks to this sample we can define the range we can use to perform the fits described in Chapter 5.

4.2 Pythia MC

Other MC samples have been generated using Pythia generator (see Section 2.2.8); unlike the previous samples, generated with `BGENERATOR`, Pythia simulates a whole event starting from the $p\bar{p}$ interaction. The initial state is defined thanks to hard-coded PDFs of the partons inside the colliding barions and the final state reproduces a tipical CDF event through the simulation of many processes as discussed in Section 2.2.8. Because the BMC samples only simulate the signal, several detector's behaviours can't be reproduced and taken into account; the most important one is the drift chamber's occupancy due to the event's multiplicity. Only simulating the complexity of a real event we can correctly evaluate the response of the detector.

4.2.1 Pythia QCD

We generated a generic Pythia sample with no requests on the presence or not of a D^0 in the events.
This sample is used in this analysis for the following aspects:

- study the geometrical acceptance of the CDF II detector to the particles generated in a tipical event;

- study the kinematical acceptance of the CDF II detector to the particles generated in a tipical event;

- study the track's reconstruction efficiency of the charged particles inside the CDF II detector;

- evaluate some systematic uncertainties as described in Chapter 7.

These aspects are crucial to determine the correction we have to apply to our measurement because of the candidates reconstruction efficiency discussed in Section 6.2.

4.2.2 D^0 filtered Pythia QCD

We generated another generic Pythia sample filtering only events where at least a D^0 is generated.
Similarly to the previous one, this sample is used in this analysis for the following aspects:

- study the geometrical acceptance of the CDF II detector to the particles generated in a tipical event;
- study the kinematical acceptance of the CDF II detector to the particles generated in a tipical event;
- study the candidates reconstruction efficiency;
- evaluate some systematic uncertainties as described in Chapter 7.

Thanks to this filtering procedure we can study our signal immersed in realistic events excluding from the sample the huge fraction of cases when only light mesons are generated by the $p\bar{p}$ interaction.

Chapter 5

D^0 signal identification

The main ingredient in the differential cross section evaluation is the raw yield of D^0 in the sample as a function of p_T. This chapter describes the tecnique we use to parameterize signals and background shapes to fit the signals yields from the invariant $K^-\pi^+$ mass distribution.

5.1 Shapes

Thanks to the statistics given by our sample, we have enough data to probe the $p_T(D^0)$ range from 1.5 to 9.5 GeV/c in steps (from now referred to as *bins*) of 1 GeV/c. To extract the raw yield of candidates for each bin we have to model the shapes of the three main components that enter in the invariant $K^-\pi^+$ mass distribution as a function of this variable: D^0, $\bar{D}^0$ and combinatorial background.

5.1.1 D^0

To study the signal shape as a function of $p_T(D^0)$ in the Right Sign (RS) case, we used the $D^0 \to K\pi$ MC sample described in Section 4.1.1. The mass line shape of the RS decay is parameterized through the following pdf:

$$\begin{aligned}\wp_{\rm rs}(m;\vec{\theta}_{\rm rs}) = f\cdot\big(g\cdot\mathscr{G}(m;m_{D^0}+\delta_1,\sigma_1)+(1-g)\cdot\mathscr{G}(m;m_{D^0}+\delta_2,\sigma_2)\big)+\\ +\ (1-f)\cdot\mathscr{T}(m;b,c,m_{D^0}+\delta_1)\end{aligned} \tag{5.1}$$

where:

$$\mathscr{G}(m;\mu,\sigma) = \frac{1}{\sigma\sqrt{2\pi}}e^{-\frac{(m-\mu)^2}{2\sigma^2}} \tag{5.2}$$

$$\mathscr{T}(m;b,c,\mu) = \frac{1}{K}e^{b(m-\mu)}\cdot\mathrm{Erfc}(c(m-\mu)) \tag{5.3}$$

$$K = \int_{m_{\min}}^{m_{\max}} e^{b(m-\mu)} \cdot \mathrm{Erfc}(c(m-\mu))dm \tag{5.4}$$

$$\mathrm{Erfc}(x) = 1 - \mathrm{Erf}(x) = \frac{2}{\sqrt{\pi}} \int_{x}^{+\infty} e^{-t^2} dt \tag{5.5}$$

The pdf is a sum of two Gaussians plus a long tail at lower masses to take into account the soft photon emission; f is the relative fraction of the double Gaussian contribution w.r.t. the total, g is the relative fraction of the Gaussian labeled with the index *1* w.r.t. the sum of the two Gaussians, $\sigma_{1(2)}$ is the width of the Gaussian *1* (*2*) and $\delta_{1(2)}$ is a mass shift from the input mass value m_{D^0} (1.86484 GeV/c^2) due to the asymmetry induced by the soft photon emission. The vector of parameters is defined as $\vec{\theta}_{\mathrm{rs}} = \{f, g, \sigma_1, \sigma_2, \delta_1, \delta_2, b, c\}$ and it's extracted by fitting the simulated invariant $K^-\pi^+$ mass distribution when a D^0 is generated; Figures 5.1 and 5.2 show the result of the parameterization for the RS signal for each bin of $p_T(D^0)$. Figure 5.3 shows again the first two $p_T(D^0)$ bins but in logarithmic scale on the y axis to highlight the presence of the radiative tail; eventual small discrepancies in the tails are well below the precision we need. The shapes obtained show that the RS signal width is almost costant throughout the $p_T(D^0)$ range probed.

5.1.2 $\bar{D}^0$

We, again, obtain the mass line shape as a function of $p_T(D^0)$ in the Wrong Sign (WS) case using the $D^0 \to K\pi$ MC sample described in Section 4.1.1; the mass line shape of the WS decay is parameterized through the same pdf used in the RS case but the vector of parameters $\vec{\theta}_{\mathrm{ws}}$ is now extracted by fitting the simulated invariant $K^-\pi^+$ mass distribution when a $\bar{D}^0$ is generated:

$$\begin{aligned}\wp_{\mathrm{ws}}(m;\vec{\theta}_{\mathrm{ws}}) = f \cdot (g \cdot \mathscr{G}(m; m_{D^0} + \delta_1, \sigma_1) + (1-g) \cdot \mathscr{G}(m; m_{D^0} + \delta_2, \sigma_2)) + \\ + \ (1-f) \cdot \mathscr{T}(m; b, c, m_{D^0} + \delta_1)\end{aligned} \tag{5.6}$$

Figures 5.4 and 5.5 show the result of the parameterization for the WS signal for each bin of $p_T(D^0)$. Figure 5.6 shows again the first two $p_T(D^0)$ bins but in logarithmic scale on the y axis to highlight the presence of the radiative tail; eventual small discrepancies in the tails are well below the precision we need. Unlike the RS signal, the WS fits show an evident dependence on the $p_T(D^0)$: the width of the distribution increases when the momentum grows.

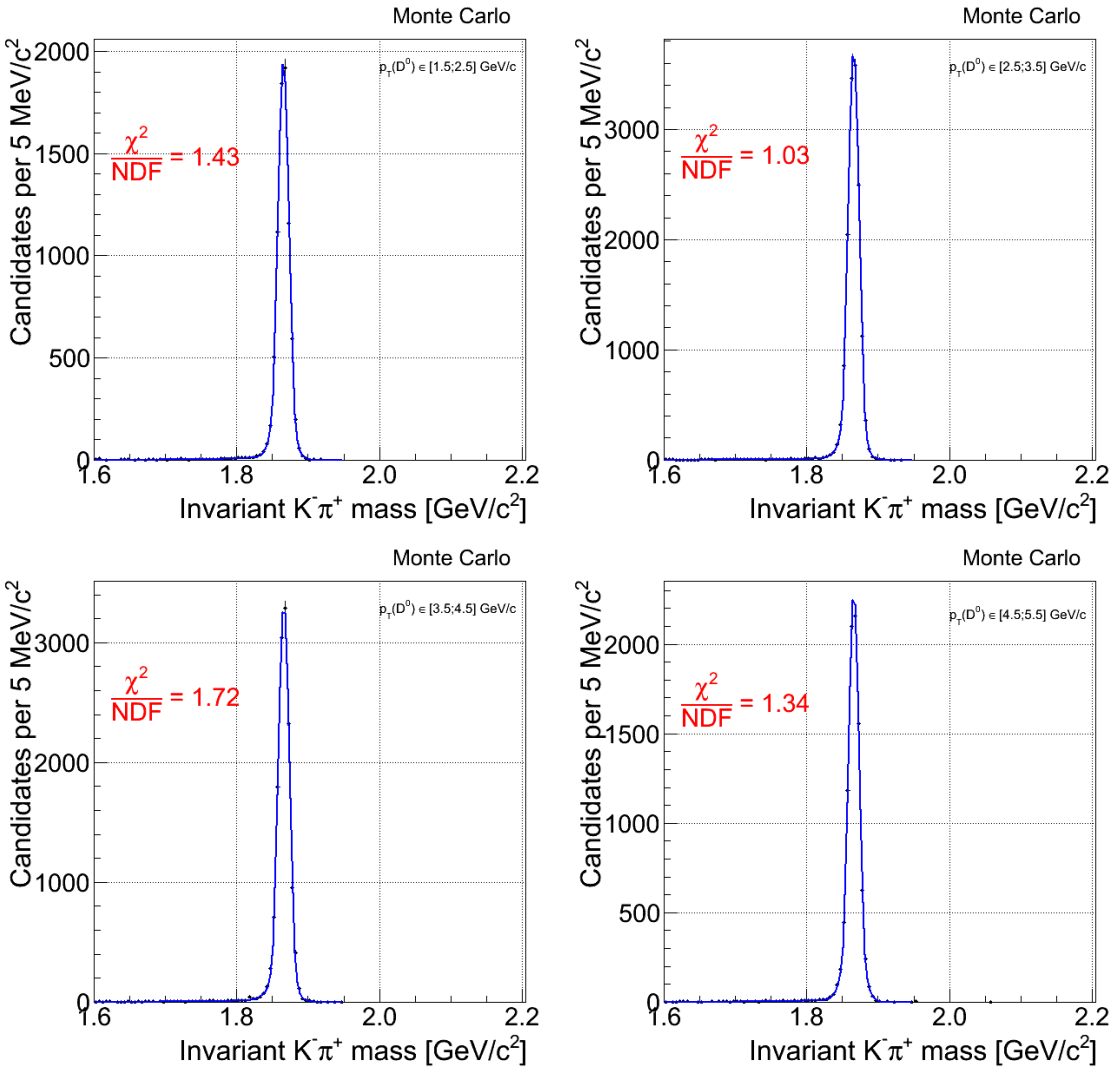

Figure 5.1: *Invariant $K^-\pi^+$ mass distribution of MC events for the RS reconstructions in 1 GeV/c intervals of $p_T(D^0)$.*

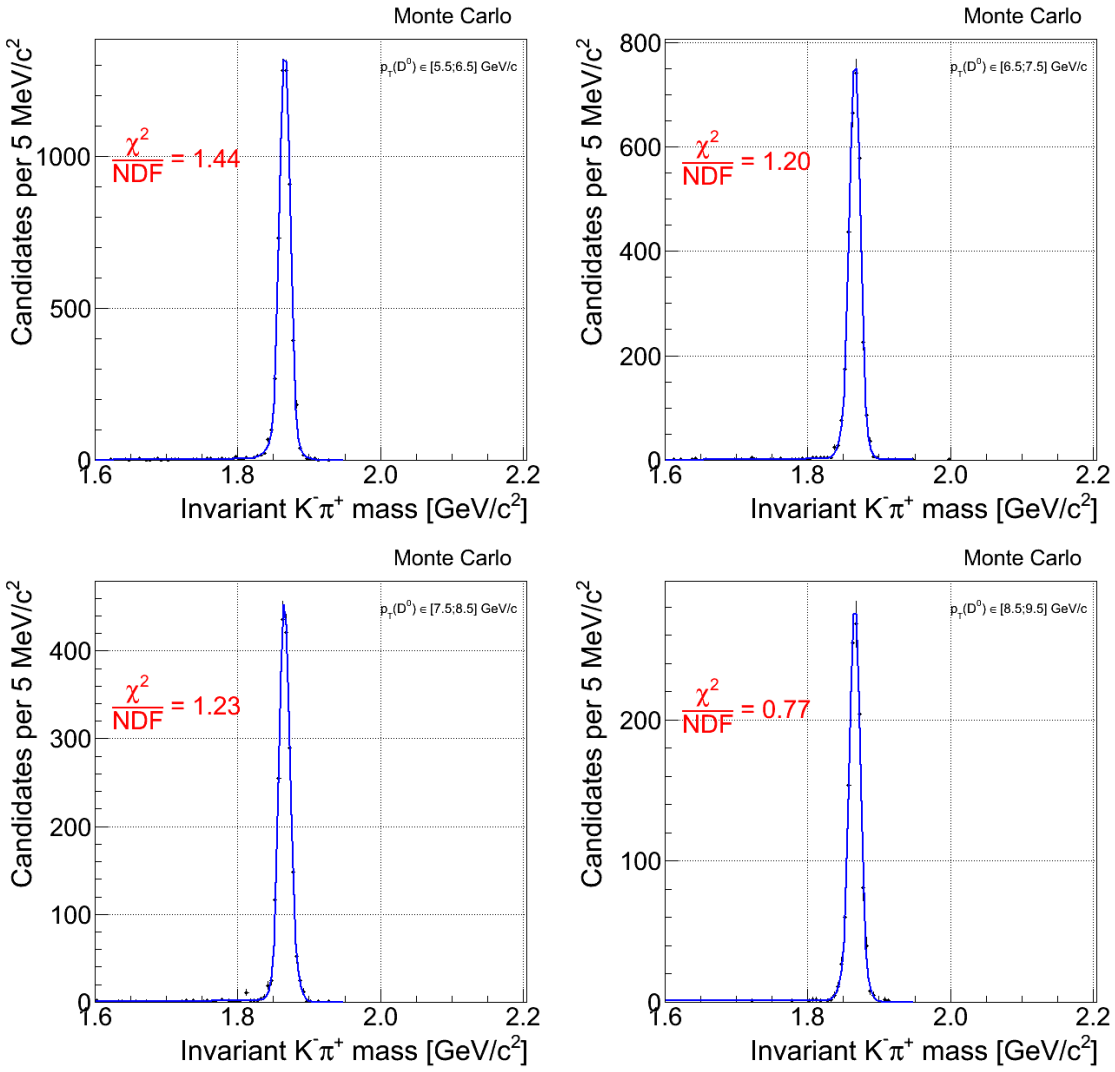

Figure 5.2: *Invariant $K^-\pi^+$ mass distribution of MC events for the RS reconstructions in 1 GeV/c intervals of $p_T(D^0)$.*

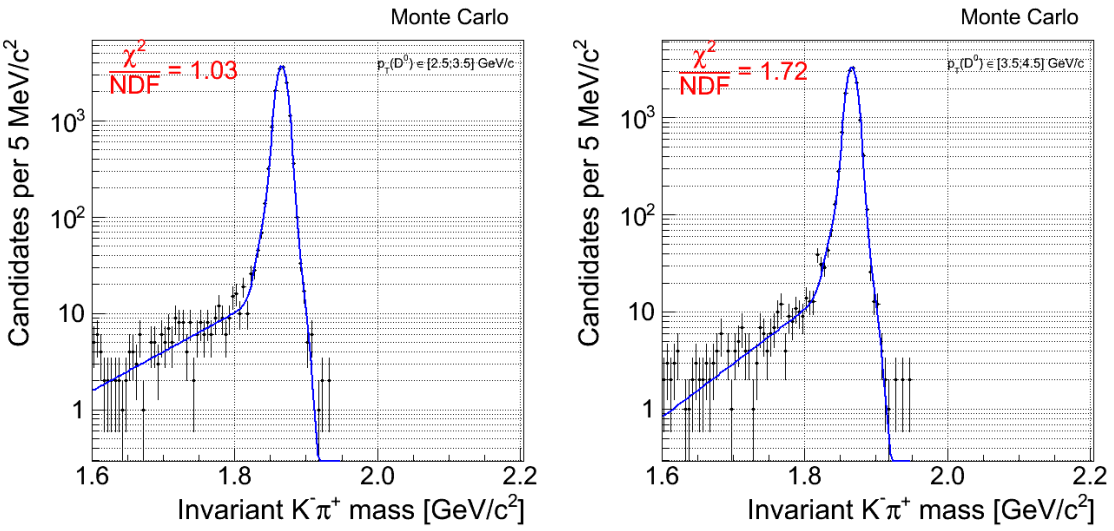

Figure 5.3: *Invariant $K^-\pi^+$ mass distribution of MC events for the RS reconstructions for candidates in the first two $p_T(D^0)$ bins; the y axis is in logarithmic scale to highligth the presence of the radiative tail.*

5.1.3 Combinatorial background

The last shape we have to parameterize is the one related to the candidates due to couples of unrelated tracks that accidentally satisfy our selection's requirements. Unfortunally in our case we can't rely on the sidebands of the candidates invariant mass plot on data (e.g. Figure 3.6) because from the MC simulation of the WS we know that the signal is not negligible for a large invariant mass range around the expected D^0 mass value (e.g. see Figure 5.4). The MC too doesn't help because only the signal is simulated instead of the whole event. We decided to extract the shape of the combinatorial forcing the reconstruction of fake candidates directly on data simply inverting the request on the product of the charges in the couples selection; this way the selection and the secondary vertex fitting procedures are exactly the same as for "true" candidates but, using tracks with the Same Sign (SS), we are sure that they do not come from real $D^0 \to K\pi$. A decreasing exponential shape is a good approximation for the combinatorics trend as shown in Figure 5.7.

5.2 Likelihood fit

For each $p_T(D^0)$ bin, we perform an extended unbinned maximum likelihood fit of the invariant $K^-\pi^+$ mass (m) on data to evaluate the yields of the signals. In our case the likelihood $\mathscr{L}$, defined in Equation 5.7, is a function of three unknown parameters (n_s, n_b, q): the signal (n_s) and background (n_b) yields and the slope (q)

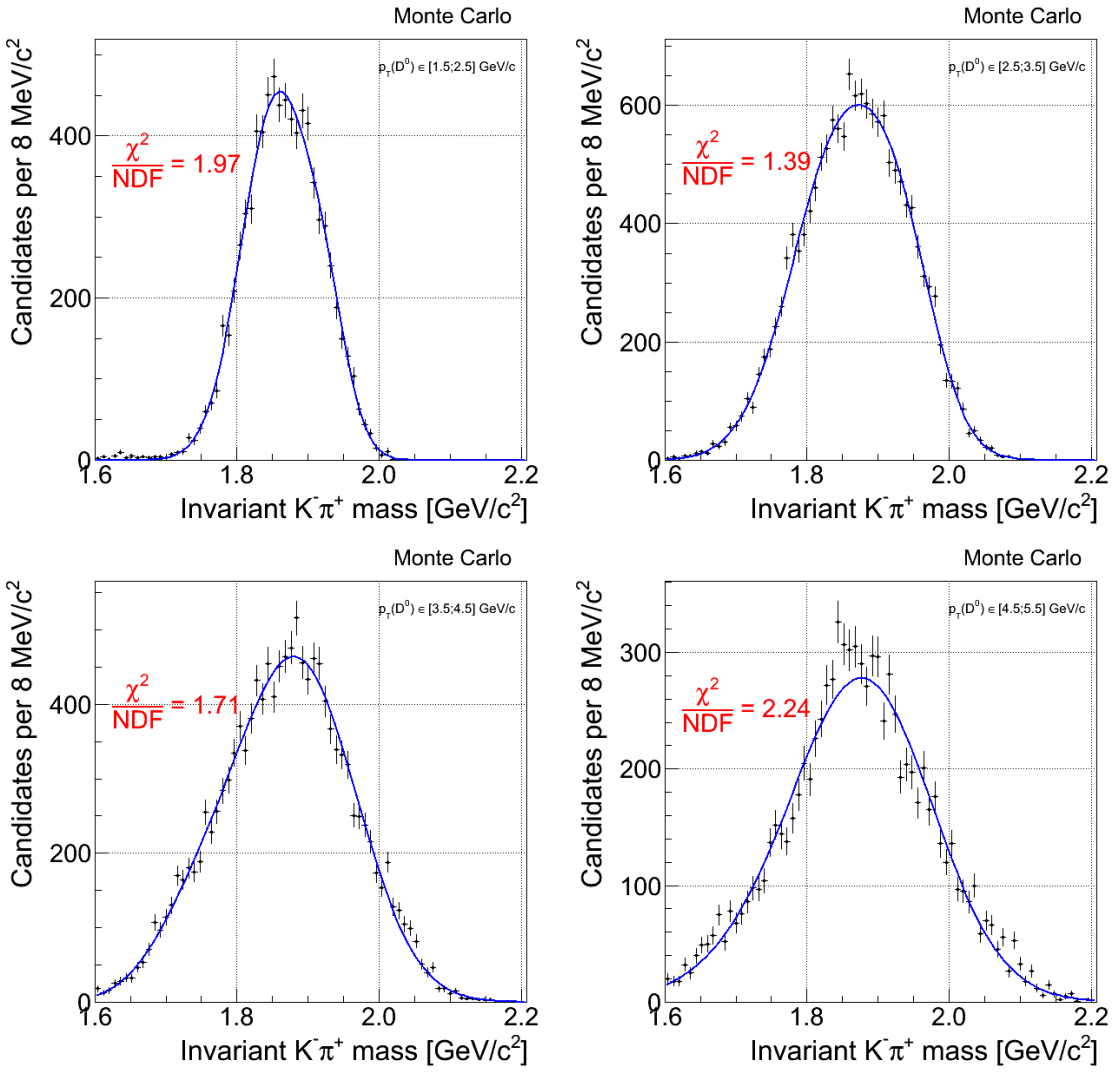

Figure 5.4: *Invariant $K^-\pi^+$ mass distribution of MC events for the WS reconstructions in 1 GeV/c intervals of $p_T(D^0)$.*

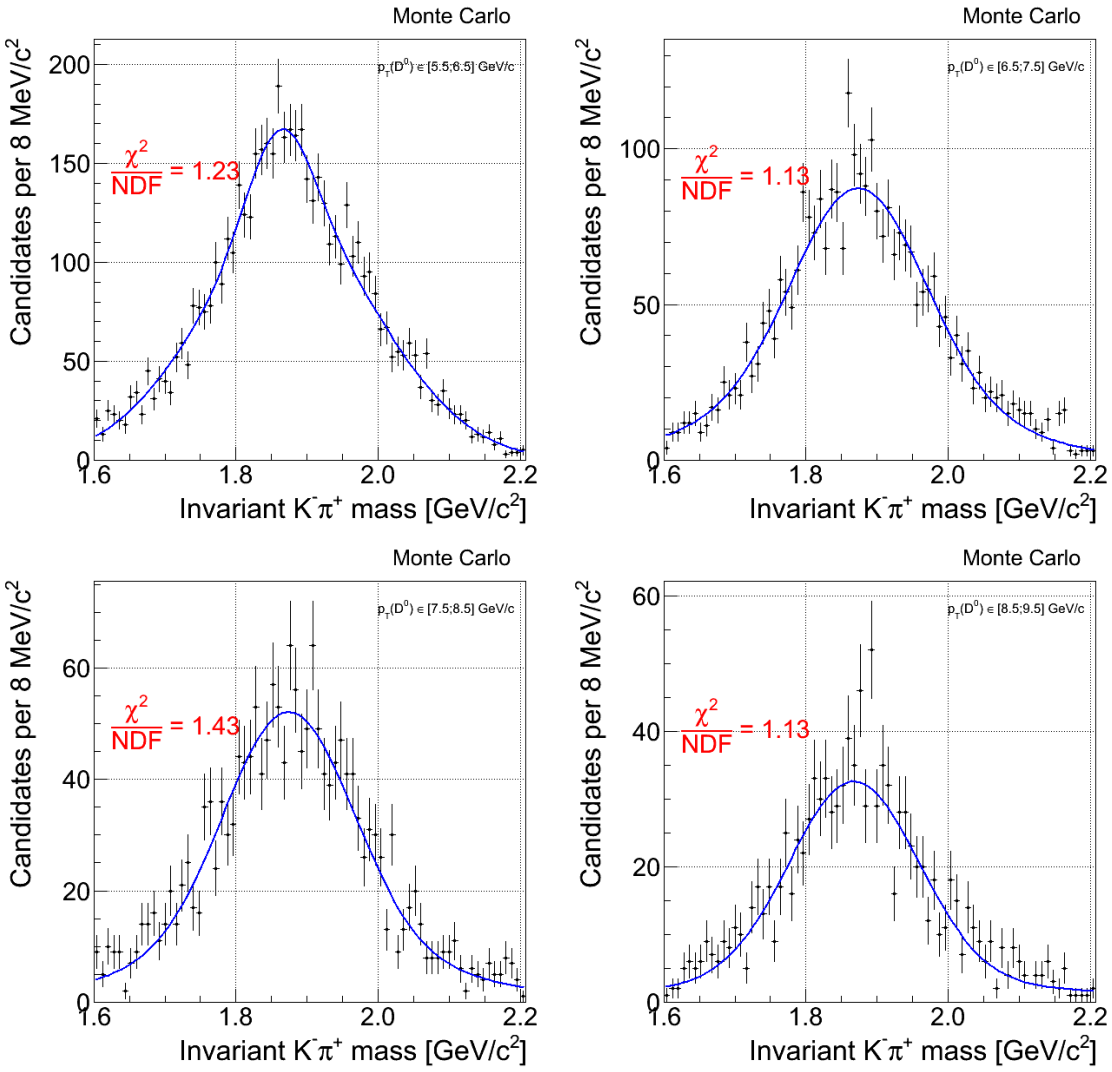

Figure 5.5: *Invariant $K^-\pi^+$ mass distribution of MC events for the WS reconstructions in 1 GeV/c intervals of $p_T(D^0)$.*

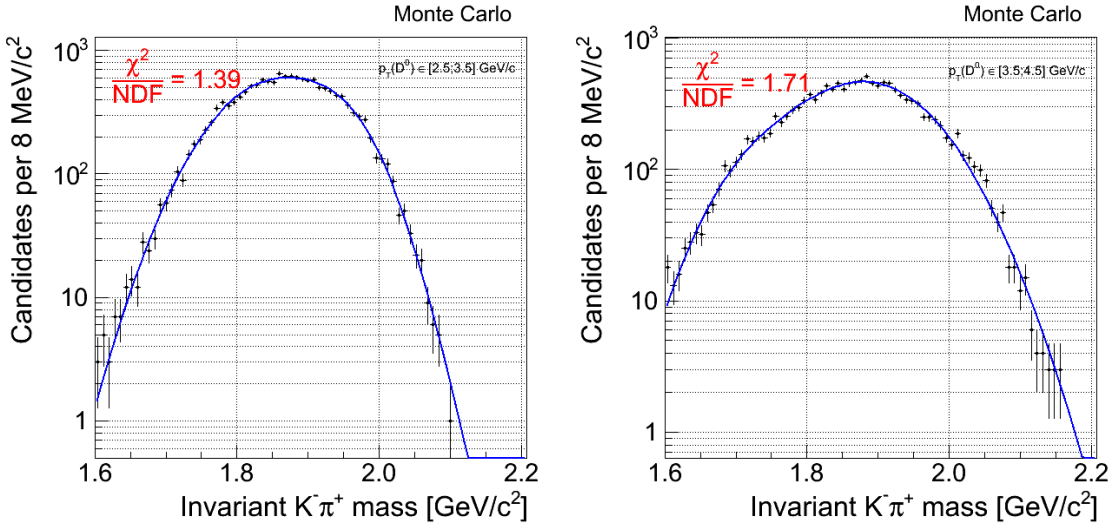

Figure 5.6: *Invariant $K^-\pi^+$ mass distribution of MC events for the WS reconstructions for candidates in the first two $p_T(D^0)$ bins; the y axis is in logarithmic scale to highligth the presence of the radiative tail.*

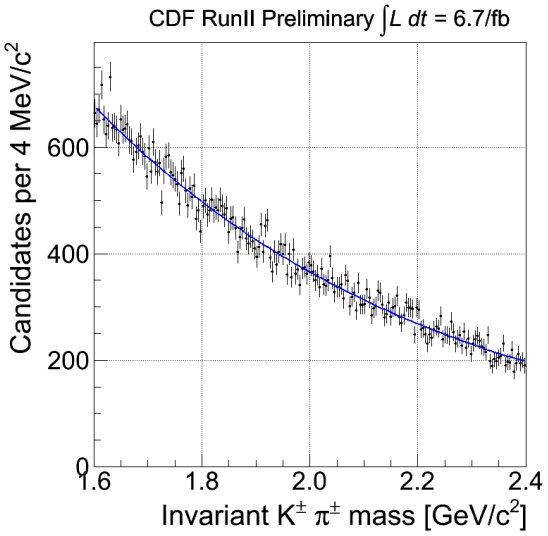

Figure 5.7: *Invariant $K^\pm\pi^\pm$ mass distribution of data events for Same Sign candidates integrated over the whole $p_T(D^0)$ range used in the analysis.*

of the exponential used for the combinatorics.

$$\begin{aligned}\mathscr{L}(m;n_s,n_b,q) &= \frac{e^{-(n_s+n_b)}(n_s+n_b)^{n'_s+n_b}}{(n'_s+n_b)!}\prod_{i=1}^{n'_s+n_b}\left(\frac{n_s}{n_s+n_b}\cdot\wp_{\rm sig}(m_i)+\frac{n_b}{n_s+n_b}\cdot\wp_{\rm bkg}(m_i;q)\right)\\ &= \frac{e^{-(n_s+n_b)}}{(n_s+n_b)!}\prod_{i=1}^{n'_s+n_b}\left(n_s\cdot\wp_{\rm sig}(m_i)+n_b\cdot\wp_{\rm bkg}(m_i;q)\right) \qquad (5.7)\end{aligned}$$

The product is over the $n'_s + n_b$ candidates in the fit range. $\wp_{\rm sig}(m)$ and $\wp_{\rm bkg}(m)$ are the Probability Density Functions (*pdf*s) respectively of the signals and the background defined as follows:

$$\wp_{\rm sig}(m_i) = \frac{f_{\rm rs}}{K_{\rm rs}}\cdot\wp_{\rm rs}(m_i)+\frac{(1-f_{\rm rs})}{K_{\rm ws}}\cdot\wp_{\rm ws}(m_i) \qquad (5.8)$$

$$\wp_{\rm bkg}(m_i;q) = \frac{e^{-q\cdot m_i}}{\int_{m_{\rm min}}^{m_{\rm max}} e^{-q\cdot m_i}dm} \qquad (5.9)$$

where $K_{\rm rs}$ and $K_{\rm ws}$ are the two normalization constants for the signals pdfs that take into account that we fit the invariant mass in the range $[m_{\rm min};\, m_{\rm max}] = [1.79;\, 2.2]$ GeV/c^2 while RS and WS candidates are present also out of this range:

$$K_{\rm rs} = \int_{m_{\rm min}}^{m_{\rm max}} \wp_{\rm rs}(m)dm \qquad (5.10)$$

$$K_{\rm ws} = \int_{m_{\rm min}}^{m_{\rm max}} \wp_{\rm ws}(m)dm \qquad (5.11)$$

Their values for each bin are summarized in Table 5.2.

p_T [GeV/c]	$K_{\rm rs}$	$K_{\rm ws}$
1.5 – 2.5	0.9700	0.9240
2.5 – 3.5	0.9815	0.8415
3.5 – 4.5	0.9848	0.7869
4.5 – 5.5	0.9833	0.7754
5.5 – 6.5	0.9749	0.7775
6.5 – 7.5	0.9618	0.7584
7.5 – 8.5	0.9336	0.7732
8.5 – 9.5	0.9277	0.7566

Table 5.1: *Signals normalization constants K_{rs} and K_{ws} as a function of $p_T(D^0)$.*

$\wp_{\rm rs}(m)$ and $\wp_{\rm ws}(m)$ were defined and described in Section 5.1. The fit is performed minimizing the following quantity in the assumption that our signal is due to the same fractions of RS and WS candidates ($f_{\rm rs} = 0.5$)[1]:

$$-2 \cdot ln(\mathscr{L}) \simeq -2 \cdot (-n_s - n_b + \sum_{i=1}^{n'_s+n_b} ln(n_s \cdot \wp_{\rm sig}(m_i) + n_b \cdot \wp_{\rm bkg}(m_i; q))) \qquad (5.12)$$

5.3 Yields

The fit of the raw yields is performed under three assumptions:

- the RS and WS shapes are taken and fixed for each $p_T(D^0)$ bin from the MC simulation as described in Sections 5.1.1 and 5.1.2: we need a p_T dependent parameterization because the WS distribution width is highly dependent on the D^0 momentum;
- the combinatorial background is assumed to be modeled by a decreasing exponential as described in Section 5.1.3: this assumption has been confirmed using SS candidates reconstructed directly with data;
- the number of RS candidates is constrained to be equal to the number of WS ones ($f_{\rm rs} = 0.5$): in fact, we do not exploit any kind of particle identification information on the final states particles but we can assume C–invariance of the strong interaction production;
- we have to renormalize the RS and the WS pdfs in the range we use for the fit: the fit starts at $m_{\rm min}$ = 1.79 GeV/c^2 (in order to reduce the contamination from the $D^0 \to K^-K^+$ decay channel and the tail of the misreconstructed 3-bodies decays under the signal) and ends at $m_{\rm max}$ = 2.2 GeV/c^2.

Figures from 5.8 and 5.9 show the results of the fits of data bin by bin and Table 5.2 summarizes the results already corrected by the normalization factors $K_{\rm rs}$ and $K_{\rm ws}$. The resulting yields are then visually shown in Figure 5.10.

[1] On the right side of Equation 5.12 we removed the term $ln((n_s + n_b)!)$ that comes from the denominator of Equation 5.7 because it simply changes the magnitude of the minimum but not its position.

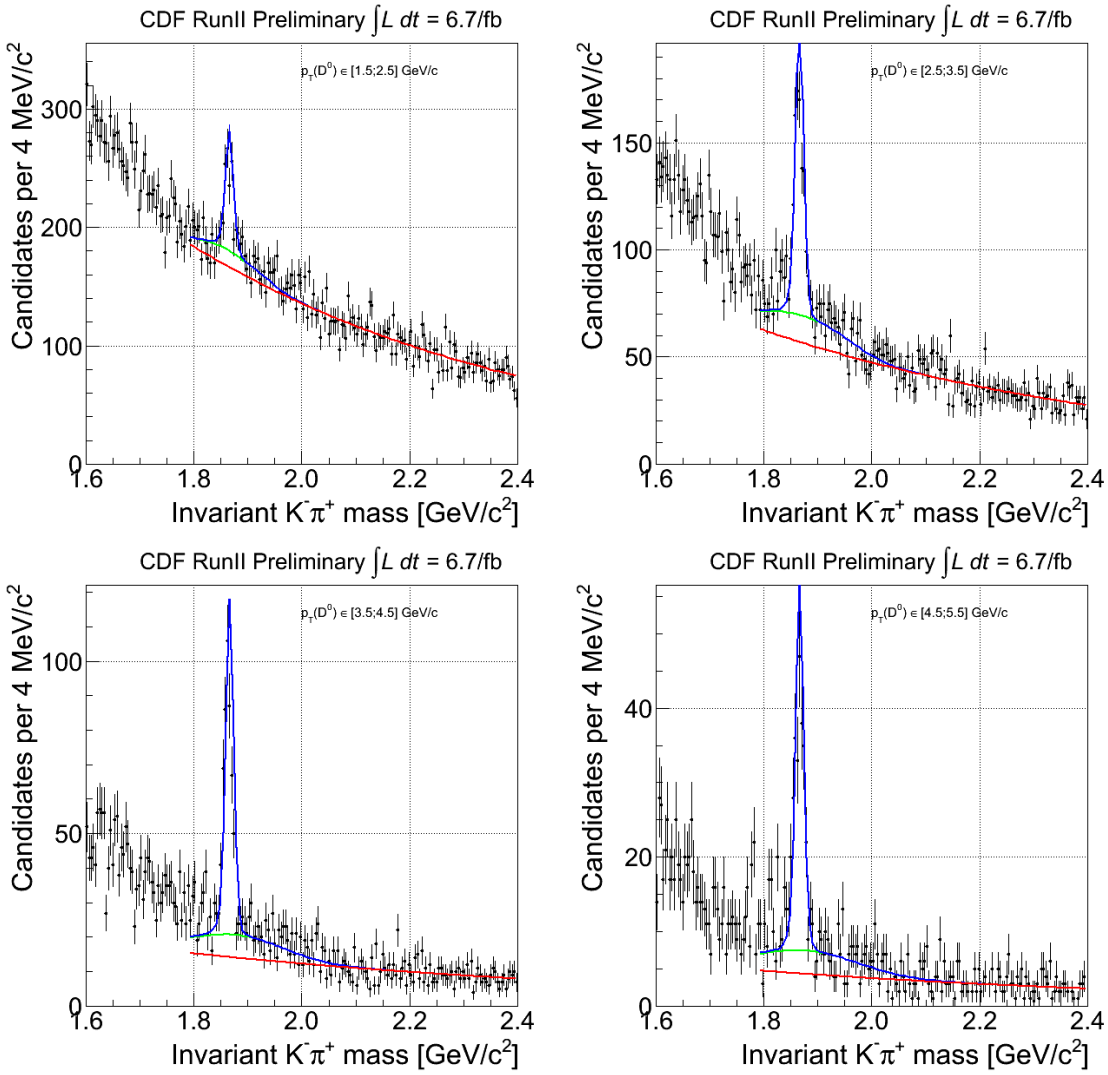

Figure 5.8: *Invariant $K^-\pi^+$ mass fit of data in 1 GeV/c intervals of $p_T(D^0)$.*

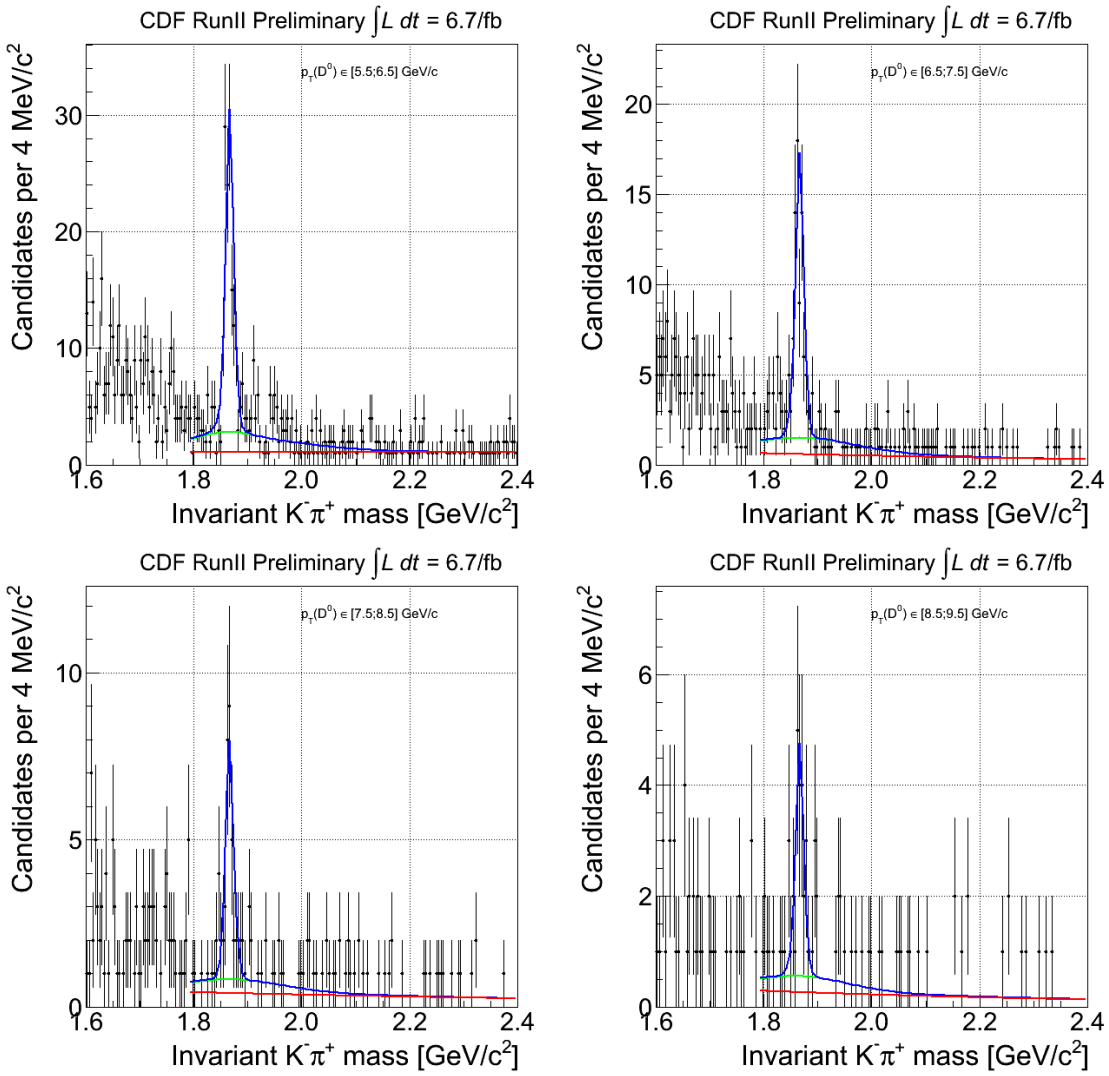

Figure 5.9: *Invariant $K^-\pi^+$ mass fit of data in 1 GeV/c intervals of $p_T(D^0)$.*

p_T [GeV/c]	$N_{D^0} + N_{\bar{D}^0}$
1.5 – 2.5	1042 ± 85
2.5 – 3.5	1511 ± 78
3.5 – 4.5	991 ± 57
4.5 – 5.5	522 ± 40
5.5 – 6.5	284 ± 22
6.5 – 7.5	164 ± 21
7.5 – 8.5	74 ± 14
8.5 – 9.5	51 ± 12

Table 5.2: *Invariant $K^-\pi^+$ mass fit results.*

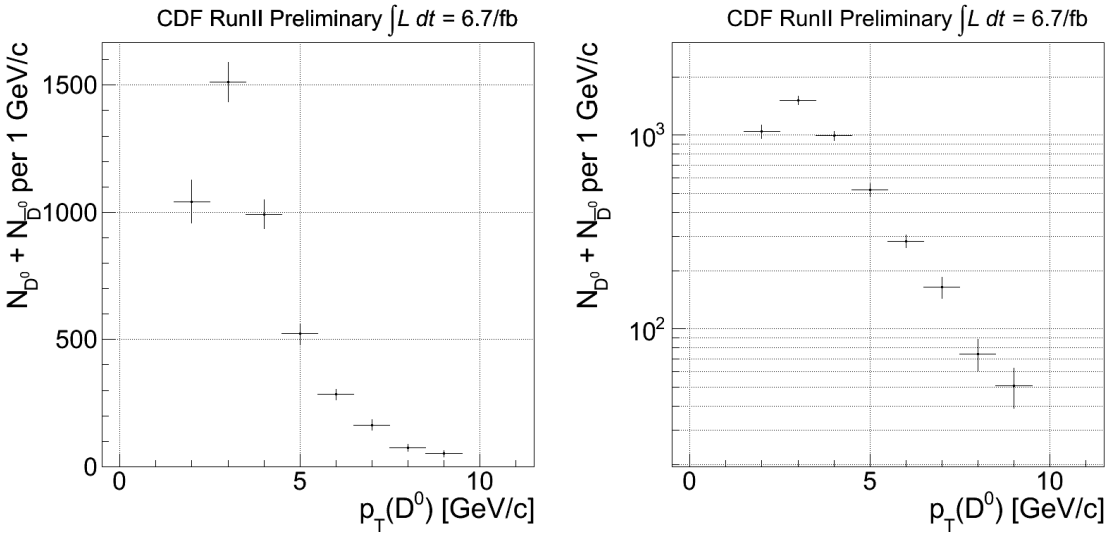

Figure 5.10: *Signals yields ($N_{D^0} + N_{\bar{D}^0}$) as a function of $p_T(D^0)$ from Table 5.2.*

Chapter 6

Efficiencies

The raw yields measured in Section 5.3 do not represent the real number of D^0 mesons produced by the Tevatron during the data taking time used for this work; inefficiencies and acceptances force us to see only a fraction of them. The following sections will describe the method we use to assess the fraction of mesons we loose through the steps of our analysis; we can then correct the yields measured and obtain the values to be used for the cross section calculation.

6.1 Trigger

This first section is devoted to the evaluation of the correction that takes into account any inefficiency due to the data taking process and the two triggers selection.

6.1.1 ZB

The ZB trigger does not need a signal from any CDF subdetector to be set because its accept status is synchronized with the Tevatron's bunch crossing frequency. The only possible source of inefficiency for this trigger is the dead time through the three-level trigger chain; because of the way the system is built, each trigger path's luminosity is automatically corrected by this non-operating time. This means that the value stored on the luminosity database do not need to be corrected and the value for the ZB trigger ε_{ZB} is 1.

6.1.2 MB

The MB trigger efficiency, instead, is highly dependent on crossing and event conditions: instantaneous luminosity (L_{inst}), number of charged particles in the event, maximum track p_T, overall E_T, pile-up, etc. Several studies to understand these

dependencies have been performed during Run II [31, 32, 33]. The quantities that play the most important role for this variable are the instantaneous luminosity, the number of tracks in the event and the number of reconstructed primary vertices. These dependencies are closely related: the higher the luminosity the larger the average number of interactions (and then reconstructed primary vertices) becomes. If the number of interactions grows, also the number of charged tracks increases; this is reflected in a rising efficiency as a function of these variables because the probability of a matching signal in both East and West CLC increases.
Because the ZB trigger path is 100 % efficient, we can use real data to evaluate the efficiency correction for the MB sample; in fact, each CDF event contains the trigger status for the whole active trigger table. This way it's easy to check if a particular ZB event was also triggered by the `MINBIAS` trigger path; the number of ZB events with the MB trigger fired (ZB_{CLC}) divided by the total number of ZB events (ZB) as a function of an arbitrary variable (X) represent the MB trigger efficiency as a function of that particular variable:

$$\varepsilon_{MB}(X) = \frac{ZB_{CLC}(X)}{ZB(X)} \tag{6.1}$$

Figure 6.1 shows ε_{MB} as a function of the three main variables related to the MB trigger efficiency: instantaneous luminosity, number of tracks in the event, number of reconstructed primary vertices.

The MB trigger efficiency correction can be handled in several ways; the most intuitive one is to reweight each event's contribution by a factor given by the efficiency trend w.r.t. a defined variable. Unfortunally a 1D correction (e.g. using the dependence on the number of reconstructed primary vertices) is not enough to take care of all the trigger's inefficiencies. A 2D approach using at the same time the number of tracks and vertices in the event seems to be a better option for our case. The effect of this correction on MB data in the invariant $K^-\pi^+$ mass plot has a negligible dependence on the invariant mass and on the candidates transverse momentum fluctuating around a +1 % correction; because the MB subsample is about the 40 % of the total sample, the global effect is at the 4 per mille level which is negligible w.r.t. the statistical uncertainties we expect on the yields measurement (~ 10 %). This confirms that the two subsamples can be safely added and we decided to handle this small correction as a systematic error. As a cross check, Figure 6.2 shows ε_{MB} as a function of the three main variables discussed above after the 2D event re-weighting.

6.2 Reconstruction

To evaluate the reconstruction efficiency as a function of $p_T(D^0)$ we used the Pythia QCD samples discussed in Section 4.2.1. This is simply done counting the number

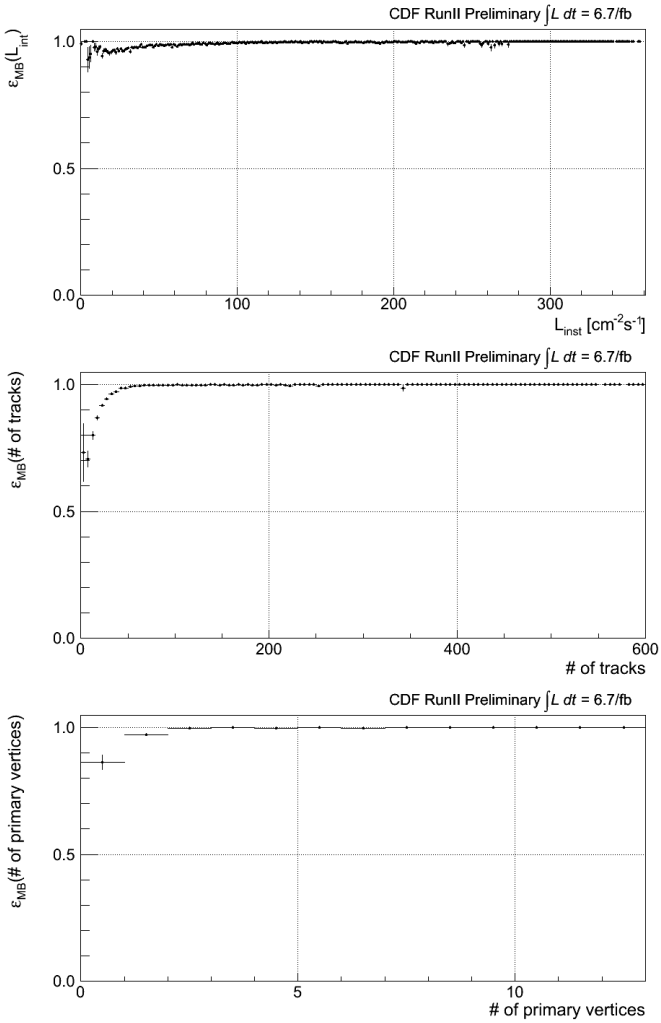

Figure 6.1: ε_{MB} *as a function of (from top): instantaneous luminosity, number of tracks in the event, number of reconstructed primary vertices.*

of D^0 and $\bar{D}^0$ generated in $|y| \leq 1$ from the MC and compare it to the number of candidates found after the selection. The ratio of the latter over the former gives the correction we are looking for:

$$\varepsilon_{rec}(p_T) = \left. \frac{N_{candidates}(p_T)}{N_{generated}(p_T)} \right|_{|y|\leq 1} \tag{6.2}$$

Table 6.1 summarizes this ratio in our range of interest and Figure 6.3 visually shows the global trend. This definition of ε_{rec} represents a global reconstruction efficiency for our candidates; it takes into account several corrections introduced by the detector response, the reconstruction process and our selection:

- detector geometrical acceptance and response to the passage of particles;

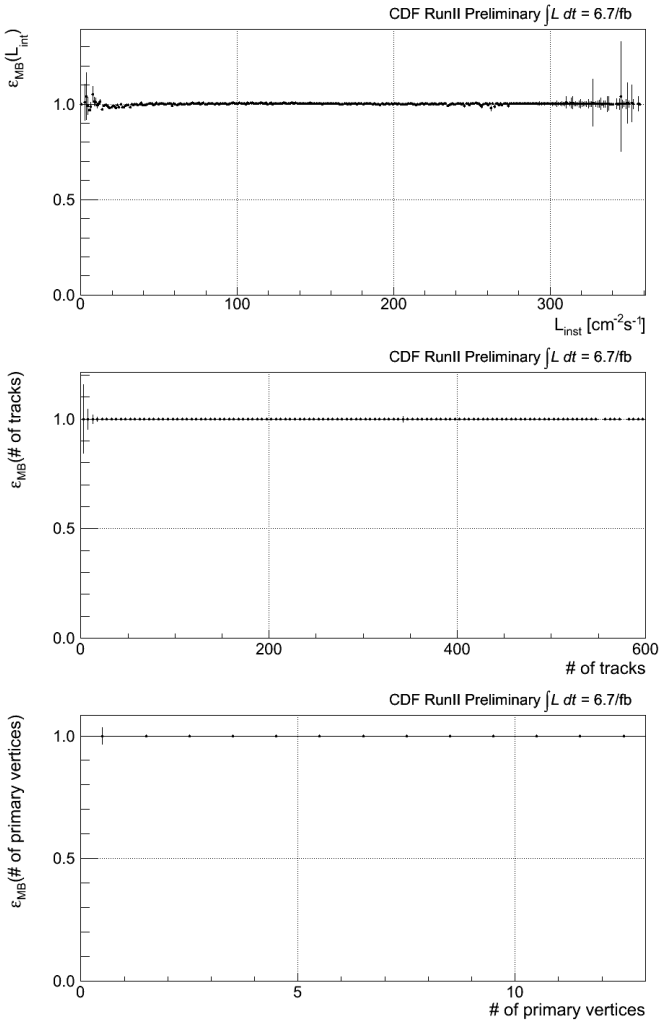

Figure 6.2: *ε_{MB} as a function of (from top): instantaneous luminosity, number of tracks in the event, number of reconstructed primary vertices after the re-weighting.*

- tracking efficiency in finding the charged particles passage;
- different algorithms involved in the tracking reconstruction with different efficiencies and acceptances;
- efficiency and acceptance corrections introduced by our selection of the candidates.

Figures 6.4 shows a comparison between real data and the MC simulation of some variables used to select our candidates; in thess plots, only candidates with a mass within 2σ from the expected D^0 mass are used and the background has been Side Band subtracted. MC seems to reproduce the features of the channel we are studing with a satisfactory accuracy.

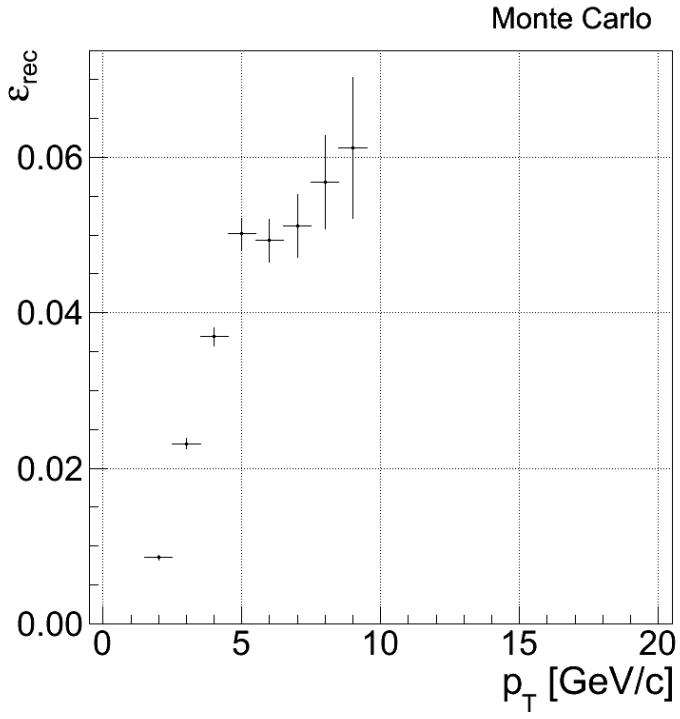

Figure 6.3: *Reconstruction efficiency as a function of* $p_T(D^0)$.

p_T [GeV/c]	ε_{rec} [%]
1.5 – 2.5	0.86 ± 0.03
2.5 – 3.5	2.32 ± 0.07
3.5 – 4.5	3.7 ± 0.1
4.5 – 5.5	5.0 ± 0.2
5.5 – 6.5	4.9 ± 0.3
6.5 – 7.5	5.1 ± 0.4
7.5 – 8.5	5.7 ± 0.6
8.5 – 9.5	6.1 ± 0.9

Table 6.1: *Reconstruction efficiency as a function of* $p_T(D^0)$.

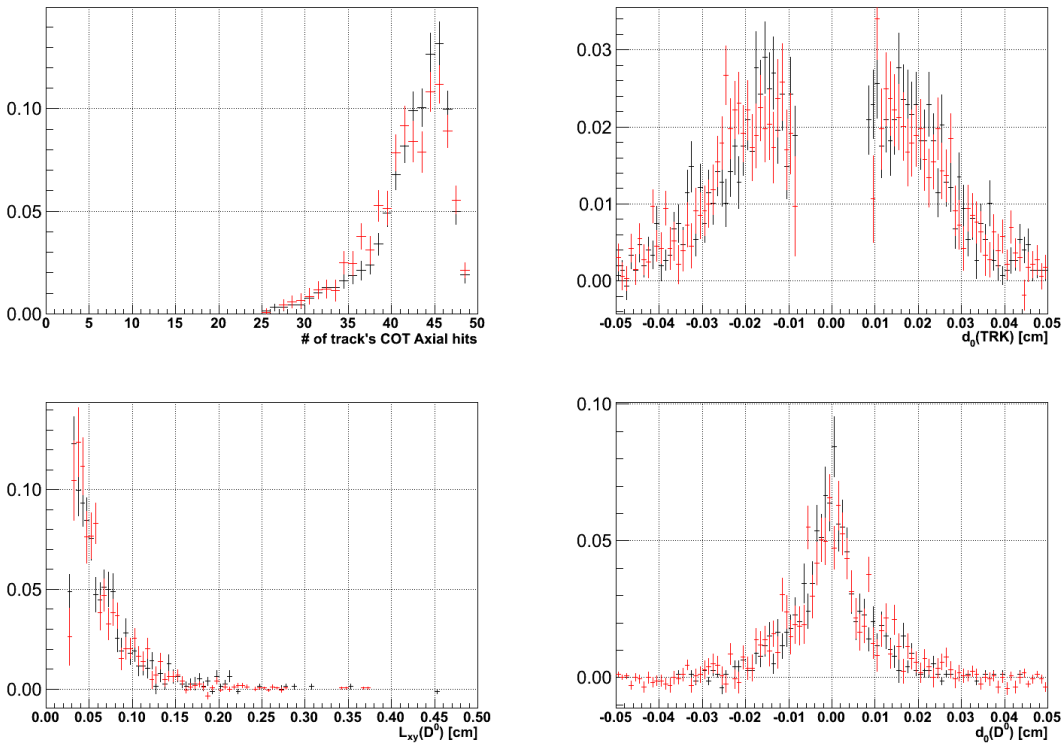

Figure 6.4: *Comparison of some relevant quantities between data (red) and MC (black); distributions are Side Bands subtracted.*

Chapter 7

Systematic uncertainties

7.1 Luminosity

As described in Section 3.3.2, CDF II instantaneous luminosity measurement is derived from the rate of the inelastic $p\bar{p}$ events estimated with the luminosity monitor (CLC). The only measurement of σ_{in} at the Tevatron has been performed at a center of mass energy of 1.8 TeV; the current evaluation of the luminosity rely on its extrapolation at 1.96 TeV. The systematic uncertainty associated to the extrapolation is 5.8 %, as reported in Table 7.1.

	L	syst
ZB	5.72	0.33
MB	4.48	0.26
Tot	10.2	0.6

Table 7.1: *Systematic uncertainties related to the luminosities values.*

7.2 Signal

Two are the main assumptions that could be source of a systematic uncertainty on the yields fitting procedure. The first is the extraction of the shapes of RS and WS signals; to test this assumption we repeated the procedure of the shape extraction using the Pythia MC and we obtained a small variation (≤ 1 %) of the resulting D^0 signals numbers after the likelihood fit of the yields. The second (and main) source of uncertainty is the backgroud modeling; because of the reduced lever arm for the exponential shape used to describe the combinatorial component, small variations in the slope of the function may reflect in not negligible effects on the final result of the fit. We then repeated the fit of the yields fixing the slope of the exponential to

the value obtained (through a binned fit) from the Same Sign candidates discussed in Section 5.1.3. Table 7.2 summarizes the uncertainties obtained bin by bin.

p_T [GeV/c]	syst [%]
1.5 – 2.5	2.9
2.5 – 3.5	5.4
3.5 – 4.5	7.9
4.5 – 5.5	4.6
5.5 – 6.5	7.6
6.5 – 7.5	2.1
7.5 – 8.5	5.1
8.5 – 9.5	2.0

Table 7.2: *Systematic uncertainties related to the signals extraction.*

7.3 Trigger efficiency

As already discussed in Section 6.1, the only, negligible, deviation from a 100 % trigger efficiency is due to the MB subsample. While the ZB is totaly efficient in the events collection, the MB efficiency to inelastic $p\bar{p}$ collisions is a function of several event's features; this deviation has already been assessed in the dedicated section to have an impact in the invariant $K^-\pi^+$ mass plot at the 1 % level. The MB subsample represents the 37.6 % of the total; we then (over)estimate the systematic uncertainty of this correction to be the 0.4 %.

7.4 Reconstruction efficiency

Table 7.3 reports our evaluation of the systematic uncertainties related to the reconstruction efficiency correction. We obtained them by reweighting the transverse momentum of the generated D^0:

- we've extracted the distribution that the MC uses to generate the D^0 mesons;
- for each 1 GeV/c bin, we've fit it with a straight line obtaining the slope within the bin;
- we've varied the fitted shapes to obtain three new distributions changing the slopes by the 20 %, the 50 % and the 100 % (flat p_T within the bin) as shown in Figure 7.1;

- we've repeated the procedure to estimate the reconstruction efficiency as described in Section 6.2.

We've then set the reconstruction uncertainties for each bin to the maximum variation obtained with the new distributions.

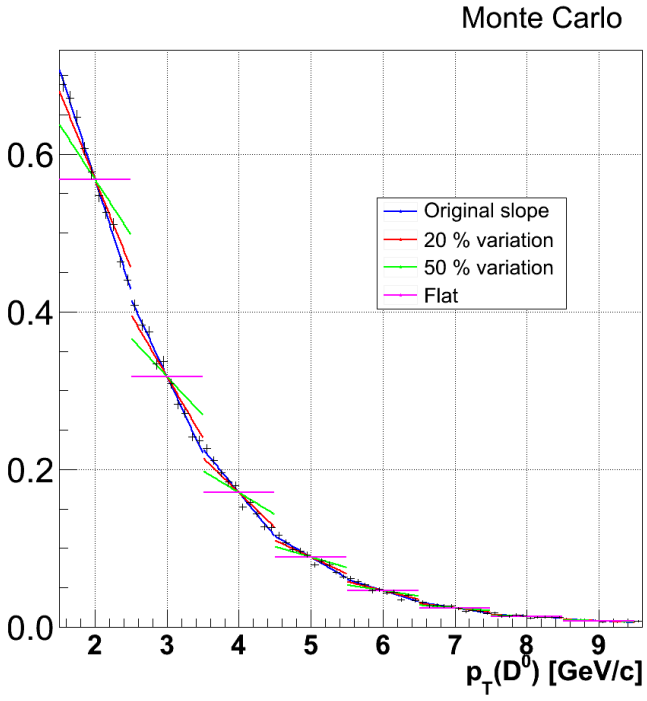

Figure 7.1: *Renormalization of the MC* $p_T(D^0)$.

p_T [GeV/c]	syst [%]
1.5 – 2.5	5.8
2.5 – 3.5	2.6
3.5 – 4.5	1.6
4.5 – 5.5	1.8
5.5 – 6.5	2.3
6.5 – 7.5	1.9
7.5 – 8.5	1.9
8.5 – 9.5	2.9

Table 7.3: *Systematic uncertainties related to the reconstruction process.*

Chapter 8

Cross section

Our measurement of the D^0 meson inclusive differential production cross section as a function of the transverse momentum (defined by Equation 8.1) is summarized in Table 8.1.

$$\frac{d\sigma_{D^0 \to K\pi}}{dp_T}(p_T; |y| \leq 1) = \left. \frac{\frac{N_{D^0}+N_{\bar{D}^0}}{2}(p_T)}{L \cdot \varepsilon_{trig} \cdot \varepsilon_{rec}(p_T) \cdot Br(D^0 \to K\pi)} \right|_{|y|\leq 1} \tag{8.1}$$

where:

- N_{D^0} and $N_{\bar{D}^0}$ are the yields of the D^0 and $\bar{D}^0$ signals in each bin of p_T. The factor of $1/2$ is included because we count both D^0 and $\bar{D}^0$ mesons while we report the cross section for D^0 mesons only and not for the sum of D^0 and $\bar{D}^0$; what is actually measured is the average cross section for D^0 and $\bar{D}^0$ mesons. This is correct under the assumption that the production process is charge invariant through strong interaction.
- L is the integrated luminosity of the data sample.
- ε_{trig} is the trigger efficiency.
- ε_{rec} is the global reconstruction efficiency of our candidates; it takes into account geometrical and kinematical acceptances and also the detector reconstruction efficiency of the signal.
- $Br(D^0 \to K\pi)$ is the decay branching ratio of the channel used in this analysis.

Our result is shown in Figure 8.1 and a comparison to the published CDF II measurement [12] is shown in Figure 8.2 and described in Appendix B.

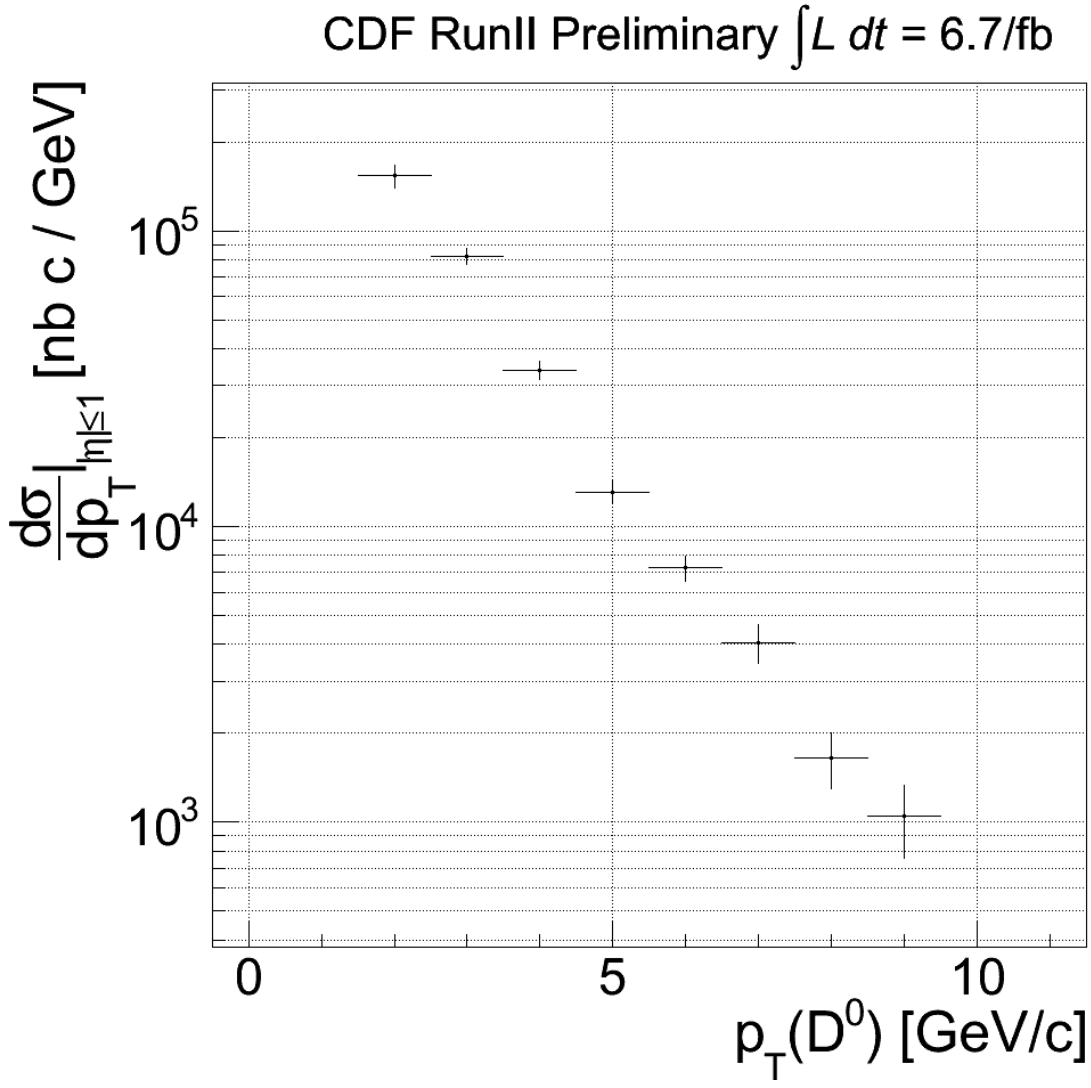

Figure 8.1: *D^0 meson inclusive differential production cross section as a function of the transverse momentum (only statistical uncertainties are shown).*

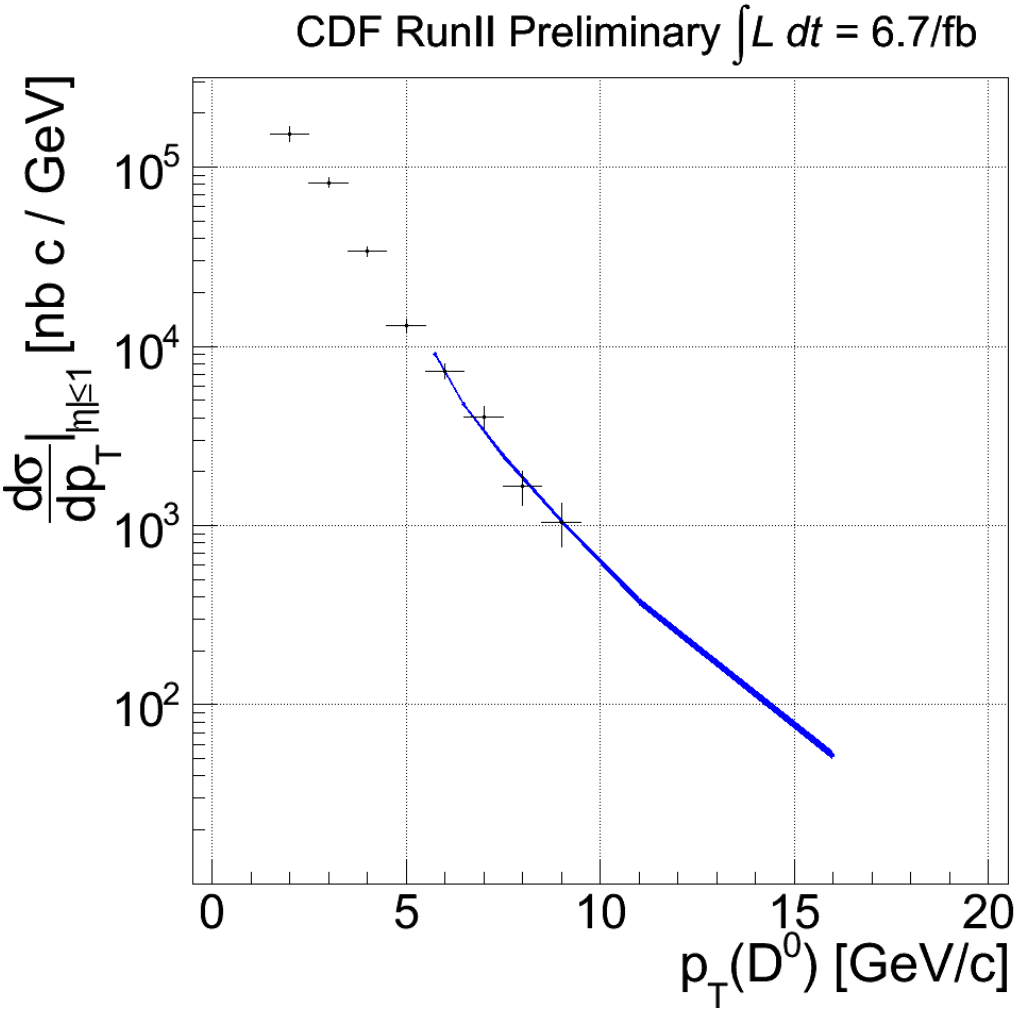

Figure 8.2: *Comparison of our result (black) and CDF published measurement [12] (blue).*

p_T [GeV/c]	[1.5; 2.5]	[2.5; 3.5]	[3.5; 4.5]	[4.5; 5.5]	[5.5; 6.5]	[6.5; 7.5]	[7.5; 8.5]	[8.5; 9.5]
$N_{D^0} + N_{\bar{D}^0}$	1,042	1,511	991	522	284	164	74	51
stat [%]	8.1	5.1	5.7	7.7	7.7	12.6	18.6	23.5
syst [%]	2.9	5.4	7.9	4.6	7.6	2.1	5.1	2.0
L $[(\text{nb})^{-1}]$	10.2	10.2	10.2	10.2	10.2	10.2	10.2	10.2
stat [%]	-	-	-	-	-	-	-	-
syst [%]	5.8	5.8	5.8	5.8	5.8	5.8	5.8	5.8
$\varepsilon_{\text{trig}}$	1	1	1	1	1	1	1	1
stat [%]	-	-	-	-	-	-	-	-
syst [%]	0.4	0.4	0.4	0.4	0.4	0.4	0.4	0.4
ε_{rec}	0.0086	0.023	0.037	0.050	0.049	0.051	0.057	0.06
stat [%]	3.6	3.0	3.3	3.9	5.6	7.8	10.6	14.8
syst [%]	5.8	2.6	1.6	1.8	2.3	1.9	1.9	2.9
$\text{Br}(D^0 \to K\pi)$	0.0389	0.0389	0.0389	0.0389	0.0389	0.0389	0.0389	0.0389
stat [%]	1.3	1.3	1.3	1.3	1.3	1.3	1.3	1.3
syst [%]	-	-	-	-	-	-	-	-
$\frac{d\sigma}{dp_T}\left[\frac{nb \cdot c}{GeV}\right]$	153,587	82,142	33,827	13,113	7,249	4,048	1,652	1,048
stat [%]	9.0	6.1	6.7	8.8	9.6	14.9	21.5	27.8
syst [%]	8.7	8.4	9.9	7.6	9.8	6.5	8.0	6.8

Table 8.1: *Differential cross section measurement result.*

Chapter 9

Conclusions

In this thesis we present a study of the D^0 meson (through one of its two-body decay channel, $D^0 \to K\pi$) collected by the CDF II experiment at the Tevatron $p\bar{p}$ collider at Fermilab. In particular we measured the differential production cross section as a function of the transverse momentum down to p_T = 1.5 GeV/c.

Since the non negligible mass of the c quark and the difficulty to apply perturbative expansion at scales below $\mu \sim \Lambda_{QCD}$, the production of charmed mesons at low p_T is a non pQCD process. This work represents the first measurement of the differential production cross section, of this charmed meson, extended to low p_T. The uniqueness of this measurement has to be highlighted because even if new-generation accelerators will be able to probe the same p_T range, their experimental conditions will not reproduce (at least for several decades from now) Tevatron ones both in terms of initial state ($p\bar{p}$) and center of mass energy ($\sqrt{s}$ = 1.96 TeV). Different energies means different conditions and processes active in this underlying soft region. A comprehension of the energy scale dependence in non-pQCD conditions plays a fundamental role in this picture too.

Our result is in perfect agreement with the published CDF II measurement [12] in the overlapping region ($5.5 \leq p_T \leq 9.5$ GeV/c)[1]. This gives the complete p_T spectum of the D^0 production from p_T = 1.5 GeV/c to p_T = 20 GeV/c. Some improvements of this measurement are still possible and planned (see Appendix A). The present result will be under internal CDF review for pubblication by the end of next summer.

[1]The comparison is discussed in Appendix B.

Appendices

Appendix A

Improvements

This appendix is devoted to the description of the improvements we can implement into the measurement discussed in this thesis.

A.1 Luminosity

Thanks to the stable CDF and Tevatron performances, more than 200/pb of data are currently collected each month; this means that by the next summer about 3 additional inverse fb of data will be available for our analysis. This will reflect in our measurement as a ~ 20 % reduction of the statistical uncertainties; in addition to that, new data could give us the opportunity to extend the measurement to an even lower minimum p_T: also the p_T bin covering the [0.5; 1.5] GeV/c range may show a signal peak with a significance over the background sufficiently big to ensure a statistical uncertainty smaller than the 20 %.

A.2 Efficiency

Thanks to SVT (see Section 2.2.6 for details), the CDF II performance in the B and D meson fields is even much better than the dedicated B-factories; the number of D mesons collected by the dedicated trigger paths is well beyond several hundreds on millions of candidates. Charged D may have an important role in analyses where the absolute charged tracks reconstruction efficiency is fundamental. They could be the key to evaluate this correction directly from data without relying to MC simulations; the $D^+ \to K^-\pi^+\pi^+$ channel, in particular, seems to have special features in this direction. While the invariant $K^-\pi^+$ mass shape of D^+ could be confused with the one obtained from a D^0 decaying into $K^-\pi^+\pi^0$, the invariant $\pi^+\pi^+$ mass has unique features: the only contribution with physical meaning to an invariant mass plot evaluated using Same Sign (SS) tracks comes from the $D^+ \to K^-\pi^+\pi^+$ channel. No other D meson decays may fall into this mass range; random pairs of

tracks are the only other possible contribution to the plot. A study of this property is on going; reproducing the expected shape of the D^+ candidates reconstructed in the invariant $\pi^+\pi^+$ plot it's possible to count the number of charmed mesons present in the sample. It's then possible to count again their number reconstructing the invariant mass adding the third track; the ratio of the latter over the former gives the absolute reconstruction efficiency of the third track. We are working to estimate it as a function of the third track's p_T; this dependence will give us a weight for each D^0 candidate entering the plot used to assess the signal yields discussed in Section 5.3.

A.3 Direct fraction

The cross section measured in this work takes into account the inclusive production of D^0 mesons at the Tevatron's energy; this means that all the contributes are integrated:

Prompt fraction : the prompt fraction of D^0 represents the mesons that are directly generated in the parton-parton interaction.

D^* **fraction** : because of their extremely small lifetime, $\Gamma = (96 \pm 22)$ keV, prompt D^0 and $\bar{D}^0$ that come from a D^* decay chain appear to have very similar kinematical and geometrical properties.

Secondary fraction : several B mesons have a D^0 as one of their decay products; unlike prompt D^0 (or D^0 produced by D^*), these secondary D^0 have an origin vertex displaced w.r.t. the primary $p\bar{p}$ interaction because of the relatively long lifetime of the B mesons.

In literature, the first two components are usually combined into the so-called *direct fraction*; they can only be separated tagging the D^0 from a $D^{*\pm}$ using the additional soft charged pion in the decay, but not if they come from a D^{*0} decay[1]. The situation is different if the D^0 comes from a B decay; the displaced origin vertex modifies the D^0 impact parameter distribution. The secondary fraction has a wider impact parameter distribution w.r.t. the direct one; a fit of this variable gives us the opportunity to assess the direct fraction of D^0 in our signal and compare it to the theoretical predictions for the prompt c quark production (that usually report the direct component behaviour).

[1] $D^{*\pm} \to D^0\pi^\pm$ while $D^{*0} \to D^0\pi^0$ and $D^{*0} \to D^0\gamma$ can't be tagged because coupled to a neutral particle.

Appendix B

Comparison cross check

Our inclusive measurement probes the transverse momentum range from 1.5 to 9.5 GeV/c while the published CDF result [12] covers the range from 5.5 to 20 GeV/c but only reports the differential cross section of the direct component. The published measurement (shown in Figure B.1) defined the differential cross section as follows:

$$\frac{d\sigma_{D^0\to K\pi}}{dp_T}(p_T;|y|\leq 1) = \left.\frac{\frac{N_{D^0}+N_{\bar{D}^0}}{2}(p_T)\cdot f_D}{L\cdot\varepsilon_{trig}\cdot\varepsilon_{rec}(p_T)\cdot Br(D^0\to K\pi)}\right|_{|y|\leq 1} \tag{B.1}$$

which differs from our definition (see Equation 1.14) only for the direct fraction cor-

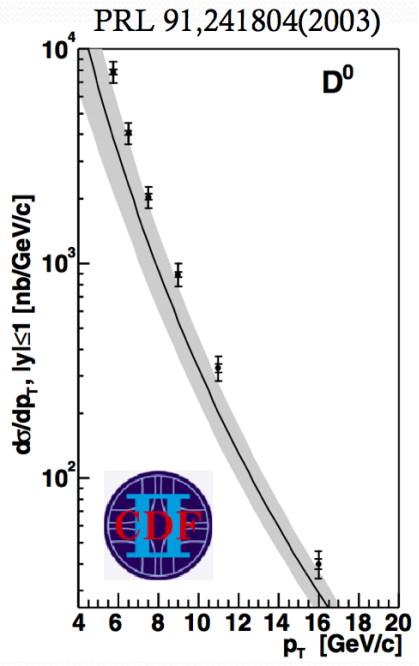

Figure B.1: *CDF published D^0 meson differential cross section.*

rection f_D. This means that we can compare them simply removing that correction. Table B.1 summarizes the old results and the direct fraction corrections applied to each bin. Figure 8.2 shows the comparison of the two results when the published one reports the inclusive cross section; they are in perfect agreement.

p_T [GeV/c]	[5.5; 6]	[6; 7]	[7; 8]	[8; 10]	[10; 12]	[12; 20]
$\frac{d\sigma}{dp_T}\left[\frac{nb \cdot c}{GeV}\right]$	7837	4056	2052	890	327	39.9
stat [%]	2.8	2.3	2.9	2.8	4.7	5.8
syst [%]	11.3	10.9	11.1	12.1	12.7	13.4
f_D [%]	88.4	87.9	85.8	86.7	89.0	78.3
stat [%]	1.0	0.9	1.2	1.1	1.7	2.4
syst [%]	4.1	4.1	4.1	4.1	4.1	4.1

Table B.1: *CDF published D^0 meson differential cross section.*

Bibliography

[1] M. Goldhaber, L. Grodzins and A. W. Sunyar, *Helicity Of Neutrinos*, Phys. Rev. **109** (1958) 1015.

[2] G. Arnison *et al.* [UA1 Collaboration], *Recent Results On Intermediate Vector Boson Properties At The Cern Super Proton Synchrotron Collider*, Phys. Lett. B **166** (1986) 484.

[3] R. Ansari *et al.* [UA2 Collaboration], *Measurement Of The Standard Model Parameters From A Study Of W And Z Bosons*, Phys. Lett. B **186** (1987) 440.

[4] P. W. Higgs, *Broken Symmetries, Massless Particles And Gauge Fields*, Phys. Lett. **12** (1964) 132.

[5] P. W. Higgs, *Broken Symmetries And The Masses Of Gauge Bosons*, Phys. Rev. Lett. **13** (1964) 508.

[6] K. Nakamura *et al.* [Particle Data Group], J. Phys. G **37**, 075021 (2010).

[7] A.V. Manohar and M. B. Wise, Camb. Monogr. Part. Phys. Nucl. Phys. Cosmol. **10**, 1 (2000).

[8] G. 't Hooft, Nucl. Phys. B **72**, 461 (1974).

[9] G. 't Hooft, Nucl. Phys. B **44**, 461 (1972).

[10] B. W. Lee, Phys. Rev. D **5**, 823 (1972).

[11] Ikaros I. Y. Bigi, *Charm physics - like Botticelli in the Sistine chapel*, hep-ph/0107102 (2001).

[12] D. Acosta *et al.* [CDF Collaboration], Phys. Rev. Lett. **91**, 241804 (2003).

[13] A. Adare *et al.* [PHENIX Collaboration], Phys. Rev. Lett. **97**, 252002 (2006).

[14] B. I. Abelev *et al.* [STAR Collaboration], Phys. Rev. Lett. **98**, 192301 (2007).

[15] J. Adams *et al.* [STAR Collaboration], Phys. Rev. Lett. **94**, 062301 (2005).

[16] B. A. Kniehl, G. Kramer, I. Schienbein and H. Spiesberger, AIP Conf. Proc. 792, 867 (2005).

[17] B. A. Kniehl, G. Kramer, I. Schienbein and H. Spiesberger, Phys. Rev. Lett. **96**, 012001 (2006).

[18] R. Blair *et al.* [CDF Collaboration], *The CDFII Detector: Technical Design Report*, FERMILAB-Pub-96/390-E (1996).

[19] Fermilab Beam Division, *Run II Handbook* and *Operations Rookie Books*.

[20] D. Acosta *et al.*, CDF note 6052, 2002.

[21] S. Klimenko, J. Konigsberg and T. Liss, CDF note 6314, 2003.

[22] K. Anikeev, P. Christoph and P. Murat, *Description of Bgenerato II*, CDF note 5092, 1999.

[23] R. Field and C. Group, CDF note 7822, 2005.

[24] R. Brun *et al.*, *GEANT: Simulation Program For Particle Physics Experiments. User Guide and Reference Manual*, 1978.

[25] P. A. Movilla Fernandez, *Performance of the CDF calorimeter simulation in Tevatron Run II*, AIP Conf. Proc., vol. 867, pp. 487-494, 2006.

[26] R. Veenhof, *Garfield, a drift chamber simulation program*, International Conference on Programming and Mathematical Methods for Solving Physical Problems, Dubna, Russia, 14-19 Jun 1993.

[27] R. Brun *et al.*, *ROOT object oriented data analysis framework.*, http://root.cern.ch.

[28] S. Jindariani *et al.*, CDF note 7446, 2005.

[29] S.Klimenko and J.Konigsberg, CDF note 6314, 2003.

[30] D. Acosta *et al.*, Phys. Rev. D **50**, 5518 (1994).

[31] D. Acosta *et al.*, CDF note 5861, 2002.

[32] D. Acosta *et al.*, CDF note 6054, 2002.

[33] N. Moggi and F. Rimondi, CDF note 8594, 2006.

Ringraziamenti

Poche righe per ringraziare tante persone che mi hanno permesso (sotto diversi punti di vista) di concludere questo lavoro di tesi.

Ovviamente il primo grazie DEVE andare ai miei genitori che hanno avuto un'enorme pazienza nell'accompagnarmi e sostenermi in questa strada, così lontana dai loro pensieri.

Un bacione a mia nonna che ce l'ha fatta a tenere a botta fino a questo giorno; l'ultima volta l'obiettivo era arrivare alla fine del dottorato ma ora lo spostiamo all'arrivo di un (bis)nipotino.

Passiamo ai colleghi: Prof. Franco Rimondi, Prof. Jeffrey A. Appel, Prof. Luciano Ristori, Dott. Michael J. Morello e Dott. Diego Tonelli ... cosa dire? Grazie mille per l'aiuto, le idee, le discussioni, i consigli, i rimproveri, la disponibilità, la gentilezza e l'esempio di cosa vuol dire essere un ricercatore nella Fisica delle alte energie. Senza il vostro aiuto non avrei mai potuto portare a termine questo lavoro.

È doveroso ringraziare il Prof. Cornia e la Prof. Santi; oltre ad essere tra i pochi insegnanti che non mi annoiavano al liceo, siete riusciti ad accendere in me la curiosità verso il mondo e la voglia di capirlo fino in fondo.

Infine il ringraziamento più sentito va alla mia dolce metà, Federica! Grazie per essere stata tanto paziente con me soprattutto negli ultimi mesi!

Un mega ringraziamento anche a tutti coloro che ho dimenticato o che ho omesso volutamente!

Alla prossima!

Bye...